Investigation of Intermolecular Interaction in organic thin films by means of NEXAFS Spectroscopy

vorgelegt von

Florian Holch

aus Ulm

Würzburg, 2009

Investigation of Intermolecular Interaction in Organic Thin Films by means of NEXAFS Spectroscopy

**Dissertation zur Erlangung des
naturwissenschaftlichen Doktorgrades
der Julius–Maximilians Universität Würzburg**

vorgelegt von
Florian Holch
aus Ulm

Würzburg 2009

Eingereicht am 20. Oktober 2009
bei der Fakultät für Physik und Astronomie

1. Gutachter: Prof. Dr. E. Umbach
2. Gutachter: Prof. Dr. J. Pflaum
der Dissertation.

1. Prüfer: Prof. Dr. E. Umbach
2. Prüfer: Prof. Dr. J. Pflaum
3. Prüfer: PD Dr. R.F. Fink
im Promotionskolloquium.

Tag des Promotionskolloquiums: 18.12.2009
Doktorurkunde ausgehändigt am: . . .

Wenn dir ein Fels vom Herzen fällt,
so fällt er auf den Fuß dir prompt!
So ist es nun mal auf der Welt:
ein Kummer geht, ein Kummer kommt...

Heinz Erhardt

Contents

Zusammenfassung

Die vorliegende Arbeit beschäftigt sich mit der Kopplung vibronischer und elektronischer Anregungen in großen organischen Molekülen. Insbesondere die Wechselwirkung zwischen diesen organischen Molekülen im Festkörper wird betrachtet. Für die Entwicklung von rein organischen oder hybriden elektronischen Bauteilen sind sowohl die elektronischen als auch die optischen Eigenschaften dieser Moleküle von entscheidender Wichtigkeit. Allerdings sind die Mechanismen des Ladungstransportes und damit auch die zu Grunde liegende Wechselwirkung der Moleküle im Festkörper immer noch Gegenstand aktueller Diskussionen [1–4]. Mit der Untersuchung der spektroskopischen Eigenschaften von einerseits freien, also gasförmigen Molekülen, andererseits von (stark) wechselwirkenden Molekülen im Festkörper soll mit der vorliegenden Arbeit ein Beitrag zum besseren Verständnis der intermolekularen Wechselwirkung geleistet werden.

Also Methode wurde die Röntgen–Nahkanten–Spektroskopie (NEXAFS) angewandt, die durch ihre chemische Selektivität lokale Informationen über die elektronische Struktur der Valenzzustände der untersuchten organischen Moleküle liefern kann [5]. Im experimentellen Teil wird eine Apparatur zur Untersuchung der organischen Moleküle in der Gasphase, die im Rahmen dieser Arbeit entwickelt wurde, vorgestellt. Das Hauptaugenmerk liegt dabei auf den Besonderheiten der Gasphasenmessungen sowie der Energiekalibrierung und anschließenden Datenauswertung.

Die qualitativ hochwertigen Spektren werden nach Gesichtspunkten der Energieposition, Form und Intensität der für die organischen Moleküle typischer Weise sehr scharfen π^* Resonanzen ausgewertet. Für Spektren mit gut aufgelöster Feinstruktur wurde die darunter liegende Schwingungsstruktur mit Hilfe einer Franck–Condon Auswertung untersucht, woraus sich weitere Informationen über die Einflüsse im Festkörper gewinnen ließen. Die dabei gesammelten Daten wurden zusammen mit den Ergebnissen früherer Untersuchungen der Schwingungsfeinstruktur organischer Moleküle herangezogen, um den Zusammenhang zwischen den Schwingungsenergien im elektronisch angeregten und im Grundzustand zu bestimmen. Dabei ergab sich eine gute Übereinstimmung mit empirischen Untersuchungen der Schwingungsstruktur kleiner Moleküle anhand von Photoelektronenspektroskopie (PES) [6].

Im Allgemeinen wird den hier untersuchten organischen Materialien eine sehr schwache Wechselwirkung mittels van–der–Waals Kräften zugeschrieben. Die vorliegenden Ergebnisse zeigen jedoch ausgeprägte Unterschiede in den Spektren der

verschiedenen Phasen, die sich nicht im Rahmen einer Wechselwirkung durch rein dispersive Kräfte erklären lassen.

Im Einzelnen traten zwischen den Gasphasen– und Festkörperspektren der C–K Kanten von 1,2,4,5–Benzoltetracarbonsäuredianhydrid BTCDA, 1,4,5,8–Naphthalintetracarbonsäuredianhydrid NTCDA und 3,4,9,10–Perylentetracarbonsäuredianhydrid PTCDA Rotverschiebungen von 0,1 bis 0,3 eV auf. Die entsprechenden elektronischen Übergänge sind jeweils dem aromatischen System zugeordnet und zeigen in der Reihe von BTCDA zu PTCDA eine zunehmende Verschiebung. Dies deutet auf eine verstärkte Wechselwirkung bei größeren Molekülen, beziehungsweise bei einer dichteren Packung hin. Übergänge die dem Anhydrid Kohlenstoff (C_1) zugeordnet sind, zeigen jedoch keinerlei Verschiebung. Die Spektren der O–K Kanten von BTCDA und NTCDA weisen lediglich eine leichte Veränderung der relativen Intensitäten auf. Im Falle von PTCDA wurde eine Blauverschiebung von bis zu 0,2 eV für den O_B 1s→LEMO+1 Übergang beobachtet.

In dieser Arbeit werden einige theoretische Modelle vorgeschlagen, die auf einer Änderung der Molekülgeometrie bzw. einer Wechselwirkung der Molekülorbitale sowohl im Grund– als auch im angeregten Zustand basieren. Betrachtet man lediglich eine einzelne Molekülsorte, so liefert z.B. eine Wechselwirkung der Orbitale benachbarter Moleküle eine zufriedenstellende Erklärung für die beobachteten Änderungen. Bei einer umfassenden Betrachtung aller Moleküle der Dianhydrid Gruppe scheitert dieses Modell jedoch. Erste quantenchemische Berechnungen der Wechselwirkung mittels einer exzitonischen Kopplung der NTCDA Moleküle mit ihren gewinkelten Nachbarn lieferten keine nennenswerten Verschiebungen der Resonanzenergien. Weiterführende Rechnungen dieser Art stehen jedoch für die gestapelten Nachbarn sowie für das größere PTCDA noch aus.

Bei dem Molekül Tris(8-chinolinol)aluminium Alq$_3$ lassen sich alle beobachteten Verschiebungen einem Orbital, dem LEMO+2 zuordnen. Obwohl die Verschiebungen für die verschiedenen Absorptionskanten unterschiedlich sind, lässt sich die Wechselwirkung des Moleküls somit diesem Orbital, das an der Phenolat Seite des Liganden lokalisiert ist, zuordnen.

Zusammenfassend lässt sich sagen, dass die Röntgen–Nahkanten Spektroskopie hochinteressante und sehr genaue Informationen über die Änderung der elektronischen Struktur organischer Moleküle beim Übergang in die kondensierte Phase liefern kann. Grundvoraussetzung dafür ist jedoch eine sehr sorgfältige Vorgehensweise sowohl beim Experiment als auch bei der Datenauswertung, vor allem bezüglich der Gasphasenresultate. Die Ergebnisse dieser Arbeit können als eine Referenz für zukünftige experimentelle und (dringend benötigte) theoretische Untersuchungen betrachtet werden. Für ein umfassendes Verständnis der komplexen Wechselwirkung zwischen organischen Molekülen sind diese weiteren Untersuchungen unabdingbar.

Summary

The present work reports on the electron–vibron coupling in large organic molecules and particularly on the intermolecular interaction in molecular condensates. The optical and electrical properties of these organic systems are in the focus of attention due to their crucial importance for the development of (hybrid) organic electronic devices. In particular, the charge transport mechanism and hence the interaction between condensed molecules is a matter of debate [1–4]. In order to shed light on this interaction, the spectroscopic signatures of isolated molecules in the gas phase and their condensed counterparts have been studied.

The applied technique, near–edge x–ray absorption fine structure (NEXAFS) spectroscopy, is a local probe with high chemical selectivity, well suited for the investigation of the electronic structure of molecular valence levels [5]. In the experimental part, the experimental set–up developed in this work is described with special attention to the characteristic issues of gas phase measurements, energy calibration and the subsequent data evaluation.

The high quality gas phase and solid state NEXAFS spectra are analysed with respect to energy positions, shape and intensity of the sharp π^*–resonances characteristic for these aromatic molecules. Where applicable, a detailed Franck–Condon (FC) analysis of the vibronic fine structure has been performed, yielding additional information on the changes that occur upon solid state formation. Together with former results on vibrational features in large organic molecules, this information has been used to investigate the correlation of vibrational energies in the ground and electronically excited state. We find a relatively good agreement with other empirical studies on vibronic structures in photoelectron spectroscopy (PES) spectra of small molecules [6].

The molecular compounds investigated are in general believed to interact via weak van–der–Waals forces only. The present results however reveal distinct differences between the spectra of the gas and solid phase that can not be explained within the context of a mere interaction by dispersive forces.

In detail, differential red–shifts of 0.1 to 0.3 eV of transitions assigned to the aromatic system have been observed in the C–K spectra of benzene–tetracarboxylic acid dianhydride (BTCDA), 1,4,5,8–naphthalene–tetracarboxylic acid dianhydride (NTCDA), and 3,4,9,10–perylene–tetracarboxylic acid dianhydride (PTCDA) upon solid state formation. From BTCDA to PTCDA the shift increases, indicating an improving intermolecular interaction with molecular size or a closer molecular

packing. In contrast, all transitions assigned to the anhydride carbon atom (C_1) do not show any shift. For the O–K spectra, small changes in relative intensity have been observed for BTCDA and NTCDA. In case of PTCDA, a blue–shift of up to $0.2\,\mathrm{eV}$ is evident for the O_B 1s→LEMO+1 transition.

Theoretical models for the intermolecular interaction have been proposed in this work, based on a change of molecular geometry and interaction of adjacent molecules in the ground and excited state, respectively. While an interaction of adjacent molecular orbitals may explain the experimental findings for one particular molecule, this model falls short for a comprehensive explanation of all three dianhydrides. For an interaction in the excited state, the excitonic coupling with the neighbours attached at an angle, quantum chemical calculations yield no significant change in peak positions for NTCDA. Unfortunately, results for the stacked neighbours as well as the larger compound PTCDA are still lacking.

For tris (8–quinolinol) aluminum (Alq$_3$), the observed peak–shifts are restricted to just one unoccupied orbital, the LEMO+2, which is mainly localised at the phenoxide side of the quinolinol ligands. Although the shifts differ for the individual edges, the main interaction can therefore be assigned to this orbital.

In summary, NEXAFS spectroscopy, if performed with great care in terms of experimental details and data analysis especially for the gas phase data, provides very detailed and highly interesting data on the changes of the electronic structure of organic molecules upon condensation. The present data can be applied as a reference for further experimental and (highly desired) theoretical investigations, which are needed for a comprehensive understanding of the complex interaction mechanisms between organic molecules.

Introduction

1

Within the past few years, organic semiconductors found their way into our daily life in form of organic electronics, in particular in displays for electronic devices such as MP3 players and digital cameras [7]. The excellent optical properties of these organic compounds let organic light emitting diodes (OLEDs) already compete well with their silicon based counterparts. Possibly, organic photovoltaic devices (OPVDs) will soon tread in their footsteps. The crux of the organic and polymeric semiconductors still are their relatively poor transport properties. Especially for future 'all–organic–devices' using also organic transistors, this issue has to be tackled.

While a comprehensive model for transport in organic thin films is discussed controversially [1–4], the main reason for low charge carrier mobilities is attributed to the weak intermolecular interaction in these organic materials. In contrast to this general belief, hard evidence of very efficient intermolecular interaction has been found.

Electronic polarisation relaxation, also referred to as intermolecular screening for example has been found to be very efficient: Surface core–level shifts, stating different electronic surrounding for the surface compared to bulk, could not be detected for several organic compounds [8]. Apart from a very efficient polarisation of the neighbouring molecules this behaviour may be explained by a very fast and effective charge transfer to, or from the excited molecule. However, this does not fit into the model of weakly interacting molecules. In addition, a dispersion of about 200 meV and more has been found for the HOMO levels of typical organic compounds, even at room temperature [9, 10]. This finding is also contradictory to the often applied model of an 'ordered molecular gas', since one prerequisite of dispersion, apart from structural order, is a significant interaction of the respective orbitals. To overcome these discrepancies, a better understanding of the intermolecular interaction and its effect on the occupied and unoccupied molecular levels is needed.

In this work, the intermolecular interaction between organic molecules has been investigated by means of near–edge x–ray absorption fine structure (NEXAFS) spectroscopy. NEXAFS is a local probe with high chemical selectivity, well suited for the investigation of the electronic structure of molecular valence levels [5]. Moreover, due to the involved core excitation, contributions from one atomic species in symmetrically non–equivalent positions within the molecule can be distinguished.

This allows mapping the unoccupied molecular orbital distribution over the molecule and thus provides *local* information. This latter fact distinguishes NEXAFS from optical spectroscopies, which have shown high sensitivity to intermolecular interactions arising from the molecular environment in the solid [11, 12] and liquid phase [13], respectively.

The straightforward approach to better understand the intermolecular interactions in organic compounds is to compare the spectroscopic signatures of isolated molecules in the gas phase with their condensed counterparts [14]. Changes in valence states and transport levels can give information about the transport mechanism in the organic crystal.

For a detailed comparison, however, the gas phase data must not lag behind the solid state data concerning resolution and signal to noise ratio. Only with data sets of comparably high quality, the small spectral differences between the two phases become evident and may be interpreted reliably.

To meet these requirements, a new experimental set up was built, taking advantage of a contained volume, in contrast to other existing gas phase beam lines for organic compounds [15]. The basic functional efficiency has already been shown for some molecules [16]. Within the present work not only the functionality has been optimised for larger molecules, but also the subsequent data evaluation has been improved.

With the claim for high quality gas phase data satisfied, the same detailed analysis is possible as for the solid state. This includes the common peak fit deconvolution that yields a deep understanding of the spectral composition as well as the Franck–Condon fitting routines that allow a modelling of the observed vibronic coupling.

For the interpretation of the data, several basic models for the intermolecular interaction will be proposed, partly supported by quantum chemical calculations.

Theoretical Basis

<div style="text-align: right; font-size: 3em;">2</div>

2.1 Basics on Organic Molecular Crystals

Organic molecular crystals (OMC) are in general characterised by their low mechanical strength, low melting and sublimation temperature as well as low charge carrier mobility. These *macroscopic* properties of the crystal are determined on the one hand by the *microscopic* properties of the molecules and on the other hand by the mutual interaction of the subunits.

The mechanical properties can be explained readily by the binding mechanism in OMC which is in general referred to as 'van–der–Waals like'. In fact, dispersive forces cause the nonvalent interaction of the electronically neutral compounds. For nonpolar molecules, fluctuating multipole moments, primarily caused by weakly bound σ and π electrons, are the source of attraction. Pure static approaches in contrast do not yield any attractive interaction [17]. The resulting *inter*molecular binding energies are two to three orders of magnitude smaller than the covalent *intra*molecular ones.

The cause of the *electrical* properties of the crystal, however, is more complicated. The microscopic electronic properties of these molecules are in general highly anisotropic, simply due to their non spherical geometry and extended π–systems. Therefore, the transport in OMC depends not only on the mutual alignment of the molecules, but also on the morphology of the organic crystal or thin film. In addition, domain–sizes and boundaries play an important role for charge localisation and trapping. Therefore, a large spectrum of charge carrier mobilities is reported in literature, not only for different compounds, but also for different morphologies or preparation conditions of the investigated thin films [18]. While organic n–type semiconductors still lag behind their inorganic counterparts, charge carrier mobilities comparable with amorphous silicon (α–Si) have been reported for organic p–type semiconductors.

The model of mere van–der–Waals type of interaction surely does not treat these complex properties adequately. Results of investigations by means of optical– and photoelectron spectroscopy also cast doubt on this simple model, as will be outlined in the following.

2.1.1 Optical Spectroscopies

Many spectroscopic techniques have been applied for investigations of the electronic structure of OMCs, amongst others optical absorption–, photo luminescence–, and Raman spectroscopy. Using the example of 3,4,9,10–perylene–tetracarboxylic acid dianhydride (PTCDA), some results from optical spectroscopies on OMCs will be outlined in the following.

Solute PTCDA, as well as ultrathin layers at low temperature can be considered as non–interacting monomers, and show a nicely resolved vibronic progression in optical absorption spectra [19, 20]. With increasing film thickness a continuous red–shift up to $0.12\,\text{eV}$ and a broadening of line width is observed. For PTCDA molecules isolated in a SiO_2 matrix, the line width is increased significantly due to inhomogeneous solvent interaction. In contrast, the basic structure and the transition energy are preserved [21].

For the amorphous thin film spectra this is not the case. The lowest transition is red shifted by about $0.15\,\text{eV}$ compared to the monomer spectrum, and the basic structure as well as the feature width is changed completely [21].

These examples show that optical absorption spectroscopy is quite sensitive to the surrounding of the molecule, i.e. the intermolecular interaction. Also Raman– and photo luminescense (PL) spectroscopy yield complementary results [21–24] and therefore corroborate this interpretation.

Since the lifetime of the optically excited state ($\approx 10^{-10}$s [20]) is larger than the relaxation time of the molecular frame, Raman– and PL spectroscopy probe the molecule in its equilibrium geometry of the excited state. Thus, different molecular surroundings, which may affect the molecular relaxation process can also influence the Raman– and PL spectrum additionally.

All these optical spectroscopies yield information averaged over the whole molecule, since the participating molecular valence orbitals (primarily HOMO and LUMO) are in general widely spread over the molecule. Intermolecular interactions with a very local character are therefore hard to distinguish.

For more local information, NEXAFS spectroscopy is very promising, since the chemical selectively allows a more pointed investigation of the unoccupied orbitals. In addition, NEXAFS spectroscopy essentially probes the molecule in its ground state geometry since the core hole life time ($\approx 10^{-15}$s [5]) is shorter than the vibrational relaxation ($\approx 10^{-13}$s) [25].

2.1.2 PES

For the numerous techniques of photoelectron spectroscopy (PES), gas phase, or other monomer spectra of large organic molecules are rarely found [26]. The reason for this probably lies in the intrinsic incompatibility of the required conditions for

electron energy analysis and organic compounds in gas phase. Therefore, we need to revert to samples already gaseous at room temperature.

For the ionised states in ultraviolett photoelectron spectroscopy (UPS) or x–ray photoelectron spectroscopy (XPS), the screening of the remaining (core)hole is a very important process. Depending on the investigated system, shifts in the range of some eV may occur. For very reactive systems such as $O_2/Pt(111)$ for example, shifts of about 5 eV are observed in XPS spectra of the physisorbed compared to weakly chemisorbed species [27, 28]. In the respective NEXAFS spectra in contrast, the shift is only about 0.5 eV even for this interacting system. This shows that NEXAFS is not very sensitive to polarisation or screening effects due to its neutral final state. This also holds for large organic molecules, as shown by the UPS investigation on PTCDA in the gas and solid state [29], described in chapter 5.4.4.

Existing investigations by means of NEXAFS spectroscopy on large organic molecules in the gas phase [14, 30–32] yielded small and not very detailed differences compared to the solid state spectra. This is mainly due to the poor resolving power of the former beamlines as well as to a poor energy calibration.

Other well known effects of inorganic solid state physics, as the splitting of degenerate levels described as Bethe splitting [33, 34], are just too small to be resolved in PES. Distortions of the molecule in the molecular crystal and the resulting splitting due to the decrease in symmetry, referred to as Jahn–Teller effect [35], may in fact cause differential energy shifts, the size of the shift however is in the range of tenths of meV and therefore also too small to be resolved.

2.2 NEXAFS Spectroscopy

Using near–edge x–ray absorption fine structure (NEXAFS) spectroscopy, not only information on the electronic structure of the unoccupied– and core levels can be gained, but also on geometric conditions especially of surface adsorbates. NEXAFS has been used on a wide range of different materials in different phases [5, 36] which we want to extend with the present work to large organic molecules in the gas phase. In the following chapter, the most important aspects of NEXAFS theory will be outlined, more detailed information can be found in reference [5].

In figure 2.1 the NEXAFS process for a diatomic molecules is depicted. When the incident monochromatic X–ray beam is stepped in energy over the absorption edge of a specific element, an absorption spectrum similar to the one on the left hand side will be detected. Right before the ionisation energy of the respective atomic K–, L–, etc. shell is reached, i.e. $h\nu \lesssim E_{vac} - E_B$, very sharp absorption features are observed, provided a sufficient resolving power. These peaks occur at photon energies that fit the energy difference between the core level of the respective element and unoccupied orbitals. The peak intensity therefore is a measure for
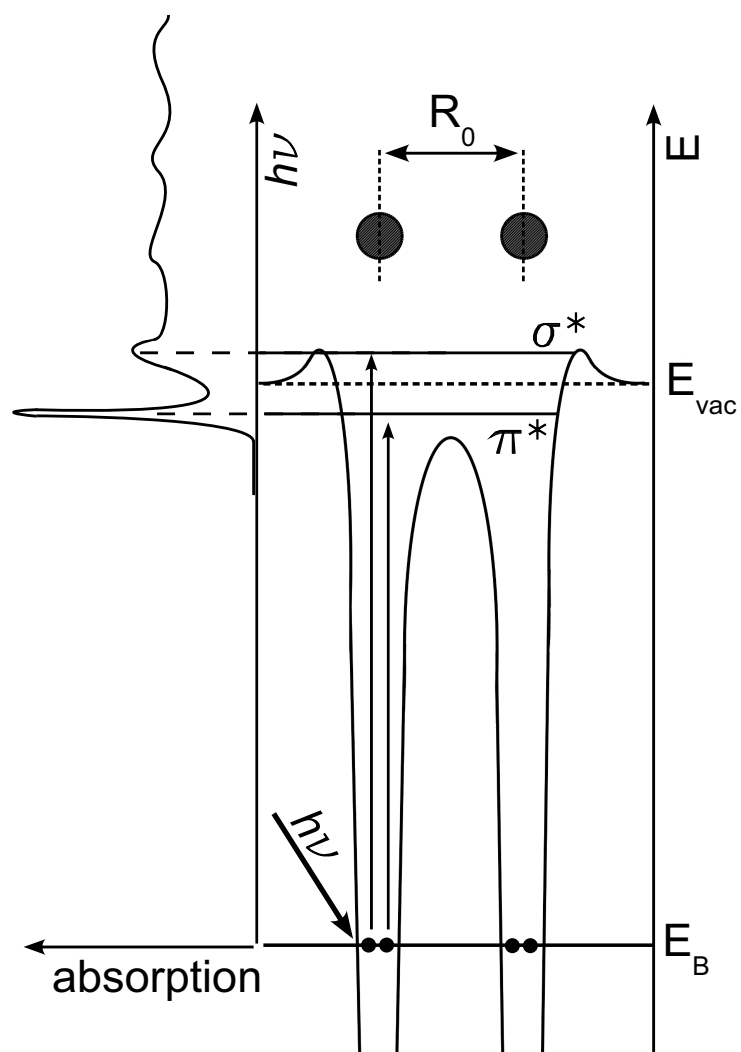
Figure 2.1: Schematic view of the NEXAFS process for a diatomic molecule. At the left hand side the resulting NEXAFS spectrum with characteristic π^* and σ^* resonances is plotted.

the overlap of the very localised core state with the in general more delocalised unoccupied orbitals.

The presence of the core hole significantly changes the unoccupied molecular orbitals, depending on the specific atomic site where the excitation is performed. Consequently and to avoid confusion, the lowest orbital into which the core electron is excited will be referred to as Lowest **E**xcited Molecular Orbitals (L**E**MO) rather than Lowest **U**noccupied Molecular Orbitals (L**U**MO).

As shown in figure 2.1, orbitals with π and σ symmetry are observed. In the present work, we will focus on the π^* resonances, which show sharper features that can better be assigned to specific transitions. In addition, for many large organic molecules, well resolved vibronic fine structure can be observed in these resonances.

To describe the NEXAFS process from a theoretical view point, we can start with Fermi's golden rule that gives the probability P_{if} per unit time for a transition from the initial state $|i\rangle$ to the final state $|f\rangle$ [5]:

$$P_{if} \sim \left| \left\langle f \left| \hat{H}' \right| i \right\rangle \right|^2 \delta \left(\hbar\omega - E_{if} \right) = \left| M'_{if} \right| \delta \left(\hbar\omega - E_{if} \right) \qquad (2.1)$$

The conservation of energy is accounted for by the delta function, assuring the photon energy to be equal to the energy difference E_{if} of final and initial state. $\left| M'_{if} \right|$ is the so called transition matrix element and contains the perturbation operator $\hat{H}'$. In this case $\hat{H}'$ can be written as

$$\hat{H}' = -\frac{e}{2mc} \left(\hat{p}\hat{A} + \hat{A}\hat{p} \right) \qquad (2.2)$$
$$\text{with} \quad \hat{p} = -i\hbar\vec{\nabla}$$
$$\text{and} \quad \hat{A} = \vec{e}\,A_0\,e^{i\left(\vec{k}\vec{r} - \omega t\right)}$$

where $\hat{p}$ is the momentum operator, $\vec{e}$ the polarisation direction of the incident light, and $\hat{A}$ the vector potential depending on wave vector $\vec{k}$ and position vector $\vec{r}$. Applying the Coulomb gauge $\vec{\nabla} \cdot \hat{A} = 0$ (see also chapter D.1), (2.2) is simplified since $\hat{A}$ and $\hat{p}$ then commute.

If the wave length of the incident light is large compared to the orbital size investigated, i.e. $\vec{k}\vec{r} \ll 1$, the dipole–approximation can be used, leaving only the first term of the Taylor expansion of the exponential function:

$$e^{i\left(\vec{k}\vec{r} - \omega t\right)} = 1 + i \left(\vec{k}\vec{r} - \omega t \right) - \tfrac{1}{2} \left(\vec{k}\vec{r} - \omega t \right)^2 \dots$$

Admittedly, the dipole approximation is at the borderline for the O–K edge (ca. $530\,\text{eV}$) with wave lengths smaller than 4Å. Thus, additional multipole terms may contribute to the spectrum in this case, but the main intensity will still be of dipole nature.

Finally, (2.1) is simplified to

$$P_{if} \sim |\langle f\,|\,\vec{e}\,\hat{p}\,|\,i\rangle|^2\,\delta\left(\hbar\omega - E_{if}\right) \tag{2.3}$$

where $|\langle f\,|\,\vec{e}\,\hat{p}\,|\,i\rangle| = |M_{if}|$ is in general denoted as the *dipole* matrix element.

The initial and final state wave functions still contain the complete information on all electrons in the system. This can be further simplified, if the excitation process is fast enough that just the 'active' electron has to be considered. In the *sudden approximation* the wave function of the active electron, ϕ_1, is separated from the, as implied, constant wave function $\Psi(N-1)$ of the remaining electrons. Therefore, the momentum operator $\hat{p}$ is expanded in the sum of individual momentum operators $\hat{p}_k$ of the individual electrons:

$$\begin{aligned}
\langle f\,|\,\vec{e}\,\hat{p}\,|\,i\rangle &= \left\langle \Psi^f(N)\,\middle|\,\vec{e}\sum_{k=1}^{N}\hat{p}_k\,\middle|\,\Psi^i(N)\right\rangle \\
&= \left\langle \phi_1^f\,\middle|\,\vec{e}\,\hat{p}_1\,\middle|\,\phi_1^i\right\rangle \left\langle \Psi^f(N-1)\,\middle|\,\Psi^i(N-1)\right\rangle + \\
&\quad + \underbrace{\left\langle \phi_2^f\,\middle|\,\vec{e}\,\hat{p}_2\,\middle|\,\phi_2^i\right\rangle}_{\approx 0}\underbrace{\left\langle \Psi^f(N-1)\,\middle|\,\Psi^i(N-1)\right\rangle}_{\lesssim 1} + \ldots \\
\Rightarrow |M_{if}|_{SA} &= \left|\left\langle \phi_1^f\,\middle|\,\vec{e}\,\hat{p}_1\,\middle|\,\phi_1^i\right\rangle\right|
\end{aligned} \tag{2.4}$$

With this matrix element, the *local* character of NEXAFS is evident, since just the very localised initial core state ϕ_1^i and the unoccupied orbital have to be considered.

Hitherto, the total wave function has been considered without going into the individual components such as spin– or vibronic wave function. In chapter 2.3, the vibronic part will be described in more detail.

2.3 Franck–Condon Principle

Separating the vibration

In the framework of the Born–Oppenheimer approximation [37], the total wave functions can be written as the product of the nuclear wave function and the electronic wave function, since the positions of the nuclei are considered fix during the electronic excitation process. This assumption is well fulfilled, since the core hole lifetime is in the order of 10^{-15}s [5]. Therefore it is assured that NEXAFS probes the spatially undistorted molecule, in contrast to, e.g. optical spectroscopy. However, the nuclei may already start to move within this time frame and thereby cause the localisation of the core hole [35, 38].

$\vec{R} = \left(\vec{R}_1, \ldots, \vec{R}_M \right)$ and $\vec{r} = (\vec{r}_1, \ldots, \vec{r}_N)$ are thereby the positions of the nuclei and the electrons, respectively:

$$|i\rangle = \phi_{el}^i(\vec{r}) \cdot \psi_{nuc}^i\left(\vec{R}_0\right) = \left|\phi_{el}^i \psi_{nuc}^i\right\rangle$$
$$\text{and} \quad |f\rangle = \phi_{el}^f(\vec{r}) \cdot \psi_{nuc}^f\left(\vec{R}\right) = \left|\phi_{el}^f \psi_{nuc}^f\right\rangle$$

(2.5)

$\vec{R}_0$ denotes the equilibrium position vector of the nuclei in the ground state. Also in equation (2.3), the nuclear part ψ_{nuc} can be separated since the momentum operator $\hat{p}$ affects the electronic part ϕ_{el} only:

$$P_{if} \sim \left\langle \phi_{el}^f \psi_{nuc}^f \middle| \vec{e}\hat{p} \middle| \phi_{el}^i \psi_{nuc}^i \right\rangle \cdot \delta\left(\hbar\omega - E_a - n \cdot E_{vib}'\right)$$
$$= \underbrace{\left\langle \phi_{el}^f \middle| \vec{e}\hat{p} \middle| \phi_{el}^i \right\rangle}_{K} \cdot \underbrace{\left\langle \psi_{nuc}^f \middle| \psi_{nuc}^i \right\rangle}_{FC} \cdot \delta\left(\hbar\omega - E_a - n \cdot E_{vib}'\right) \qquad (2.6)$$

If a vibration couples to the electronic transition, a series of vibronic peaks will be observed at excitation energies

$$\hbar\omega = E_a + n' \cdot E_{vib}'$$

where E_a is the adiabatic energy, the difference of the vibrational ground states of the initial and final state, E_{vib}' the spacing of the vibrational levels n' in the electronic excited state. The intensity distribution of the individual peaks is determined by the vibrational part FC, the Franck–Condon factors, that will be described in the following.

Franck–Condon principle

Figure 2.2 depicts the nuclei potential curves of a diatomic molecule AB in the ground state, and two electronic excited states $AB^\star$ with the respective vibronic levels. On the right hand side, the intensities for the respective *vibronic* transitions from the vibronic ground state are depicted. This intensity distribution is determined by the overlap of the vibronic wave functions of the ground state $(n = 0)$ and the different vibronic wave functions in the electronic excited states $(n' = 0, 1, 2, \ldots)$. These overlaps correspond to the nuclear term FC in (2.6) and are referred to as the Franck–Condon factors.

Depending on the bonding character of the excited state orbital[1], the respective potential curve is shifted in equilibrium distance R_0 and shaped differently. For a non–bonding state (figure 2.2, middle curve), the main overlap of vibrational wave–functiony occurs for the vibrational ground state $n' = 0$, since the shift in equilibrium distance ΔR is small. Consequently, the main peak is found at the adiabatic energy (E_a) with only one additional peak, $h\nu'$ at higher energy.

In case of an anti–bonding orbital in contrast (figure 2.2, upper curve), higher vibronic levels have the largest overlap, the intensity of the 0–0 transition, however, decreases. The maximum of the progressions envelope is now at E_v, the energy of the vertical transition. The difference to the adiabatic energy E_a

$$\Delta E_{FC} = E_v - E_a \tag{2.7}$$

is referred to as the Franck–Condon shift. In the NEXAFS spectra, ΔE_{FC} is derived from the 0–0 transition (first peak) and the maximum of the envelope of the progression.

Franck–Condon analysis

The coupling of vibrations to electronic transitions is observed in NEXAFS spectra of numerous large organic molecules [5]. From the vibronic structures, it is possible to gain more information on the system and, in the present case, especially on the changes that occur upon condensation. Thus, a detailed fit analysis has to be performed as will be described in the following. The fitting program used for this analysis has originally been written by Lennart Kilian for the object oriented framework *root* [39] and further developed.

For small Franck–Condon shifts, i.e. non–bonding orbitals, the Franck–Condon factors may be approximated by a Poisson distribution, which passes into a Gaussian distribution for larger values of ΔE_{FC} [40]. To avoid the discomfort of different approximations, the FC factors are determined by calculating the overlap of Hermite polynomials, which present a solution of the Schrödinger equation for the harmonic oscillator [40]. The change in potential shape due to the electronic excitation is accounted by shifting (sh) and scaling (sc) the internuclear distance R of the ground state potential V_i:

$$V_i(R) = \frac{1}{2}k\left(R - R_0\right)^2 \rightarrow V_f(R) = \frac{1}{2}k\left(sc\left(R - R_0 - sh\right)\right)^2. \tag{2.8}$$

Since no *absolute* values can be given for the potential curve, the vibronic energy $h\nu$ in the excited state is an additional fit parameter.

---

[1]In contrast to photoemission spectra, in NEXAFS the initial– as well as the final state orbital have to be considered for the anti–, non–, or bonding classification. The nomenclature therefore refers in this case to the bonding type of the final state in respect of the initial state.
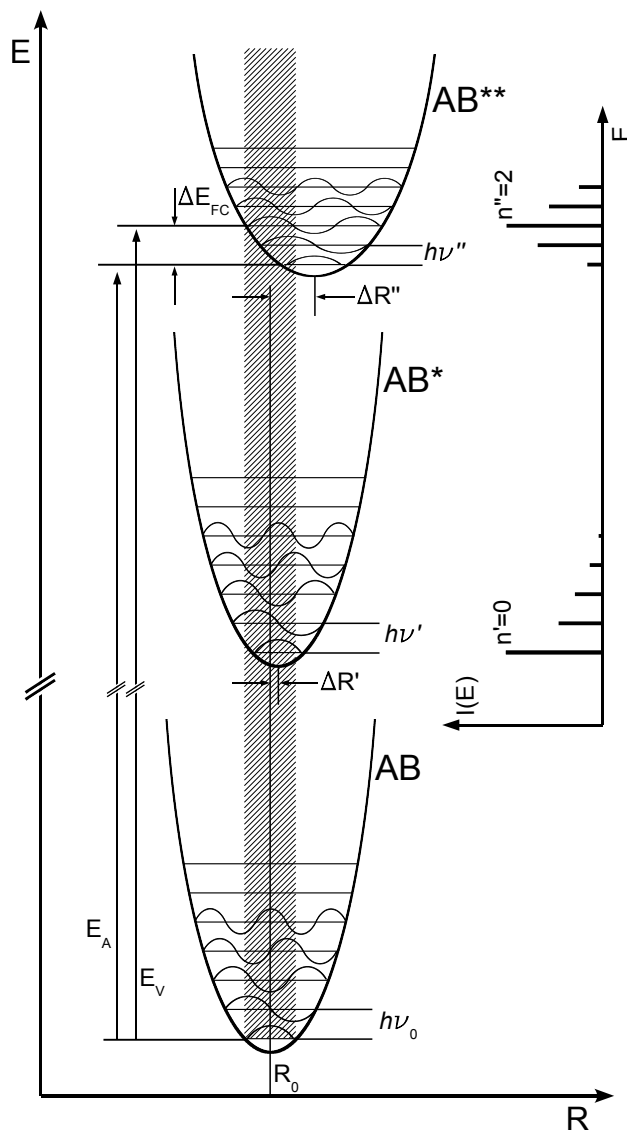
Figure 2.2: The Franck–Condon principle for a diatomic molecule AB in different electronic states $AB^\star, AB^{\star\star}$. E_V and E_A is the vertical and the adiabatic transition energy respectively, ΔR the change in equilibrium distance. The hatched area depicts the dimension of the vibronic ground state $n = 0$ of AB. At the right hand side the intensity distribution for the individual vibronic lines is sketched.

The individual peaks of the progressions are Voigt peaks with Gaussian (Γ_G) and Lorentzian (Γ_L) contribution to the total line width. Finally, each progression needs a transition energy (*pos*) and an intensity (*int*). Altogether one progression is described by 7 individual parameters, independent from the actual number of individual peaks. Compared to already 4 parameters ($pos, int, \Gamma_G, \Gamma_L$) for only one Voigt peak, this number is small. For similar electronic transitions, some parameters, especially the line widths, may be coupled and thereby the total number of parameters further decreased. In most cases, the line shape can be deduced from the leading edge of the progression and then used as fixed parameter for the whole feature.

Additional corrections as asymmetric peaks, or anharmonic potentials can easily be incorporated, but are of course increasing the parameter set. For some FC–fits an anharmonicity constant ξ has been used:

$$E_n = \left(\tfrac{1}{2} + n\right) h\nu + \xi \left(\tfrac{1}{2} + n\right)^2 h\nu^2.$$

In order to correctly assign the observed and fitted vibration to a normal mode of the molecule, the ground state vibronic energy $h\nu_0$ has to be determined. Based on the semi empiric formula derived for valence band photoemission spectra [6], $h\nu_0$ can be calculated with the Franck–Condon shift (2.7):

$$E_v - E_a = 1.2 \left(\frac{h\nu_0}{h\nu} - 1\right), \tag{2.9}$$

$$\rightarrow h\nu_0 = h\nu \left(\frac{\Delta E_{FC}}{1.2} + 1\right). \tag{2.10}$$

Although (2.9) has been derived from photoemission spectra of small molecules, it can be very well applied to NEXAFS spectra of most large organic molecules as is shown in chapter 5.6.

2.4 Special aspects in gas phase NEXAFS

What do we measure with NEXAFS in gas phase and solid state? The intensity of an incident photon in an absorptive material at depth x is given by

$$I(x) = I_0 \exp\left[-\alpha x\right] \quad \text{with} \quad \alpha = \alpha(E).$$

Although NEXAFS stands for near–edge x–ray *absorption* fine structure, the signal that is measured in solid state and our gas phase experiments is not an absorption signal. Unlike, for example optical absorption spectroscopy or, to stay in the same energy range, scanning transmission X–ray microscopy (STXM), where

the transmitted signal is measured directly, NEXAFS measurements depend on indirect detection channels.

For solid state measurements the sample current or total (photo) electron yield (TEY) is used for detection in general. The recorded signal is then

$$I_S = k \cdot (I_0 - I(d))$$
$$I_S = kI_0 \left(1 - e^{-\alpha d}\right). \tag{2.11}$$

Since the proportionality factor k, which links the intensity I to the measured signal I_S is unknown, we cannot solve equation 2.11 for the desired coefficient of absorption α. Fortunately, the mean free path of the (high energy) photoelectrons in the organic material is very small (a few nanometres) [41] and they cannot escape from deeper layers without losses. Consequently, the signal I_S resembles just the absorption in the first few layers of the organic film. For a small exponent αd we can expand the exponential function using the Taylor series:

$$I_S = kI_0 \left(1 - \left(1 - \alpha d + \frac{(-\alpha d)^2}{2!} + \dots\right)\right) \tag{2.12}$$

$$I_S \simeq kI_0 \cdot \alpha d \quad \text{for small } \alpha d \tag{2.13}$$

So we end up with a linear dependency between the absorption coefficient α and the measured signal I_S.

In case of gas phase measurements, the total ion yield is collected throughout the gas cell. If we now imagine an infinitely long gas cell for our absorption experiment, the total ion yield, measured along the whole cell, would be independent of α and therefore also independent of the photon energy. Even with a very small α, all photons, regardless of which energy, will be absorbed sooner or later in the infinite absorption volume. Since there is no limiting factor, as the electron escape depth in case of the solid state, all ionised molecules will reach the electrode and contribute to the total ion yield signal. The recorded signal will just resemble the flux curve of the beamline.

For a *finite* absorption volume, however, we still need to ensure that the absorption is 'small enough'.

Compared to the solid state, the coefficient of absorption α is much smaller in the gas phase. At the same time, the absorption length d, that is now the length of the absorption volume, is several orders of magnitude larger. Therefore we cannot, as a matter of principle, assume the product αd still being small enough for the Taylor expansion to be valid.

At least we can estimate an absorption range which is still appropriate for an acceptable error. For an absorption of 10% ($I(x)/I_0 = 0.9$) for example, the approximation (2.13) differs from the real value (2.11) by 5%. Assuming this is the

highest absorption in the spectrum, the peak will be 5% too small compared to the background. As a rule of thumb, this is, in our view, still tolerable.

Note that the error made by this expansion does not scale linearly with the absorption coefficient. Regions with high absorption, e.g., the NEXAFS resonances, will be affected more than the average background.

The way to tackle this issue experimentally, is described in detail in chapter 3.4.

In order to gain the absorption coefficient from equation 2.13, the initial intensity I_0 present in the absorption volume is needed. The experimental realisation is described in detail in chapter 4.1.

2.5 NEXAFS Calculations

In order to reliably interpret NEXAFS spectra, it is very helpful to also consider theoretical calculations of the NEXAFS process. Although many codes exist for the calculation of the electronic configuration in the ground state, codes for excited states, especially in the presence of a core hole, are still rare. In addition, if intermolecular interaction has to be taken into account, no standard codes are available. In the following, the methods for calculating NEXAFS spectra used in this work will be outlined shortly. At the end of the chapter the individual methods are compared using the example of 1,4,5,8–naphthalene–tetracarboxylic acid dianhydride (NTCDA).

Z+1 calculations

The major challenge of calculating NEXAFS spectra ist the presence of the core hole. In most methods the core hole would be filled upon energy minimisation. The simplest way of getting around this issue is the so called 'Z+1' or 'equivalent core' approximation [42]. At the atomic site of the excitation, the atom is replaced by the next higher element of the periodic table. A carbon atom for example is replaced by a nitrogen atom. When calculating the electronic configuration of the cation, there is an excess of positive charge localised at the substituted atom that will simulate the core hole. The whole electronic system will react to this charge and reorganise.

Since the substituted atom has a very different core level energy, the energy of the 1s level in the ground state has to be used as a reference for the transition energy. Still the resulting energies are far too high and need to be shifted in energy to resemble the experimental data. To obtain the transition intensities, the output files of the ground state core level and the excited orbitals, containing volumetric data of the wave function, can be used. Alternatively, transitions may be classified as visible or not–visible simply by examination of the respective excited orbitals by eye.

Of course, these are very crude approximations: The equivalent core will be screened differently compared to an actual core hole, the negative charge in the

excited orbital is neglected, and the intensity calculation does not precisely include the polarisation. In spite, the results are precise enough to reasonably assign the individual transitions to the experimental spectra. Most important, the electronic levels of the excited states can be calculated conveniently using standard quantum chemical programs.

The Z+1 calculations in this work have been performed with Gaussian03 [43], using a Hartree–Fock functional with a 6–31G(d,p) basis set. This basis set even allows calculations incorporating next neighbours within a reasonable time frame. Table 2.1 shows NTCDA orbitals, table 2.2 the respective energy levels calculated with two different basis sets (6–31G(d,p) and 6–311G++(2df,2pd)). As can be seen, no major differences are obvious in the orbital shape, and also the energy values for the excited levels are very similar. The Z+1 calculations have been primarily used to visualise the excited state orbitals (see chapter C).

GSCF3 code

For most calculations used for the peak assignment, Kosugi's GSCF3 code [44–46], which is optimised for core excited states, has been used. This *ab initio* method accounts for the core hole effects by the improved virtual orbital (IVO), also known as static exchange approach or frozen core approximation [47]. In this approach, the core states and occupied molecular orbitals are optimised in the presence of the core hole in a first step. As second step, all these orbitals are kept constant (frozen) and the excited electron is introduced to the respective unoccupied orbital. Still keeping the occupied levels constant, the unoccupied orbitals are optimised in energy. However, due to the limited basis set available, it was not possible to reliably calculate molecules with their next neighbours present.

WAVELS code

In order to integrate models that may describe the solid state effects observed in the experimental spectra, a more flexible code was needed. The WAVELS code package, an *ab initio* code originally developed for calculating Auger electron spectroscopy (AES) spectra [48], is a good basis for this task. The excitonic coupling, as described in chapter 2.6.2 has already been implemented as a first approach to the solid state effects [49]. Thus, it is now possible to investigate the eventual coupling of the nearest neighbours in the excited state on a theoretical basis. The implementation of configuration interaction (CI) and dispersive forces is currently in progress and is expected to additionally shed light on the intermolecular interaction. For the first time, a code is available that is capable of reproducing various solid state effects responsible for the difficult changes that are observed in NEXFAS spectra upon solid state formation.

Table 2.1: Excited molecular orbitals of NTCDA, calculated in Z+1 approximation with two different basis sets.
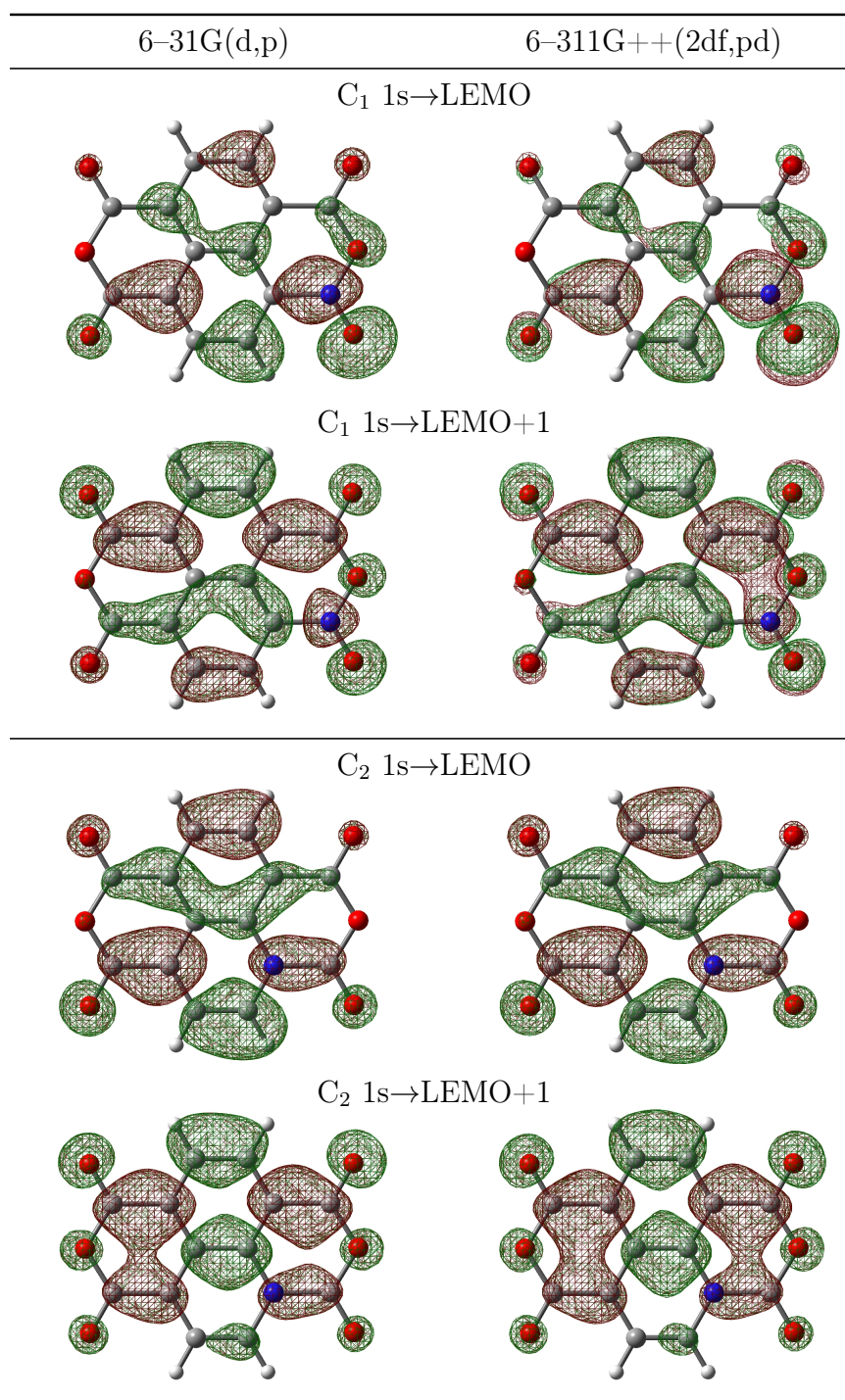
6–31G(d,p)	6–311G++(2df,pd)
C_1 1s→LEMO	

C_1 1s→LEMO+1

C_2 1s→LEMO

C_2 1s→LEMO+1

Table 2.2: Comparison of Z+1 calculations of NTCDA C_1 orbital energies with different basis sets. The respective orbitals are plotted in table 2.1.

MO	6–31G(d,p)	6–311G++(2df,pd)
C_1 69	563.09	562.93
C_1 70	565.38	565.13
C_1 71	566.90	566.55

Calculations for NTCDA

Using the example of NTCDA, the results of the different calculations have been compared. For all three calculations the resulting absolute value of the transition energy is too high. This is caused by an overestimation of the core hole and by the limited basis sets. Since the minimisation of orbital energy is more difficult for higher orbitals, the mismatch in energy is increasing with the orbital number. For a better assignment to the experimental data, the theoretical energy scales are therefore shifted and compressed in the respective data plots (for example see figure 5.12).

In figure 2.3 the results for the NTCDA C–K edge using the Z+1 (top), GSCF3 (middle), and the WAVELS code (bottom) are displayed. While the GSCF3 and the WAVELS codes yield very similar results of energy position and transition intensity, the Z+1 calculations differ significantly. Especially in the transition energies, the crude approximations of this method, as described before, become evident. The intensities, however, are quite comparable.

In general, the energies resulting from the WAVELS code are smaller. Especially the transition of the C_3 at $291.5\,\mathrm{eV}$ is significantly lower. This can be related to the mixed–Rydberg character of the respective orbital (see also chapter C, NTCDA $C_3 \rightarrow$L+4). The energy of the wide spread orbital is probably minimised more effectively by the WAFELS code.

This comparison shows that the WAFELS code produces the most accurate values, but that the Z+1 calculations are also suitable for a global peak assignment.

For a comparison of different basis sets, excited state orbitals for the C_1 and C_2 atom are plotted in table 2.1. The higher basis set (6–311G++(2df,2pd)) provides an additional primitive gaussian basis function for the valence AO (31**1**), diffuse functions for heavy and hydrogen atoms (++), and higher angular type of basis functions (**d, f**). Compared to the 6–31G(d,p) basis set, the computational time is increased by a factor of about 40. The results, however, are not very different compared to the much simpler basis set. Just for the C_1 L+1 and C_2 L+1 orbitals a somewhat improved delocalisation at the excited atom is evident. Also the excited state energy levels are very similar for both basis sets as can be deduced from table 2.2. In summary, at least for visualising the excited state orbitals, the simple

6–31G(d,p) basis set is sufficient. For more advanced calculations including next neighbours, the larger basis set would probably be sensible, but is just too demanding in computational power.
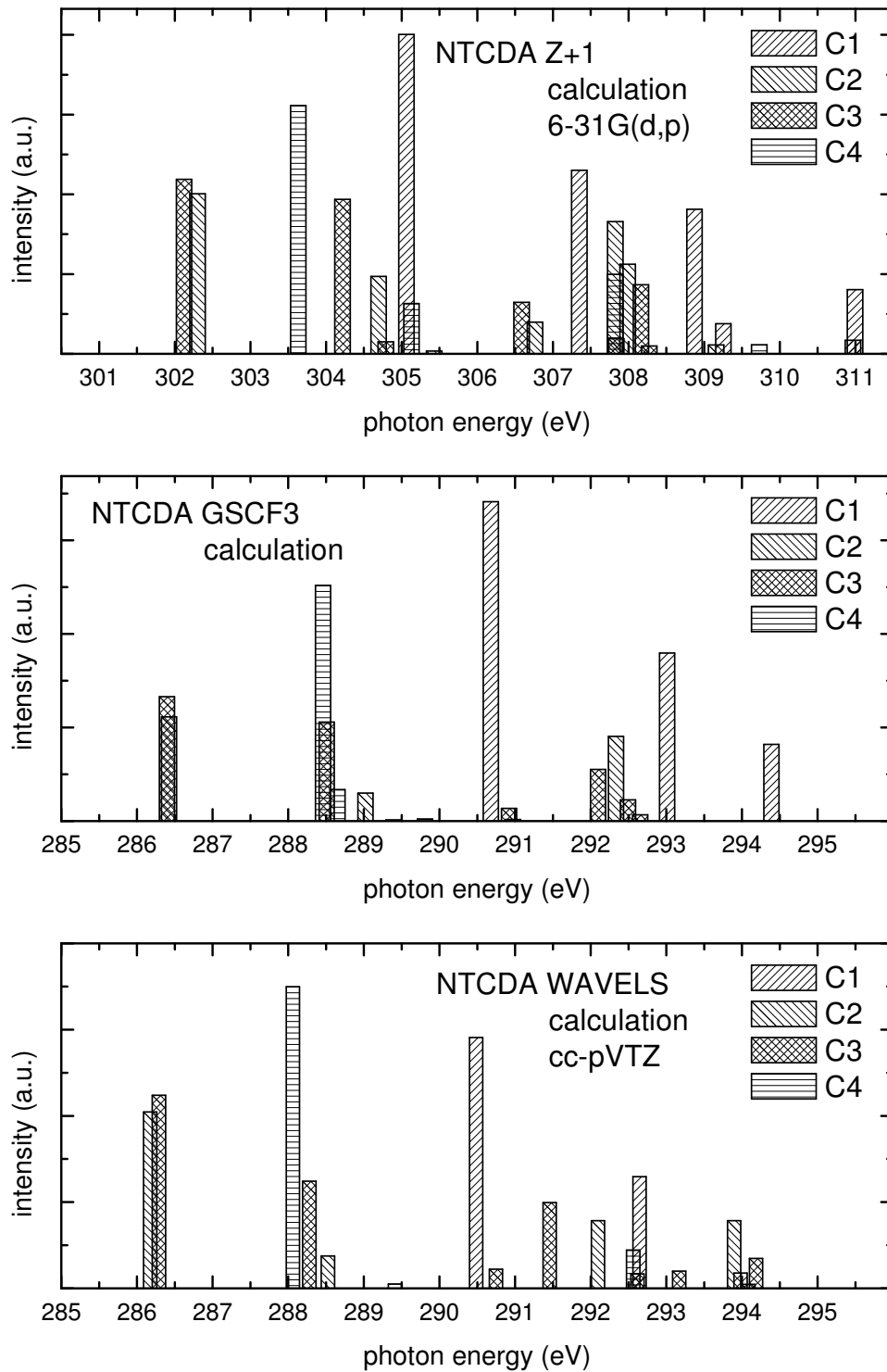
Figure 2.3: Comparison of calculated NEXAFS spectra with Z+1 (top), GSCF3 (middle), and WAVELS (bottom) codes.

2.6 Theoretical models to explain the experimental findings

In this chapter, different models will be introduced that may describe the effects occurring when molecules condense or aggregate and start to interact with each other. Most classical models of ground state interaction via dispersive and van–der–Waals terms will most probably fail to explain the differences observed for gas– and solid phase NEXAFS. General shifts may be readily explained by these theories, but not differential shifts of individual transitions, since marked differences between the individual atoms in a molecule are evident not until the excitation process spotlights a certain atomic site. In addition, the interaction in the excited state can be expected to be much more efficient compared to the ground state. Therefore, interactions in the excited state need to be considered in particular.

The proposed models for intermolecular interaction are all inherited from optical spectroscopy. In spite of the same basis of a coupling a molecule in the excited state with another one in the ground state, the specialities of the NEXAFS process must not be neglected. The chemical selectivity and localised excitation need to be considered in particular.

2.6.1 Coupling wave functions

In this section, the interaction of neighbouring molecular orbitals already in the ground state shall be considered using the very basic example of a two level system corresponding to a molecular dimer. In the molecular crystal, the situation is of course more complicated due to the numerous orbitals that need to be considered. The basic principle, however, is the same.

When two orbitals approach each other, they will start to interact with each other even before they come closer than their van–der–Waals radii. If the ground state of the system is considered only, this situation can be described with perturbation theory for a two level system [50].

The unperturbed system can be described by the two eigenstates Ψ_1^0 and Ψ_2^0 and the ground state Schrödinger equation

$$\hat{H}^0 \Psi_m^0 = E_m^0 \Psi_m^0 \text{ with } m = 1, 2$$

with E_1^0 and E_2^0 being the ground state energies. Under the influence of the perturbed Hamiltonian, the two orthogonal eigenstates will couple, which is described by the linear combination of the original wave functions

$$\Psi = a_1 \Psi_1^0 + a_2 \Psi_2^0 \text{ with } \hat{H} = \hat{H}^0 + \hat{H}^1, \tag{2.14}$$

and the two eigenvalues $E_\pm$ of the perturbed system

$$E_\pm = \tfrac{1}{2}\left(E_1^0 + E_2^0\right) \pm \tfrac{1}{2}\left(\left(E_1^0 - E_2^0\right)^2 + 4\varepsilon^2\right)^{1/2}. \qquad (2.15)$$

Besides the ground state energies E_1^0 and E_2^0, we find the energy term $\varepsilon^2 = \left|\hat{H}_{12}^1\right|^2$, which resembles the interaction energy of the coupled states. Since the interaction energy is part of the splitting term, a stronger perturbation, i.e. more closely packed molecules, will cause a larger splitting of the levels.

The largest shift for the respective levels is achieved if the two ground state energies are equal. The splitting is then $E_+ - E_- = 2\varepsilon$.

For non–degenerate levels, when the interaction energy is small compared to the level difference, the lower level is shifted down and the higher level is shifted up:

$$\text{for } \varepsilon^2 \ll \left(E_1^0 - E_2^0\right)^2$$

$$E_+ \approx E_1^0 - \frac{\varepsilon^2}{\Delta E^0} \text{ and } E_+ \approx E_2^0 + \frac{\varepsilon^2}{\Delta E^0}$$

$$\text{with } \Delta E^0 = E_2^0 - E_1^0$$

In the case of degenerate levels, the resulting wave functions of the perturbed system are a 50% mix of the unperturbed wave functions:

$$\Psi_+ = \tfrac{1}{\sqrt{2}}\left(\Psi_1^0 + \Psi_2^0\right) \qquad \Psi_- = \tfrac{1}{\sqrt{2}}\left(\Psi_1^0 - \Psi_2^0\right) \qquad (2.16)$$

For the non–degenerate ground state levels, only a small part of the other wave function is added

$$\Psi_+ \approx \Psi_1^0 - \frac{|\varepsilon|}{\Delta E^0}\Psi_2^0 \qquad \Psi_- \approx \Psi_2^0 + \frac{|\varepsilon|}{\Delta E^0}\Psi_1^0 \qquad (2.17)$$

On the basis of this very simple two–level model, at least qualitative conclusions can be drawn for the interaction of orbitals of adjacent molecules.

The mutual alignment of the orbitals, as well as the shape of the molecular orbitals are crucial for the interaction energy (2.15) and therefore for the resulting split [51][2]. The largest effect is expected for a coupling of identical orbitals, e.g. LUMO–LUMO. Since the resulting orbitals are the sum and the difference of the original orbitals, respectively, they will differ significantly in their shape. In turn, for some transitions this can explain changes in peak intensity, which depends on the overlap of initial– and final state orbitals.

---

[2]This just refers to the theoretical part, the therein cited experimental data is not undoubtedly reliable.

Due to the energetic degeneracy of the individual orbitals, the interacting ones will be significantly different in energy. Therefore, a splitting can be explained. In addition, combined with the intensity argument before, also a mere shift in energy is possible.

2.6.2 Excitonic coupling

Especially in the process of excitation, not only the single molecule, but also the adjacent neighbours have to be considered. The individual molecular transition dipole moments may couple in presence of the incident electric field. In a quantum mechanical picture this is equal to a system with two coupled states: excitation either on one or the other molecule.

This excitonic coupling, or Davydov Splitting has been observed by means of spectroscopic ellipsometry, for pentacene and PTCDA for example, and is in the range of 120 and 40 meV, respectively [52, 53].

For simplicity, this excitonic coupling will be explained in the following by means of a dimer model, mostly following reference [54]. More detailed information can be found in reference [55].

The ground state of a dimer with identical molecules U and V is given by the wave function Ψ_G and the Hamiltonian $\hat{H}$:

$$|\Psi_G\rangle = |\psi_U \psi_V\rangle \tag{2.18}$$

$$\hat{H} = \hat{H}_U + \hat{H}_V + V_{UV} \tag{2.19}$$

ψ_U and $\hat{H}_U$ represent the ground state wave function and the hamiltonian for the isolated molecule U, respectively (same applies for molecule V). The intermolecular perturbation is described by the coulombic potential V_{UV}. Using the Schrödinger Equation $\hat{H}\langle\Psi_G| = E_G\langle\Psi_G|$ and (2.19), we obtain the ground state energy E_G:

$$E_G = E_U + E_V + \langle\psi_U\psi_V| V_{UV} |\psi_U\psi_V\rangle \tag{2.20}$$

E_U and E_V are the ground state energies of the individual molecules. The coupling between the molecules leads to a lowering in energy described by the third term, which is also referred to as *van–der–Waals interaction energy* [54].

In case of the excited dimer, wave functions with the excitation[3] on molecule U ($\psi_U^* \psi_V$) and on molecule V ($\psi_U \psi_V^*$) couple to

$$|\Psi_E\rangle = r |\psi_U^* \psi_V\rangle + s |\psi_U \psi_V^*\rangle \tag{2.21}$$

---

[3]Within the framework of the sudden approximation 2.2, ψ_U and ψ_U^* are orthonormal.

To determine the coefficients r and s, the Schrödinger Equation of the excited state has to be diagonalised:

$$\langle \psi_U^* \psi_V |\,,\; \langle \psi_U \psi_V^* | \; \cdot \Big|\; \hat{H} \,| \Psi_E \rangle = E_E \,| \Psi_E \rangle \tag{2.22}$$

$$\text{yields} \quad r\hat{H}_{UU} + s\hat{H}_{UV} = rE_E \quad \text{and} \quad r\hat{H}_{UV} + s\hat{H}_{UU} = sE_E \tag{2.23}$$

$$\text{with} \quad \hat{H}_{UU} \left(= \hat{H}_{VV}\right) = \left\langle \psi_U^* \psi_V \,\Big|\, \hat{H} \,\Big|\, \psi_U^* \psi_V \right\rangle \text{ and}$$

$$\hat{H}_{UV} \left(= \hat{H}_{VU}\right) = \left\langle \psi_U^* \psi_V \,\Big|\, \hat{H} \,\Big|\, \psi_U \psi_V^* \right\rangle \tag{2.24}$$

The non–trivial solution of the determinant of (2.23) yields the energy levels of our dimer system which is then expanded by using (2.24) and (2.19):

$$E_E = \hat{H}_{UU} \pm \hat{H}_{UV}$$
$$= \left\langle \psi_U^* \psi_V \,\Big|\, \hat{H} \,\Big|\, \psi_U^* \psi_V \right\rangle \pm \left\langle \psi_U^* \psi_V \,\Big|\, \hat{H} \,\Big|\, \psi_U \psi_V^* \right\rangle$$
$$= \left\langle \psi_U^* \psi_V \,\Big|\, \hat{H}_U \,\Big|\, \psi_U^* \psi_V \right\rangle + \left\langle \psi_U^* \psi_V \,\Big|\, \hat{H}_V \,\Big|\, \psi_U^* \psi_V \right\rangle + \langle \psi_U^* \psi_V \,|\, V_{UV} \,|\, \psi_U^* \psi_V \rangle \pm$$
$$\pm \left(\left\langle \psi_U^* \psi_V \,\Big|\, \hat{H}_U \,\Big|\, \psi_U \psi_V^* \right\rangle + \left\langle \psi_U^* \psi_V \,\Big|\, \hat{H}_V \,\Big|\, \psi_U \psi_V^* \right\rangle + \langle \psi_U^* \psi_V \,|\, V_{UV} \,|\, \psi_U \psi_V^* \rangle \right)$$

$$E_E = E_U^* + E_V + \langle \psi_U^* \psi_V \,|\, V_{UV} \,|\, \psi_U^* \psi_V \rangle \pm \langle \psi_U^* \psi_V \,|\, V_{UV} \,|\, \psi_U \psi_V^* \rangle \tag{2.25}$$

The third term is again the van–der–Waals relaxation energy, but now for the excited state. The difference

$$\Delta D = \langle \psi_U^* \psi_V \,|\, V_{UV} \,|\, \psi_U^* \psi_V \rangle - \langle \psi_U \psi_V \,|\, V_{UV} \,|\, \psi_U \psi_V \rangle \tag{2.26}$$

between ground and excited state will be negative due to the enhanced interaction in the excited state.

Together with the last term of (2.25) representing the exciton splitting energy

$$\mathcal{E} = \langle \psi_U^* \psi_V \,|\, V_{UV} \,|\, \psi_U \psi_V^* \rangle \tag{2.27}$$

and the excitation energy of the single molecule $\Delta E_{unit} = E_U^* - E_U$, we can express the energy needed for an excitation of the dimer as

$$\Delta E_{dimer} = \Delta E_{unit} + \Delta D \pm \mathcal{E}. \tag{2.28}$$

In the point–dipole point–dipole approximation , the splitting term (2.27) becomes

$$\mathcal{E}^\star = \frac{\vec{M}_U \cdot \vec{M}_V}{r^3} - \frac{3 \left(\vec{M}_U \cdot \vec{r} \right) \left(\vec{M}_V \cdot \vec{r} \right)}{r^5}. \tag{2.29}$$

Depending on the relative phase of the coupled transition dipoles $\vec{M}_U$ and $\vec{M}_V$, $\mathcal{E}$ will be added (in phase) or subtracted (out of phase) from the excitation energy (see table 2.3).

Expanding the scalar products in (2.29) yields a more descriptive expression that may be adjusted depending on the molecular arrangement.

For a coplanar alignment with the angle θ between the transition dipole moments and the line of molecular centres we get:

$$\mathcal{E}' = \frac{2\left|\vec{M}\right|^2}{R_{UV}^3} \cdot \left(1 - 3\cos^2\theta\right) \tag{2.30}$$

This yields a red–shift (blue–shift) for angles smaller (larger) than 54.7° as depicted in figure 2.4.

For the calculations performed for NTCDA (see chapter 5.5), the geometry part G of (2.29) is separated:

$$\mathcal{E}^\star = \left|\vec{M}_U\right|\left|\vec{M}_V\right| \cdot \underbrace{\left(\frac{\vec{n_U}\cdot\vec{n_V}}{r^3} - \frac{3\left(\vec{n_U}\cdot\vec{r}\right)\left(\vec{n_V}\cdot\vec{r}\right)}{r^5}\right)}_{G} \tag{2.31}$$

Atomic combinations that are likely to yield a high coupling, can be identified with this term. One has to keep in mind that, in contrast to the approximation in (2.29), the actual size of $\mathcal{E}$ strongly depends on the energy difference of the coupled states. The geometry factor is therefore calculated for pairs of chemically equivalent atomic sites on two different molecules only. In addition, the transition dipoles are assumed to be perpendicular to the molecular plane, and located directly at the respective atomic site.

As is shown in figure 5.24, this yields 16 terms for each of the C_1 to C_3 atoms, and 4 terms for the C_4 atom in case of NTCDA. Depending on the chosen neighbours, quite different geometry factors are possible.

Table 2.3: Phase relation of the transition dipole moments for some special molecular alignments. Given are the splitting term $\mathcal{E}$ and the intensity ratio $\frac{I_+}{I_-}$ of the in–phase $(+)$ and out–of–phase $(-)$ component.

mol. arrangement	$(+)$	$(-)$	$\mathcal{E}\,|r|^3$	$\frac{I_+}{I_-}$
in–line			$|M|^2$	2:0
stacked			$-2\,|M|^2$	2:0
angled			$0.5\,|M|^2$	1:1
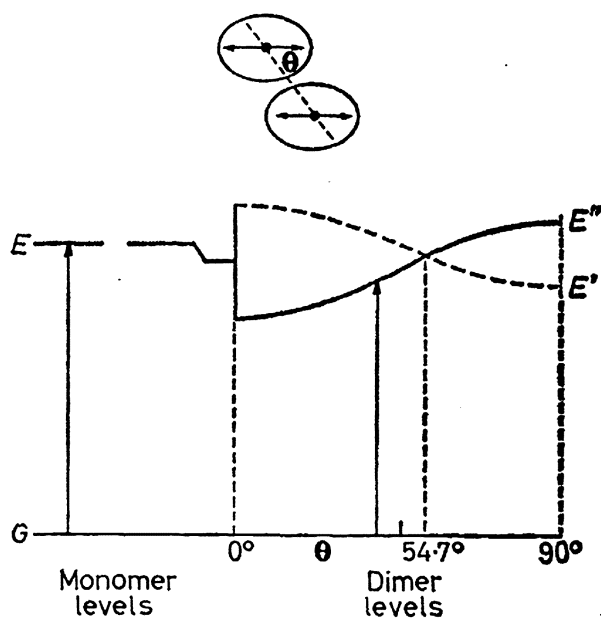
Figure 2.4: Dependence of splitting energy on mutual molecular alignment for co–planar inclined transition dipole moments. Taken from **(author?)** [54].

Gas Phase — Experimental

<div style="text-align: right">3</div>

As already outlined in detail in the introduction, the intermolecular interaction of large organic compounds is still not completely understood. To elucidate this interaction, we have chosen the most direct way by comparing interacting molecules in the solid state with their free counterparts in the gaseous phase. For the solid phase, numerous sets of high quality, high resolution NEXAFS data were already available from former investigations. In order to complete these sets with data of the gaseous phase, an experimental set–up was needed, providing gas phase NEXAFS spectra of comparable quality and resolution as for the solid state.

The experimental challenge of the present work was to eradicate the teething troubles of the recently built gas phase set–up. The following experimental part shall document the key issues and further development of the existing set up trying to exemplify the basic idea and requirements of our concept for better understanding intermolecular interaction.

3.1 Beamline Set Up

Unlike the existent gas phase experiments for organic molecules, the idea of the gas cell is to provide a long ionisation path through an organic vapour of high optical density. Consequently, the basic design is an enclosed volume that is entirely heated above the sublimation temperature of the organic compound under investigation and still compatible with the surrounding UHV conditions.

Figure 3.1 shows the latest set up of the gas phase experiment. In order to put a flexible and easy to adjust experiment into practice, the set up was designed to require as few space as possible. Thanks to the small outline of approximately 2 by 2 metres, the experiment can be placed behind any experimental chamber (EC) that features a flange to pass through the synchrotron beam. This allows a usage with existent experimental stations at various beamlines. The chamber of the gas cell is mounted on a stand with four degrees of freedom for adjustment. To provide compatibility with the respective vacuum requirements, a differential pumping stage ensures UHV conditions better than $5 \cdot 10^{-9}$ mbar at the experimental chamber even
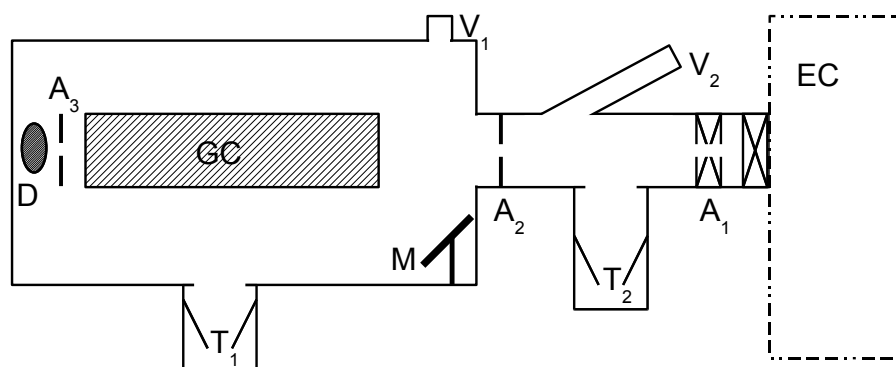
Figure 3.1: Sketch of the latest set up for gas phase measurements with apertures A_1 - A_3, viewports $V_{1,2}$, mirror M, gas cell GC, Si photo diode D, and turbo molecular pumps $T_{1,2}$ attached to experimental chamber EC.

if the pressure in the gas cell chamber rises above $5 \cdot 10^{-7}$ mbar. Aperture A_1 can be removed for alignment purposes.

The heart of the experiment, the gas cell (GC), is mounted in the main gas cell chamber. To facilitate the gas cell alignment, the 2nd aperture (A_2) of the differential pumping stage as well as the frame of the gas cell's front window are coated with ZnS. At a photon energy of $150\,eV$ the spot of the synchrotron beam can be observed very clearly. Through viewport V_2 one has view of the 2nd aperture, the front window of the gas cell can be observed through viewport V_1 and the mirror M.

At the end of the gas cell chamber a Si Photodiode (D) is mounted to monitor the transmitted signal behind the gas cell (see also chapter 4.1).

3.2 Gas Cell

Figure 3.2 shows an exploded view of the latest gas cell version and the new window design. The gas cell is made of a stainless steel tube (Ø5cm) sealed by welding on one side; the other end is sealed by a lid. Two Al windows at the front and at the back are used to pass through the incident synchrotron beam and separate the absorption volume from the UHV. Inside the cell, two electrodes are mounted to collect the ion and electron signal respectively. The plug on top of the cell can be opened with a rotationary feed through to avoid large pressure differences during pump down and venting.

3.2.1 Heating

To obtain a high x–ray absorption signal with high resolution and a high signal to noise ratio it is necessary to create a dense and stable atmosphere of gaseous
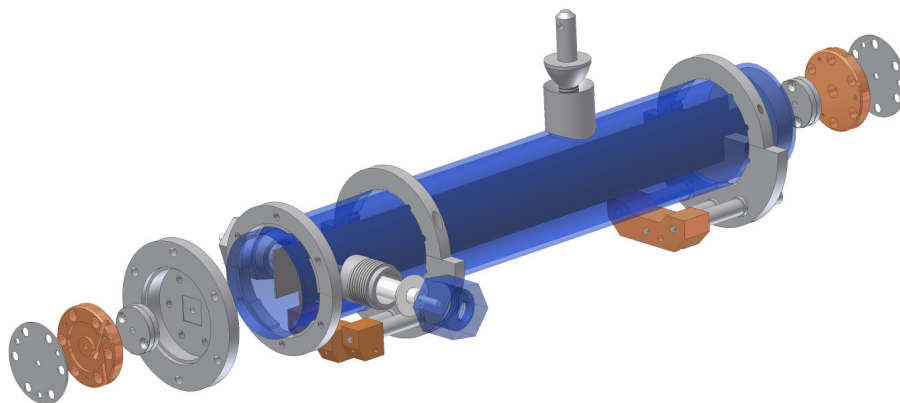
Figure 3.2: Technical sketch of the gas cell in the latest version. For details see text.

organic material within in the gas cell. Most organic molecules with a molecular weight larger than naphthalene (128 amu) have a very low vapour pressure at room temperature. To achieve a sufficient optical density in the absorption volume, the whole gas cell can be heated well above the sublimation temperature of the respective substance (380°C so far). To prevent disturbing magnetic fields, the resistive heating elements [56] are wound back and forth. If the cell temperature is throughout higher than the sublimation temperature, a dynamic equilibrium of organic material in the solid and gas phase is established. To ensure stable conditions during the measurement the temperature can be monitored at the rear window and at the gas cell mount.

The cell temperature is optimised with respect to count rate and saturation effects as explained in chapter 3.4.

3.2.2 Windows

The windows that separate the absorption volume from the surrounding UHV system and protect the beamline optics against contamination are the crucial point of the whole experiment. They need to withstand the pressure difference during pump down, the temperature gradients due to heating and, in case of reactive materials, chemical reactions induced by the organic molecules. Moreover, a small and preferably flat absorption coefficient is desired at the most interesting absorption edges (C, O, N. . .). Figure 3.3 shows the absorption coefficients in the interesting energy range for some elements that were considered as window material. Si compounds like SiN impress with a small absorption coefficient at the most important C–K edge and showed good resistance during pump down as well, but were not flexible enough to withstand the strain caused by the temperature gradients due to heating the cell. For higher heat tolerance and more flexibility, metal windows seemed to be the right choice. Unfortunately, the more rigid metals also have a higher absorption

Figure 3.3: Transmission of potential window materials with a thickness of 0.2 μm, dependent [58] on incident photon energy in the range of the interesting absorption edges (C–K, O–K, and N–K).
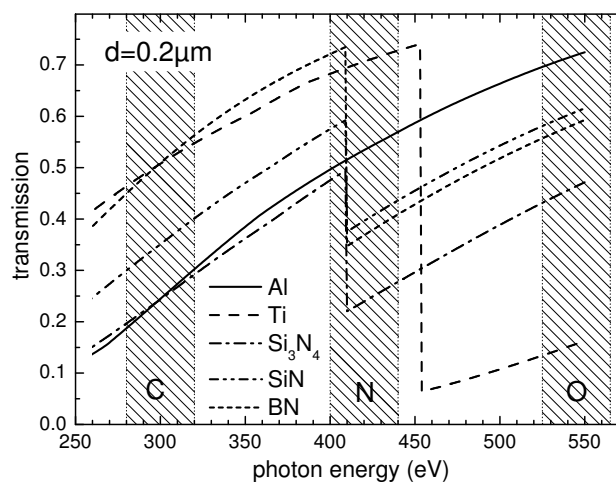
coefficient especially in the low energy range. On the other hand most metals can be fabricated in thinner quality.

In an upgrade of the gas cell we replaced the Cu–Al sandwich windows [16] by an 0.15-0.2 μm thick aluminum foil supplied and mounted in rigid stainless steel frames by Lebow Company [57]. This more rugged design is easier to handle and much easier to store. This window design proved its capability to withstand the temperature gradients as well as the pressure differences during pump down. Moreover, aluminum is chemically passivated and is thus more suitable for experiments with reactive molecules. Nevertheless, the windows have to be stored under inert atmosphere or in vacuum. The drawback of this protective oxide layer, the influence on spectra at the oxygen edge, is described in chapter 4.1. As can be seen in Figure 3.3, the absorption coefficient of Al is rather flat at all relevant edges. A 0.2 μm thick Al foil for example transmits about 20-30% of the incident light intensity through the first window at the carbon edge. At the oxygen edge the absorption is even smaller (ca. 30% transmission) which is convenient since oxygen atoms are only found in the functional groups of the organic molecules under investigation and therefore provide a relatively weak signal.

In the dynamic solid/vapor equilibrium, organic material is deposited everywhere in the cell. To avoid erroneous absorption signals from condensed layers of the organic substance on the aluminum foil, the windows need to resemble the hottest point of the gas cell. Therefore the window mounts (see figure 3.2) can be heated separately by additional heating elements and are in general set to a temperature about 50 K higher than the rest of the gas cell.

Using the example of NTCDA, figure 3.4 shows the effect of contaminated windows. In spectrum a), the main features are compressed and show a larger line width. This is due to the decreased incident light intensity caused by the absorption of the organic layers on the windows. With the window temperature high enough,
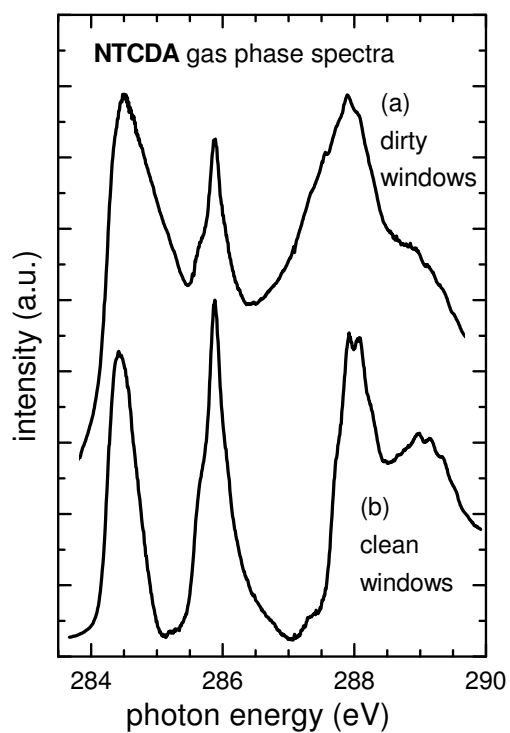
Figure 3.4: NTCDA C–K edge NEX-AFS: Effect of contaminated windows on spectral shape: Organic material adsorbed on Al–windows (a) and clean windows at higher temperature (b).
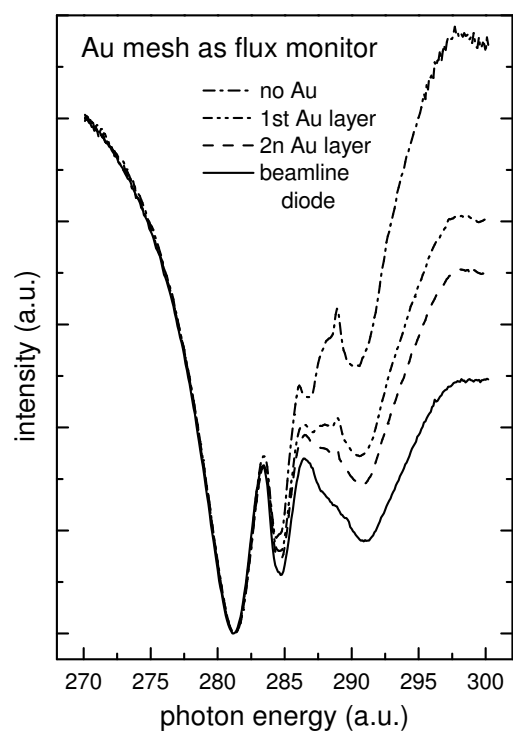
Figure 3.5: Beamline flux–curve at the C–K edge: Effect of contaminations from the gas cell on the Au–mesh flux monitor.

the windows are free of organic material and the correct gas phase spectrum b) is recorded.

In order to protect the beamline optics in case of a window failure, we used the $0.15\,\mu m$ foil for the rear window as a kind of predetermined breaking point. In case of an overpressure in the gas cell, the thinner rear window would break and thus protect the more important front window. The retreat of course is the lower transmission of the thicker front window.

3.3 Flux & Transmission

As described in chapter 2.2, the recorded total ion yield (TIY) spectra have to be normalised to the flux of the incident x–ray beam. In the experiments on intermolecular interaction we are looking for very tiny differences in intensity and energy positions between solid state and gas phase spectra. The normalisation process of the NEXAFS spectra can not only influence the intensity of the spectra, but also, in case of sharp features in the flux curve, alter the energy positions of peaks or peak onsets. Therefore it is essential to treat all aspects, starting from a reliable flux signal up to the normalisation process itself, with special care.

For solid state experiments the spectrum of the clean substrate is often used for this normalisation [59]. In case of the gas phase experiments we used the GaAs photodiode of the beamline for recording the flux curve. Although the characteristics, or the photon–to–electron conversion ratio of a photodiode depend on the photon energy, it can be considered as constant in the region of a NEXAFS spectrum ($\simeq 30\,eV$). This procedure works out very well for some energy ranges.

At the carbon edge, where heavy carbon contaminations often cause pronounced dips in the flux curve [59], it is hard to reliably normalise spectra using this technique. Even slight discrepancies in the photon energy scale of measurement and flux curve can alter the spectra significantly. Particularly the first feature of most aromatic molecules is thereby affected heavily. These shifts in photon energy mostly occur during an injection if the electron orbit changed slightly. Another source of error is the changing heat load at the optical elements of the beamline during warm up, after injection or a temporarily closed beam shutter. The longer the period of time between measurement of flux curve and spectrum, the more probable and larger these shifts are.

To eliminate these sources of error, a flux monitor recording the I_0 signal *simultaneously* is required.

In the first set up we used the sample current of a tantalum sheet with freshly evaporated gold to monitor the transmitted signal. However, the gold film was covered with organic material shortly after by the contaminations from the gas cell. Due to the small mean free path (escape depth) of the photoelectrons, most signal was therefore caused by the organic adsorbates on the surface. Even several

cycles of evaporation of fresh gold can not extinguish the signature of the organic substance from the flux curve entirely.

Also a gold mesh in front of the gas cell turned out to be unfeasible as a flux monitor, also due to the continuous contamination caused by the gas cell. Figure 3.5 reveals the effect of the contaminations even with freshly evaporated Au layers.

Both methods turned out as not suitable for the normalisation process.

To skirt this issue, a Si photodiode (Hamamatsu S1226–8BK, glass cover removed) was put behind the gas cell. Since the short–circuit current I_{SC} is generated within the p–n region where the synchrotron radiation is absorbed, the contaminations on the surface can be neglected. Without the glass cover, the photodiode is also sensitive to infrared radiation. To minimise perturbing contributions from the hot gas cell, the angle of acceptance of the diode is limited to the actual window size by an aperture. After subtracting this dark current the signal from the diode is suitable for the normalisation process (see chapter 4.1) even though the signal to noise ratio (SNR) is not good enough for a direct use as absorption spectrum. The transmission signal is also used to keep track of the contamination on the windows and the self absorption as described in the following chapter.

3.4 Self Absorption

The self absorption is an issue implicated by the new design of the gas phase experiment. Measurements in the molecular beam yield, as well as solid state measurements[1], a signal just from a small absorption region i.e. a very tiny part of the sample (see also chapter 2.4). With increasing density of the organic atmosphere, the intensity of the synchrotron beam will decrease significantly along the ionisation region. This effect is proportional to the absorption coefficient of the organic material at a certain photon energy. Therefore the main features of the spectrum will be affected in particular since they represent the maxima in cross section. The resulting spectrum will therefore show compressed main features similar to those in figure 3.4.

In order to keep the error below 5%, the absorption of the gas phase must not exceed 10% (see estimation in chapter 2.4). Features with high absorption can be directly observed by comparing the actual transmission signal with one of the cold gas cell. If these features are in the range of a few per cent, the influence of the self absorption is negligible.

In the transmission spectrum of PTCDA for example a dip caused by the CO contamination can be seen at 287.3 eV (see figure 3.6). Although the peak in the spectrum is very prominent, the absorption dip is only about 5% and therefore still tolerable.

The self absorption of the gas phase and the contaminated windows alter the NEXAFS spectrum in a similar way. To distinguish between the two of them, one

---

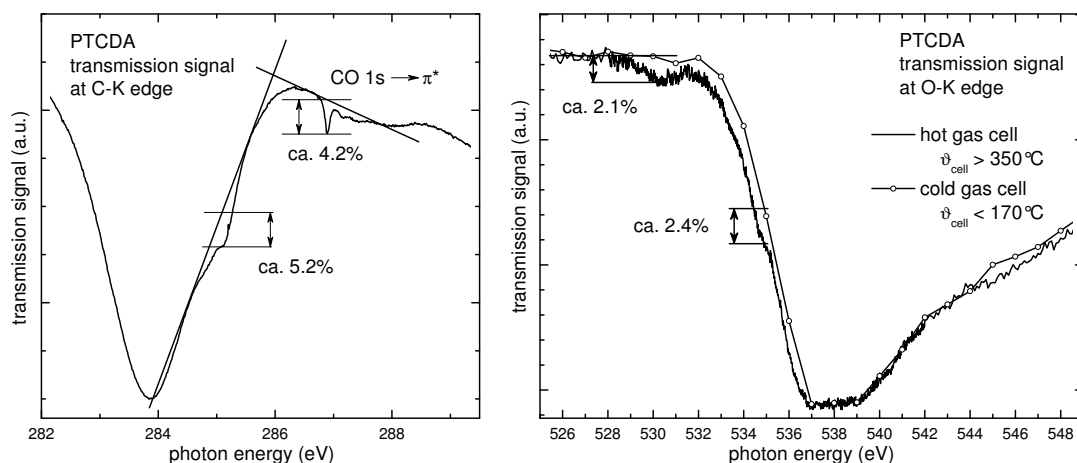[1]In that case due to the small escape depth of the photoelectrons.

Figure 3.6: Test for self absorption for PTCDA C–K (left) and O–K (right) edge.
PTCDA and CO signatures are well below 10% limit for absorption.

can elevate either the window or the gas cell temperature while keeping the other temperature constant. From the behaviour of the dip in the transmission signal one can deduce whether the windows or the organic vapour itself is absorbing too much intensity.

3.5 Data Acquisition

The NEXAFS spectrum is recorded using the TIY signal from one electrode. To extract possibly all ions generated in the absorption volume, a bias voltage is applied to the electrodes. It turned out that the built in bias voltage of the source meter causes a huge leakage current in the range of nA. This is due to a shunt resistance caused by the organic material covering the electrode mount and the electrode feed–through (figure 3.2)). To minimise this leakage current, one electrode was biased positively with a battery box (50-100V). The electric field then pushes the positive ions onto the opposing electrode which is connected to common ground by a Keithley picoamperemeter. With this set up, the TIY signal is in the range of several tens of pA.

3.6 Other Issues

Dark currents

Among this leakage current, we also observed a temperature dependent dark current during our first measurements. Different temperatures and materials at the chamber and the gas cell feed–through caused a thermoelectric voltage between the electrode

and common ground. This voltage would drive a current through the shunt resistance at the electrode feed–through.

To tackle this problem, a micro–volt decade was connected in series with the measurement circuit. While the beam shutter was closed, the compensating voltage was adjusted until the dark current was at a minimum. The remaining current offset was subtracted from the spectrum prior to normalisation. This adjustment was repeated for each measurement.

To avoid these dark currents all connections from the feed–through at the chamber to the gas cell have to be made of materials with the same or at least similar contact potential (see also chapter 3.7).

Contaminations

Gas phase measurements in the molecular beam, as performed for benzene–tetra-carboxylic acid dianhydride BTCDA for example, often suffer from contamination with water. The water resonances at the O–K edge coincide in many cases with the features of the functional group and complicate the analysis of the spectra (see chapter 5.2.1). With the gas cell setup in contrast, the organic material looses most of its water of crystallisation during the bakeout of the vacuum chamber. Therefore the water contamination is minimised considerably as has been shown for NTCDA for example (see section 5.3.1).

Admittedly, in the recorded spectra of PTCDA additional peaks appeared in the C–K NEXAFS spectrum during the measurement (see chapter 5.4.2). Because of the very sharp signature, fragments of PTCDA molecules seemed unlikely. The structure fits very well the NEXAFS signatures and energies of CO and CO_2. These contaminations stem from the stainless steel of the gas cell which precipitates carbon oxides especially at high temperatures [60]. To reduce this outgassing, the empty cell should be baked in UHV at very high temperature and then stored under vacuum or inert gas atmosphere. This will prevent the stainless steel from soaking again with CO and CO_2 under ambient conditions. Nevertheless, the CO contamination had the advantage of providing an excellent calibration point for the C–K edge. Recorded simultaneously, energy shifts between measurement and calibration are excluded. As depicted in figure 5.18, the CO signal at the C–K edge could be subtracted from the PTCDA spectrum successfully and results in a spectrum with still high–quality.

The situation at the O–K edge, however, is more complicated. Figure 3.7 (top) displays the original PTCDA gas phase spectrum which is completely buried under contaminations starting from 533 eV. In contrast to the C–K edge, here the broad CO and CO_2 resonances overlap with each other and also with the PTCDA feature II. Thus it is not possible to just subtract the spurious spectra. Instead, the measured O–K spectrum is reassembled by different components: s– and p– polarised PTCDA solid state spectra, and reference spectra of the CO and CO_2 contaminations. The
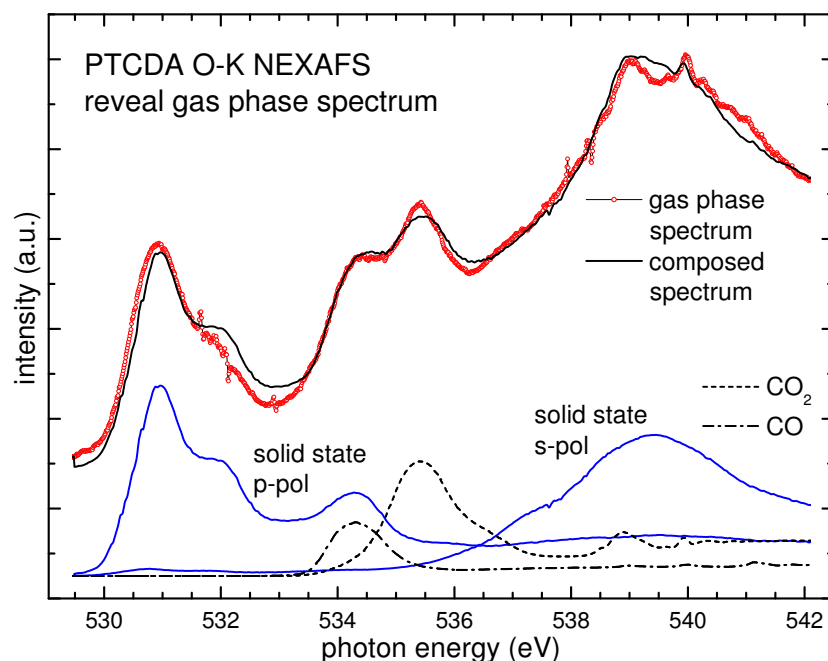
Figure 3.7: PTCDA O–K edge spectrum built up from components For the revealed
spectrum see figure 5.17.

intensity of each component and the energy position (within the uncertainty of
calibration) are adjusted using a least–square fit routine. In case of CO_2 it was even
possible to set the energy position fix since the very sharp feature at ca. 540 eV
provides an excellent point for (relative) calibration.

Since the whole spectrum extends over a large energy range, especially over 533 eV,
the transmission of the gas cell has to be taken into account either by the use of a
normalised gas phase spectrum, or by multiplying the components with the transfer
function of the gas cell windows. The composed spectrum will of course differ from
the measured spectrum due to the different background of the components and
differences in solid and gaseous PTCDA, which are the aim of the investigation.
Therefore no special weighing was used for the adjustment of the spectra.

Figure 3.7 shows the composed spectrum together with the individual components
in their actual scaling. The overall agreement is very good, considering the relatively
large energy range of 12 eV. The remaining discrepancies at the CO_2 resonance are
ascribed to differences in resonance widths.

By subtracting the contamination spectra from the original gas phase spectrum,
while accounting for the transmission function, the original gas phase spectrum is
revealed. The result is plotted in figure 5.17 and will be compared with the solid
state spectrum in detail in chapter 5.4.1.

Beam damage

Although the organic material within the gas cell is not replaced during measurement, no signs of beam damage were obvious. Even over a long period of measurements, the spectra of compounds investigated so far did not change in view of line shapes, relative intensities, or additional peaks. In contrast, some solid state samples are more sensitive to the high intensity x–ray beam and the generated photoelectrons.

3.7 Suggested Improvements

The gas phase experiment still is a very young project in our workgroup so there is still a lot of room for improvements.

Lock In amplifier

One of the major issues still is the leakage and dark current during the measurements. Even with the compensation described in chapter 3.5 there is still an undesired signal. The major difficulty is that the dark current is not constant over time. To eliminate this current we need a compensation method that allows the subtraction of a 'quasi constant' current. The answer to this problem is a lock in amplifier. It allows to differentiate between signal contributions that are dependent and those that are independent of the x–ray beam. The major challenge in putting this idea into practice is a chopper for the x–ray beam. It needs to be compatible with the UHV requirements. As examples for electrostatic tuning–fork choppers see references [61, 62]. Of course one will loose up to 50% of the signal, but since signal quality and not intensity is the key issue, this will not be the problem. This upgrade is highly recommended since it will have the best cost–benefit ratio.

Of course the major contribution of dark current — if still present — should nevertheless still be compensated using the micro–volt decade in order not to drive the preamplifier or the lock in amplifier into saturation.

Concurrent measurements

To further improve the reliability and correctness of the relative energy calibration (see chapter 4.2), measurements of both phases at the same time are desired. As **(author?)** [63] showed relative shifts as small as $6\,\text{meV}$ between gaseous N_2 and N_2 clusters could be resolved in simultaneously measured NEXAFS spectra. Of course we also should aim at such a high precision measurement. As we have seen in chapter 3.3, small organic contaminations on a gold grid can already yield a significant signal. Taking advantage of that issue, a gold grid with freshly evaporated organic material could be used as a solid state reference. Of course the resulting spectrum can neither in quality nor in structural information compete with thin

solid film spectra on single crystal substrates. But it is worth trying to eliminate the uncertainty in the calibration process.

Temperature control

Last but not least, the temperature control needs some improvement. Although the temperature of the gas cell will stabilise after some time it is recommended, especially for a temperature series, to control the temperature automatically. Using the EPII$^{\mathrm{therm}}$ could make a contribution to that, allowing several channels to be monitored at the same time. Yet it is unclear if the used proportional–integral–differential (PID) control is capable of this issue. Fortunately the control unit is not implemented in the instrument, so it can be updated very easily.

Data Evaluation

<div style="text-align: right; font-size: 3em;">4</div>

Due to the different signal sources, experimental set up, and detection methods, the standard procedures used for the solid state NEXAFS spectra [59] can not be applied for the gas phase measurements just like that. In the following sections the different steps of data handling for gas phase NEXAFS spectra will be explained.

4.1 Normalisation

As described in chapter 3.3, several signal sources are available for the normalisation of NEXAFS spectra. The partial electron yield (PEY) signal for solid state measurements, the beamline diode, and the gas cell diode or transmission signal all have their assets and drawbacks. The transmission signal of the gas cell diode is measured simultaneously with the NEXAFS spectrum and is therefore free of any inconsistencies regarding the photon energy. Thereupon it can be used as a crude I_0 for a first attempt to normalise the gas phase spectrum. Due to the small SNR of the transmission signal, the resulting spectrum has low–quality and the resonances will appear somewhat exaggerated since the transmitted signal is smaller in this energy range.

Still, the result is good enough to get an impression of the overall signature of the spectrum. Thereupon, the photon energy of the recorded flux curve of the beamline diode can be slightly adjusted ($\simeq \pm 50$meV) to match the transmission signal.

Figure 4.1 shows a NEXAFS spectrum of PTCDA at the carbon edge that has been normalised using the transmitted signal and the PEY signal of a clean silver substrate. The resulting spectra exhibit very good accordance in regions of low intensity. Especially at the outset, the spectra are nicely flat in both cases. At the resonances, the spectrum normalised with the transmitted signal has higher intensity due to the decreased transmission signal in this part of the spectrum. For higher energies, the PEY normalised spectrum shows increased intensity. This can be explained by a nonlinearity of the gas cell diode caused by an increase of the photon–to–electron conversion ratio with higher photon energy.

As already mentioned in chapter 3.2.2, the Al windows have a native oxide layer that might play a role for normalisation at the O–K edge. In the transmission
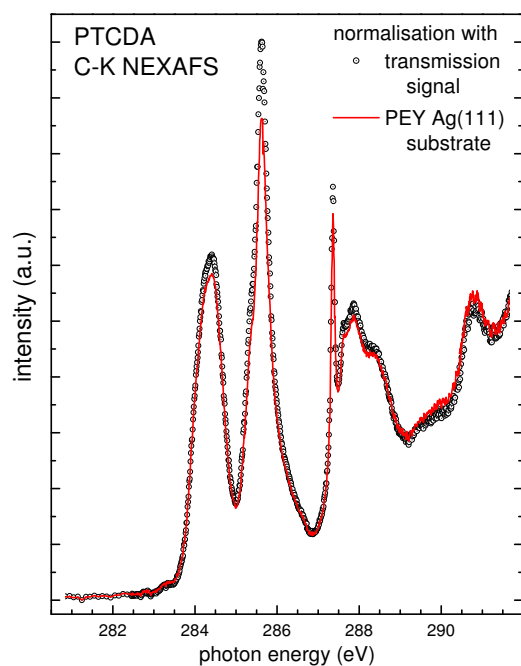
Figure 4.1: Different normalisation procedures for PTCDA gas phase NEXAFS at the C–K edge.
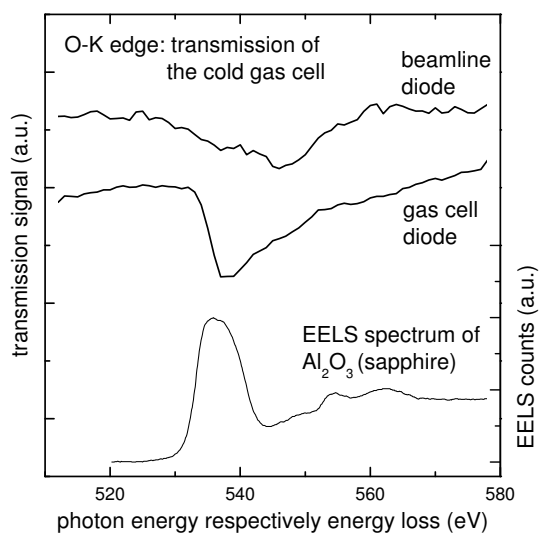
Figure 4.2: Transmission of the cold gas cell at the O–K edge. Gas cell diode signal compared to beamline diode signal. EELS data of Al_2O_3 digitised from Ref. [64].

signal of the gas cell a step occurs at about $536\,\mathrm{eV}$ which is much more pronounced compared to the flux curve measured with the beamline diode (see figure 4.2).

Fortunately, this step, caused by the Al_2O_3 resonance, is very broad ($7\,\mathrm{eV}$) compared to the features present at the oxygen edge for most organic molecules investigated so far. Therefore the structures of interest are affected marginally only. However, if comparing gas and solid state spectra in an expanded energy range this effect of course has to be taken into account. In combination with the flux curve measured with the beamline diode, the transmission of the clean cold gas cell can be used to calculate the flux present in the gas cell.

In order to achieve best results, not only concerning the normalisation, measurements of solid state and gas phase in direct succession are highly recommended. Almost identical beamline conditions for both phases allow a high quality comparison. Furthermore, normalisation of gas and solid state spectra using the same flux curve will also improve the quality of the comparison. In addition, a very small relative error in photon energy is achieved and of crucial importance for the detailed comparison of gas and solid state spectra.

4.2 Calibration

Some effects of the intermolecular interaction on the spectral signature can be derived by comparing gas and solid state spectra with comparable high quality. Changes in intensity distribution or fine structure give a hint which orbitals of the molecules are affected by the solid state formation. Such interpretations do not require an exact energy calibration of the two spectra.

A plausible interpretation of, e.g. differential shifts in various NEXAFS resonances, however, requires reliable information about the point of origin of these energy shifts. As observed for, e.g. NTCDA (see chapter 5.3) effects caused by the intermolecular interaction are in the range of 100meV. In order to recover these small shifts, the accuracy of the photon energy calibration needs to be significantly better.

For an *absolute* energy calibration this is hard to achieve, since the accuracy of literature values is worse in many cases. For the CO $1s \rightarrow \pi^*$ transition for example, a sharp resonance commonly used for gas phase calibration, values ranging from $287.3\,\text{eV}$ to $287.4\,\text{eV}$ at the C–K edge and from $533.1\,\text{eV}$ to $534.11\,\text{eV}$ at the O–K edge can be found in literature (references [65–67]). In addition, most gas phase references are based on electron energy loss spectroscopy (EELS) measurements.

Since solid state samples are often calibrated to substrate photoemission lines (in the present work mainly Ag^{3d} lines), a comparison of the two phases was infeasible within an error of better than $80\,\text{meV}$.

Therefore we recorded the CO and CO_2 NEXAFS spectra at the C– and O–K edges, calibrating them to the Fermi edge of a clean Ag(111) substrate. Thus we created a common base for energy calibration of our gas phase and solid state measurements. The calibration values we achieved for CO and CO_2 are in good agreement with the values measured by **(author?)** [68].

In most cases a very high accuracy of the *absolute* energy calibration is not required since only the relative shifts occurring upon condensation are of interest. In fact, a *relative* calibration between the two phases is sufficient and, to a certain extent, easier to achieve.

If measured subsequently, the deviation in photon energy between gas and solid state measurement is in the range of $\simeq 20\text{meV}$. This deviation resembles that of the backlash of the undulator and monochromator from one measurement to the succeeding. Of course this method is challenging since two measurements have to be prepared at the same time, but the gain in accuracy is worth the effort.

In case of ANQ we have been able to accomplish such measurements at the C–K edge. As displayed in figure 4.3, the second features of the two phases align within this error, whereas feature one and two show significant shifts in the range of $100\,\text{meV}$. Using this method the achieved accuracy in relative photon energy is satisfactory.

Nevertheless, this method is not resistant against sudden, admittedly seldom, changes in photon energy. For an even more exact and reliable interpretation, a
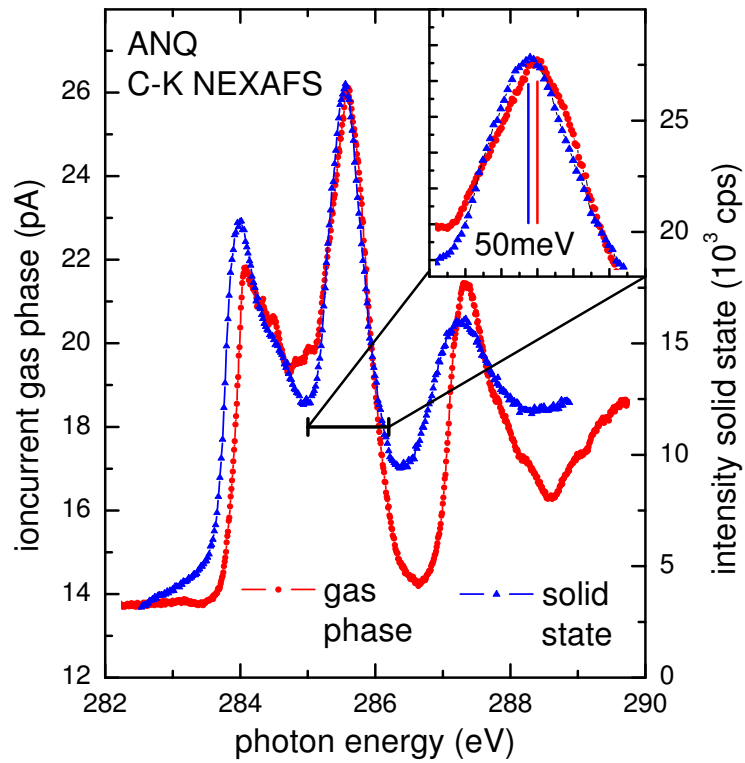
Figure 4.3: Raw data of ANQ gas and solid phase at the C–K edge. Both spectra
were measured subsequently. The shift of the second peak is in the order of
50 meV.

concurrent measurement of gas and solid phase, as suggested in chapter 3.7, is
desirable. No matter which method for calibration is used, the spectra always need
to be shifted in wavelength, not in energy, since the main error is introduced by the
beamline monochromator.

Results

5

In the following sections, results of gas phase and solid state measurements are presented. Principal effects of solid state formation on the NEXAFS spectra will be explained based on the results obtained for Alq$_3$.

Next, the results of the systematic investigation of the dianhydride–series BTCDA, NTCDA, and PTCDA, will be presented with the main issues on the effect of intermolecular interactions on the electronic structure of each molecular compound. The similarities and differences of the intermolecular interaction of the three dianhydrides will be discussed in detail afterwards, considering the theoretical models developed in chapter 2.6.

The chapter concludes with a consideration of the vibronic properties of large organic compounds that have been derived from the data of this and former investigations.

5.1 Alq$_3$

In the wide range of organic materials for organic electronics, tris (8–quinolinol) aluminum (Alq$_3$) surely is among the most important ones. It is often used in OLEDs because of its good electron and light emitting properties [70, 71]. Also due to its relevance in device physics, numerous fundamental investigations have been
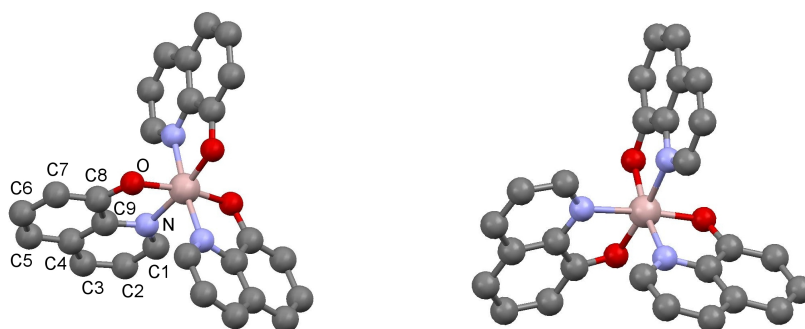
Figure 5.1: Alq$_3$ meridianal (left) and facial (right) configuration. In thin solid films, the meridianal configuration is present [69].

carried out, including UPS, XPS, and inverse photoelectron spectroscopy (IPES) studies of this workgroup [72–74]. The present investigation of gas and solid state aims at a better understanding of the properties of the unoccupied levels.

For Alq₃, two different isomers, the meridianal and the facial (see figure 5.1), and several crystal phases are known [75]. In thin films, amorphous growth of molecules in the meridianal configuration is observed [69, 75]. In spite of the asymmetry of the meridianal isomer, the atoms of the ligands may be considered as symmetrically equivalent [76]. Since only one O– and N–atom exists per ligand, very sharp single peaks are expected in the NEXAFS spectra at the O–K and N–K edges. This will simplify the interpretation considerably and makes Alq₃ a well suited compound to start the investigations.

For the O– and N–K edge, theoretical calculations yield transitions into the LEMO, LEMO+2, and LEMO+3. The LEMO+1 in contrast is not visible due to the absence of significant overlap of the orbital with the respective core level. For the C–K edge in contrast, transitions from the various carbon atoms into all four LEMOs are predicted [76].

The thin films for the solid state spectra shown in the following, have been prepared by organic molecular beam deposition (OMBD) on a cooled Ag(111) substrate (150K) and measured at room temperature. The gas phase spectra have been measured in the gas cell at 530K. For the C–K edge well resolved data with a high SNR have been obtained, the N–K and O–K edge however suffer from a much lower intensity since only three N and O atoms exist per molecule, respectively. Nevertheless, the recorded data is of good enough quality for a detailed comparison of the different phases. Note that due to the aluminum windows of the gas cell, the Al–K edge could not be investigated.

O–K edge

In figure 5.2, the gas phase– (left) and solid state (right) O–K NEXAFS spectra are plotted. The appearance of the π^* region with transitions into the LEMO (I) and LEMO+2 (II) is very similar for both phases. No evidence of fine structure is present in either phase. While the intensity ratio of the two π^* resonances is comparable, the relative intensity of the σ^* resonance (feature III) decreases in the solid phase. The signature of the leading edge of the gas phase σ^* resonance indicates subjacent fine structure. An unambiguous assignment of the observed shoulders to electronic or vibronic features, however, is not possible. This is not only due to the lack of theoretical calculations for this region [76, 77], but also due to the uncertainties with respect to energy and intensity (higher SNR) of the gas phase spectrum. In the solid phase, these structures are not visible, but a clear increase in intensity at the trailing edge of feature III is present.

The evaluation of the peak positions of feature I and II yields a decrease of the peak spacing from 2.0 eV in the gas phase to 1.76 eV in the solid state spectrum

Table 5.1: FWHM (given in eV) of the Alq$_3$ features at the O–K (I-II) and the N–K edge (A-C).

peak	gas phase	solid state
I	0.98	1.13
II	0.81	1.13
A	0.72	0.68
B	0.68	0.76
C	0.99	1.15

(see figure 5.2, insets). In turn, the II–III distance, which is admittedly not as exact to determine in the gas phase, increases by exactly the same amount from 5.2 to 5.45 eV. This means that the solid state formation is accompanied by a distinct, relative red–shift of 0.24 eV for the LEMO+2 transition. Also the increase of FWHM (see table 5.1) is more than twice as large for feature II compared to feature I. This is quite contrary to all observations for the O–K edges of the other molecules investigated in this work.

N–K edge

Also at the N–K edge, the gas phase and the solid state spectrum are very similar as depicted in figure 5.3. Even the shape and relative intensity of the σ^* feature (E) is comparable. In contrast to the O–K edge, the LEMO+2 (B) and LEMO+3 (C) transitions are not clearly separated, but appear as a double peak.

The energy difference between the features A (LEMO) and C (LEMO+3) of 3.56 and 3.52 eV for the gas phase and the solid state, respectively is identical within the error bar. To evaluate the position of feature B more exactly, a peak–fit is needed, especially for the gas phase data due to the significantly lower SNR. The resulting spacing of features B and C is 1.13 eV for the gas phase, and 1.23 eV in case of the solid state spectrum. In the solid phase, the FWHM of features B and C is increased by 12 and 16%, respectively, whereas for feature A a slight decrease is observed (see table 5.1).

As can be seen in the insets of figure 5.3, this close inspection also reveals a distinct asymmetry of both features and even a partly resolved fine structure (significant shoulders) in case of the solid state spectrum. Hence, the fitted peaks tend to overestimate the actual spacing of the features. Consequently, the resulting red–shift of 0.1 eV for the LEMO+2 transition has to be considered as an upper limit. Compared to the shift of 0.24 eV at the O–K edge, even this upper limit is still significantly smaller.
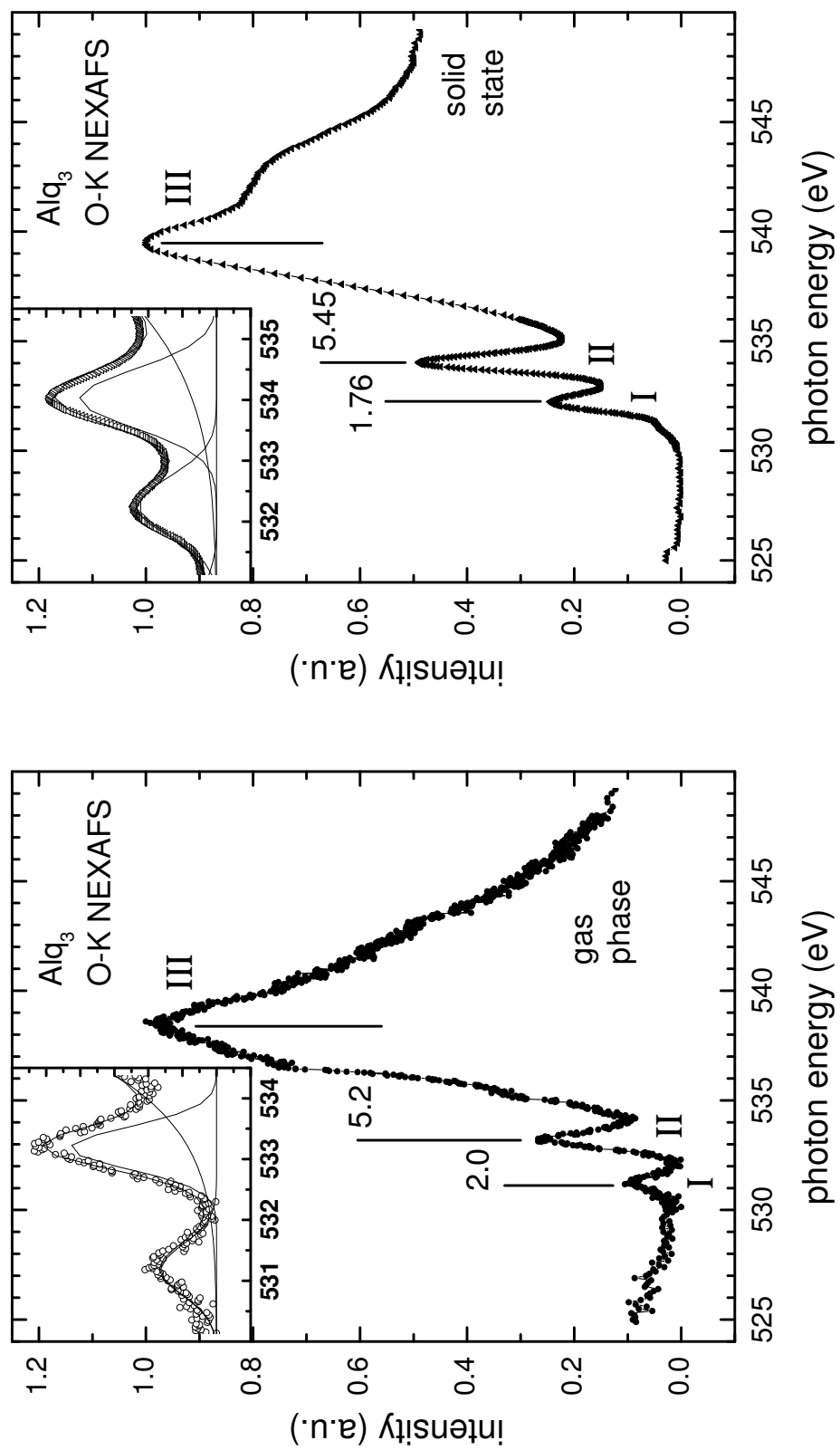
Figure 5.2: Alq₃ O-K edge in gas phase (left) and solid state (right). The insets show a detailed view of the peak fit for features I and II.
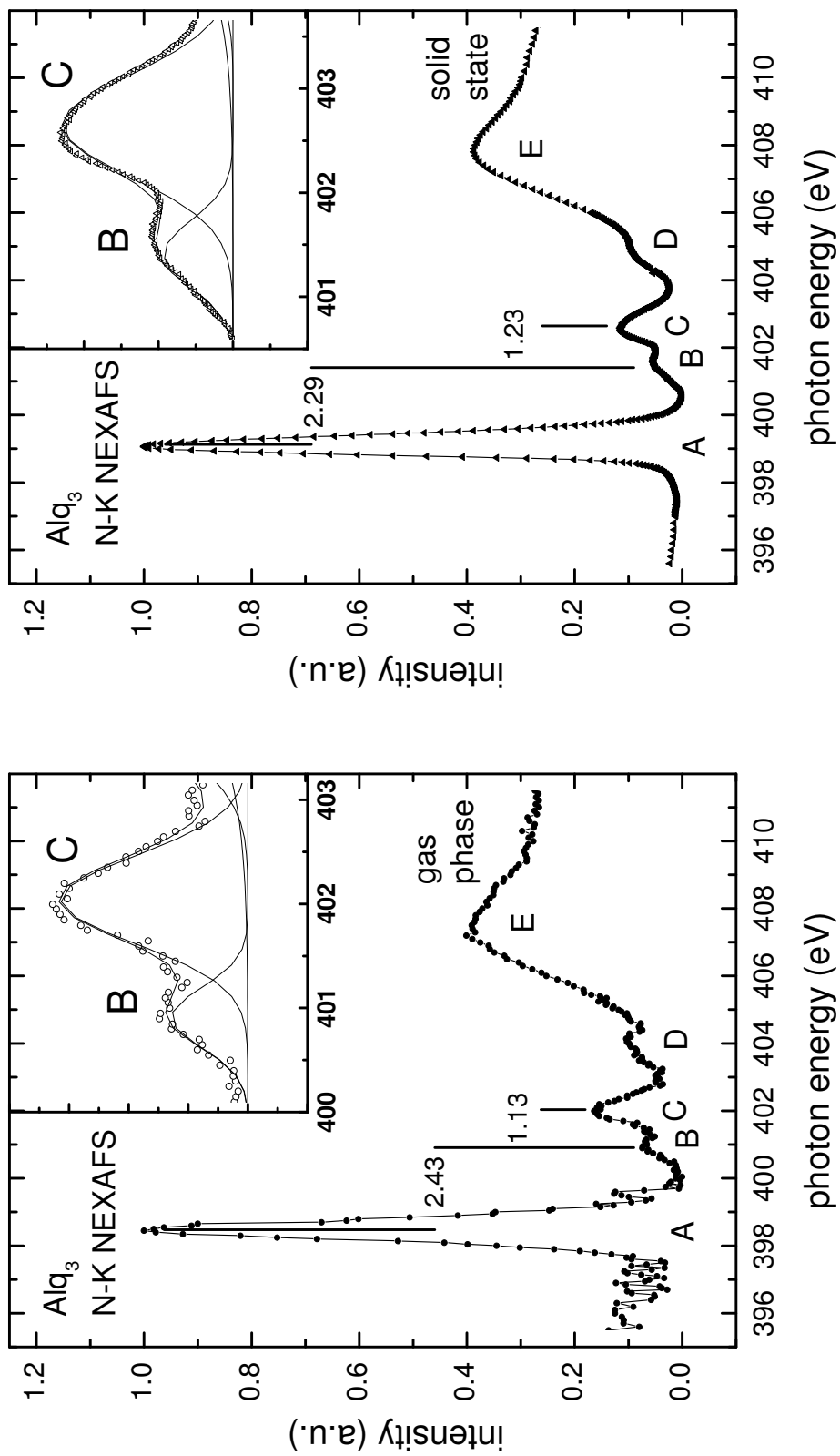
Figure 5.3: Alq₃ N–K edge in gas phase (left) and solid state (right). The insets show a detailed view of the peak fit for features B and C.

C–K edge

Finally, the C–K edge data of Alq₃ provide a nicely resolved fine structure with a very good SNR for both phases as can be seen in figure 5.4. According to theoretical investigations [76, 77], the broad feature α can be reproduced by pure electronic transitions from the various carbon atoms into the LEMO and LEMO+1. Most intensity stems thereby from the C_3 and C_5 atoms, respectively. Feature β can be assigned to transitions into the LEMO+2, with a main contribution from the C_8 atom. Observed differences between gas phase and solid state data are therefore exclusively of electronic origin.

With respect to the peak onsets of feature α, some peaks and shoulders shift by 0.04 to 0.13 eV towards higher photon energy upon solid state formation. This difference may partly arise from a large uncertainty in the determination of onset– and peak position. The most significant difference in the solid state spectrum is the low energy shoulder of the peak at 285.78 eV, which has no counterpart in the gas phase spectrum.

Since no other changes in intensity are observed in feature α, a shift of an individual electronic transition seems unlikely. An increase of transition probability for a LEMO+1 transition in contrast, is a more probable explanation for this main difference in feature α.

The width of feature β, derived from transitions into the LEMO+2, appears significantly decreased in the solid state spectrum, and is also shifted towards higher energy. With respect to the onsets of the spectra, this implies a blue–shift of 0.24 eV for the whole feature β upon condensation. This finding is quite exceptional, since no blue–shifts have been observed for the other molecules investigated in this work.

Summary for Alq₃

Alq₃ turned out as a well suited candidate to exemplify the correlations between experimental features (shifts and changes in intensity) and the possible causes (changes in core– and unoccupied states) of the NEXAFS gas– and solid phase investigations. The important advantage at the N– and O–K edge is the presence of symmetrically equivalent atoms of the same species. Consequently, pure transitions into the unoccupied orbitals are observed exclusively and can be assigned without ambiguity.

The differential shifts, primarily found for the transition into the LEMO+2, show that the observed solid state effects can not be caused by a mere change in core level energy. Otherwise, *all* other transitions at the respective atomic site would shift as well. For this particular orbital, changes at all three absorption edges (O, N, and C–K) are found. This shows nicely that the orbital structure is very important for the respective sensitivity to intermolecular interaction. Another speciality of this orbital is the pronounced change in full width at half maximum (FWHM) compared
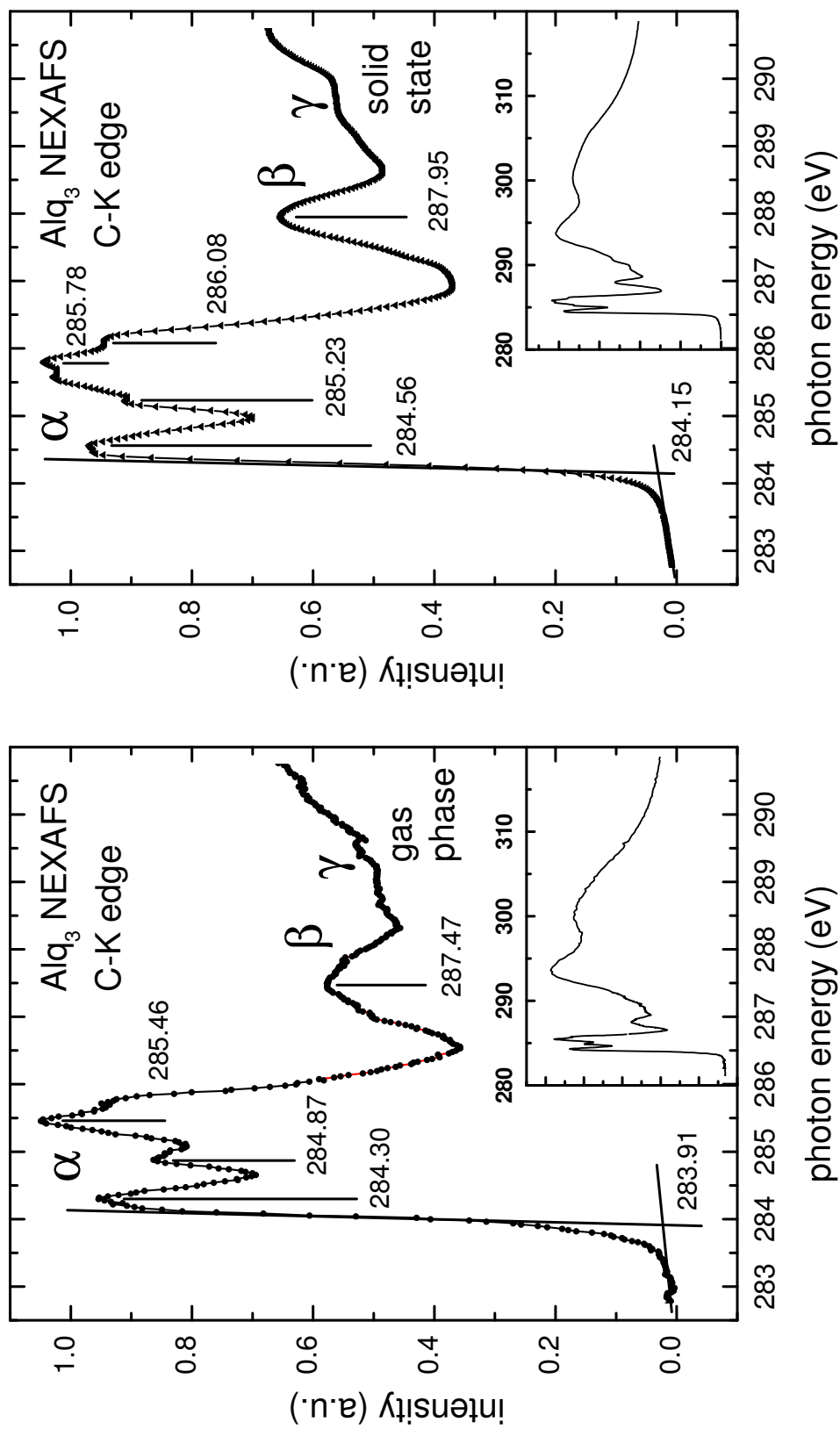
Figure 5.4: Alq$_3$ C–K edge in gas phase (left) and solid state (right). The insets depict an overview spectrum of the whole C–K edge.

to the other transitions. This finding demonstrates the sensitivity of resonance signatures to intermolecular interaction.

The different size of the differential shifts at the O– and N–K edge (0.24 and 0.1-0.14 eV red–shift) and the even opposite direction at the C–K edge (0.24 eV blue–shift) in turn reveal the importance of the interplay between core level, core excitation and the molecular orbital.

Compared to the dianhydrides discussed in chapter 5.5, only few, but relatively large changes are observed for Alq_3 upon solid state formation. In fact, investigations on Alq_3 by means of UPS [72] and optical spectroscopy [78] yield less pronounced differences between gas phase and solid state compared to, e.g., PTCDA or NTCDA [20, 26, 79]. The polarisation relaxation for example has been determined to 0.68 eV for Alq_3 which is significantly smaller compared to 1.2 eV for PTCDA. Also the UPS signature of the lower highest occupied molecular orbitals (HOMOs) is by far not as much altered as for PTCDA and NTCDA.

This investigation has clearly shown the special role of the LEMO+2 in the intermolecular interaction of this compound. Considering the shape of the LUMO+2[1], a localisation at the phenoxide side (closed to the oxygen) of the ligands is found. The other relevant orbitals have less intensity in this part (LUMO), or are evenly distributed over the whole ligand (LUMO+3).

Apart from that, the LEMO+2 resonance at the C–K edge also bears local information from this part since the main intensity stems from the C_5 atom. Therefore, the intermolecular interaction can be assigned to the phenoxide part of the ligands. In principle, a coupling of ground state orbitals would be a suitable explanation. However, the shift at the C–K edge in the *opposite* direction (blue–shift) points out the influence of the respective core excitation on the intermolecular interaction. Whether the molecules already interact in the electronic ground state or the interaction is essentially caused by the electronic excitation can therefore not be determined by these data alone.

5.2 BTCDA

As the smallest representative of the carboxylic acid dianhydrides we investigated BTCDA, also known as pyromellitic dianhydride (PMDA). BTCDA has one benzene ring as aromatic system, a molecular weight of 218 amu, and the free molecule belongs to the D_{2h} point group[2].

It has two chemically different oxygen atoms O_A and O_B, and three carbon atoms C_1 to C_3 in symmetrically nonequivalent sites (see figure 5.5). The small number of

---

[1]Because of lack of calculations for the excited orbitals, the unoccupied orbitals in the ground state [76] are used for discussion.
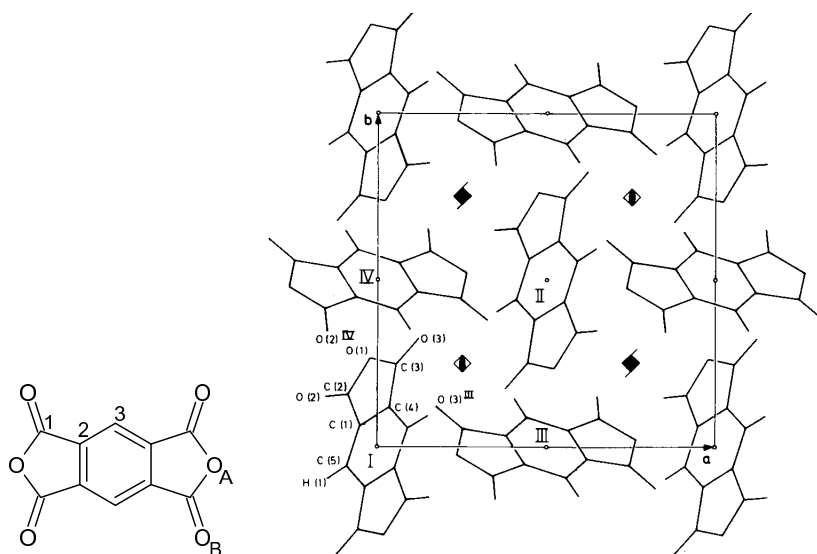
Figure 5.5: Left: Structural formula of BTCDA; labels denote symmetrically nonequivalent atoms. Right: crystal structure of BTCDA seen along c–axis, taken from Ref. [80].

different atoms shows great promise for a detailed investigation since the number of electronic transitions will be limited, too.

BTCDA crystallises in a tetragonal lattice ($P4_2/n$ space group) with four molecules per unit cell with basis vectors $a = b = 10.792$ Å, and $c = 7.4128$ Å. The normal of the molecular plane is tilted 53.3°, 42.8°, and 108.8° with respect to the a–, b–, and c–axis, respectively. The molecules stack along the c–axis with an interplanar distance of 4.43Å which is significantly larger than the sum of the van–der–Waals radii of carbon [80, 82, 83].

The gas phase data presented in this work have been measured at the *gas phase beamline* at ELETTRA with an evaporator temperature of approximately 420 K. The solid state spectra show a multilayer film on a Ag(111) substrate that has been cooled to 200 K during deposition. Neither at the C–K nor at the O–K edge any sign of polarisation dependence could be found. We can therefore assume that the multilayer film is of an amorphous or polycrystalline nature in this case.

Because of the different calibration mechanisms of gas and solid state spectra, the uncertainty in energy calibration is in the range of about 100 meV. Therefore we rather compare relative than absolute photon energies for this molecule (see also chapter 4.2).

---

[2](**author?**) [80] state a non–planar geometry for BTCDA as a free molecule. However, all calculations consistently yield the D_{2h} symmetry. Also (**author?**) [81] find different degrees of distortions for BTCDA in different compounds.

5.2.1 BTCDA O–K edge

Figure 5.6 shows the O–K NEXAFS spectra of BTCDA in the gas phase (top) and the solid state (middle). Calculating the NEXAFS spectrum of BTCDA at the oxygen edge turned out not to be straightforward since the GSCF3 code did not converge for the anhydride oxygen. Instead, the results of calculations using the 'Z+1' approximation are shown at the bottom of figure 5.6.

In the gas phase spectrum we find contaminations of H_2O that are unambiguously identified by the sharp feature at $537\,eV$ which is assigned to the H_2O O 1s→3p transition. Using digitised data from reference [84], the spurious contribution can be subtracted very successfully. The very distinct structure thereby gives a good indication for scaling and positioning of the H_2O spectrum. In figure 5.6 the corrected spectrum is plotted together with the H_2O and the original gas phase spectrum.

Due to the massive decrease in photon flux, caused by the shape of the monochromator harmonics, the quality of the gas phase spectrum decreases significantly above $537\,eV$. Still, the overall SNR of the gas phase spectrum is very good and will allow a detailed comparison with the solid state data.

If we now focus on the theoretical calculations and assign the calculated transitions to the respective resonances, we find that feature I is built up by a single electronic transition (1s→LEMO) at the O_B atom. Feature II in contrast, has contributions from two transitions arising from the O_B atom (to LEMO+1 and LEMO+2) and one transition from the O_A atom (to LEMO+1). The rising edge leading to structure III is built up by several transitions into the LEMO+3 and LEMO+4 at both oxygen atoms. The source for the main part of structure III however can not be identified exactly.

In both experimental spectra, no fine structure can be observed, but the asymmetry evident for all features indicates the subjacent, unresolved vibronic progressions coupling to the electronic transitions.

Comparing gas phase and solid state spectra, an increase of the FWHM[3] of about 20 and 10% is observed for feature I and II respectively. For the very broad structure III the FWHM can not be determined.

The energy gap between the onsets of the first two features agrees very well for both phases. In contrast, the peak–to–peak distance of the features increases by $0.2\,eV$ upon condensation. This shift is accompanied by a significant decrease of intensity and a change of shape of feature II. The fixed onsets, however, are a hint that the shift of the peak maximum is caused by a change of relative intensity of the subjacent progressions rather than by an energy shift of the whole feature. A similar change has also been observed for NTCDA (see chapter 5.3.1).

In the gas phase, the shoulder of structure III is very steep compared to the solid state spectrum. This change is most probably caused by a decrease of intensity

---

[3]FWHM have been determined by fitting single Gaussian peaks to each feature.
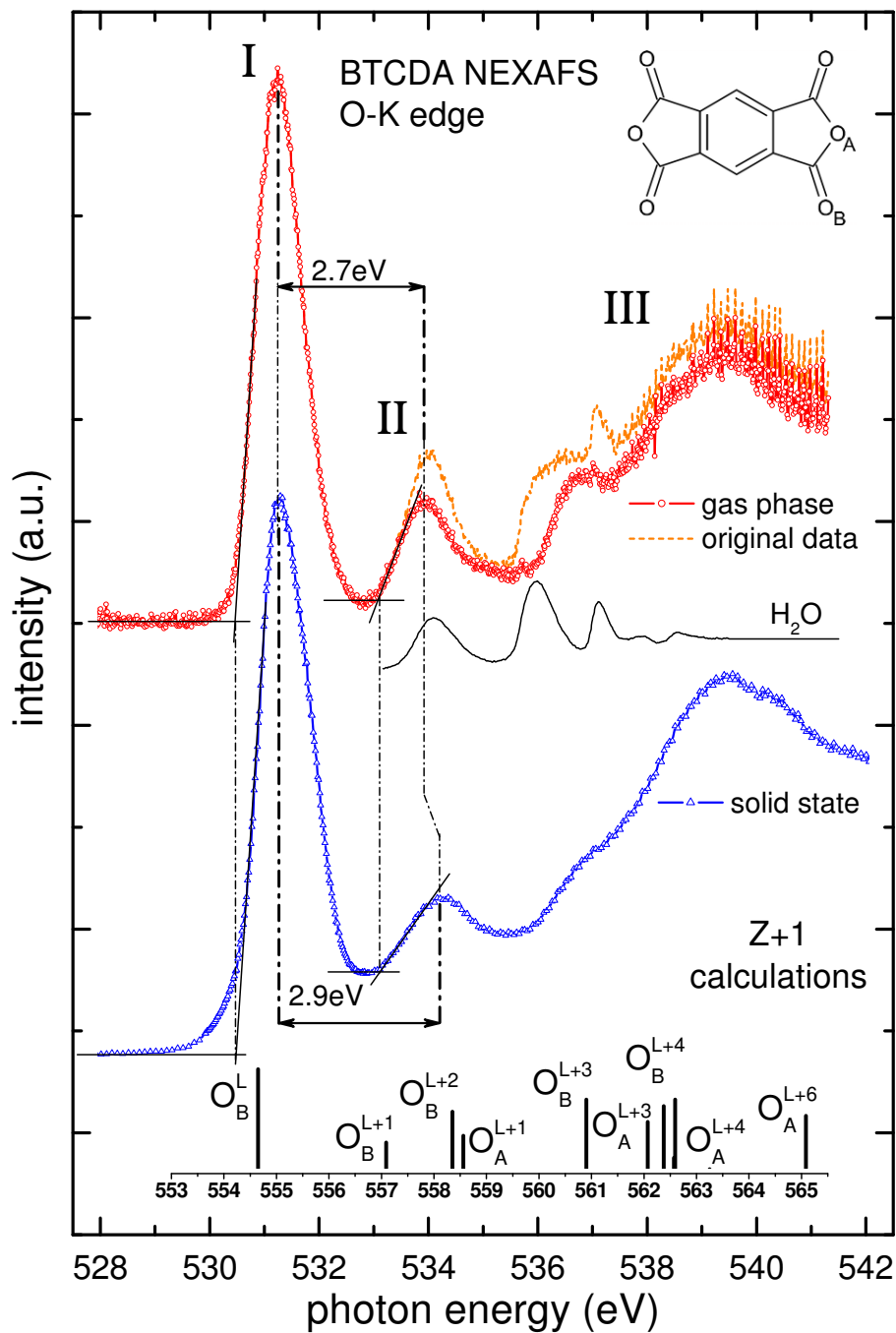
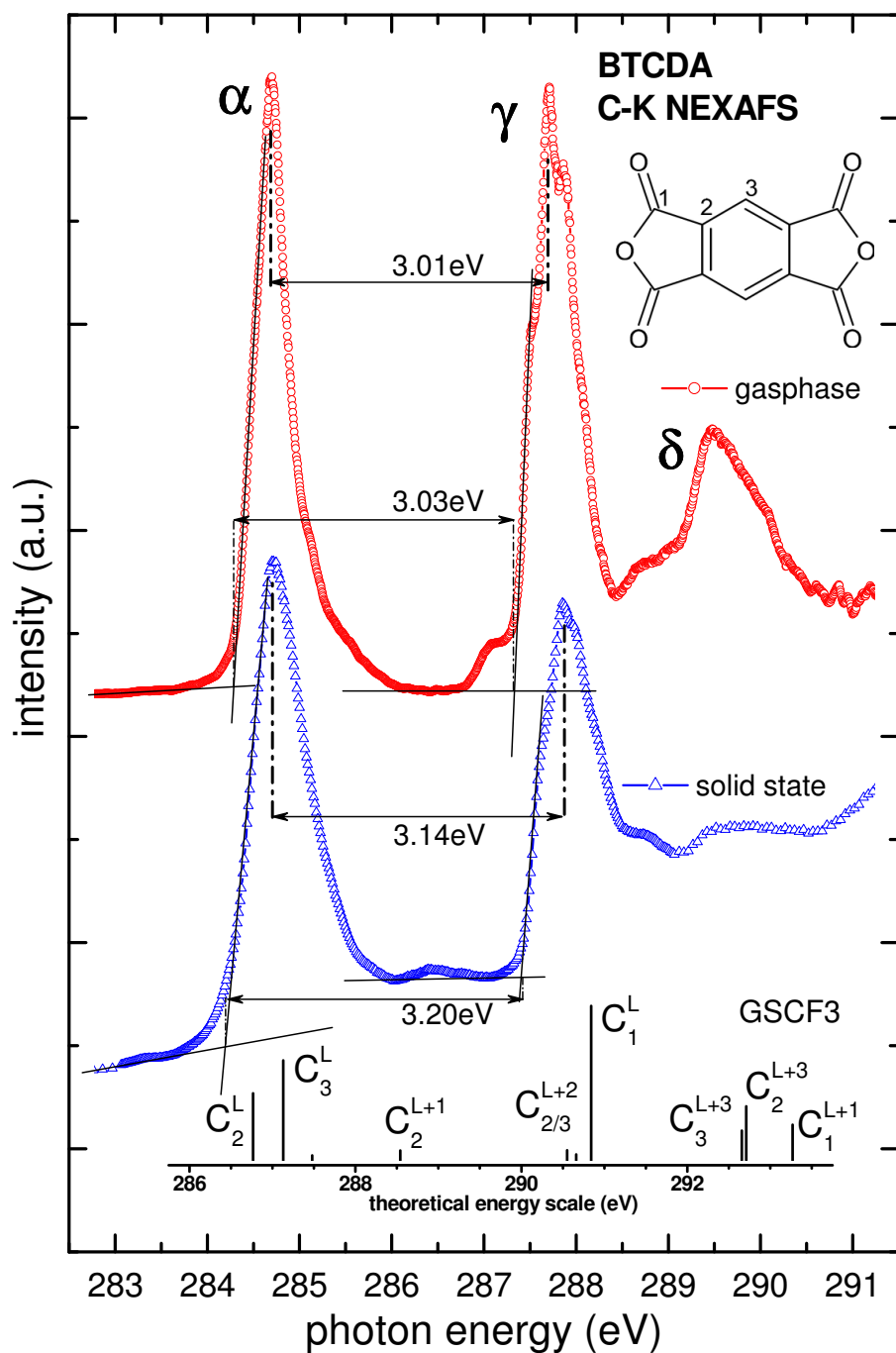*Figure 5.6:* BTCDA O–K edge NEXAFS spectrum in the gas phase (top), in the solid state (middle), and theoretical 'Z+1' calculations (bottom). Spurious contributions of H_2O have been subtracted from the gas phase spectrum using digitised data from reference [84]. The different scaling of the theoretical energy axis is explained in chapter 2.5.

of the O_B 1s→L+3 transition upon condensation, although the assignment is not unambiguous due to the absence of detailed features.

The main part of structure III is to a large extent identical to the solid state. This is astonishing all the more, since the O_A and the O_B LEMO+4 orbitals are widely extended and show a clear Rydberg character (see chapter C, page 117), whereupon they should be much more influenced by their surrounding.

5.2.2 BTCDA C–K edge

Figure 5.7 displays the C–K NEXAFS spectra of BTCDA in the gas phase (top), the solid state (middle), and theoretical calculations (bottom) using Kosugis GSCF3 code [44, 46]. Transitions originating from the C_2 and C_3 into the LEMO contribute to the first feature α, whereas the second feature γ^4 is essentially made up by a single electronic transition from the C_1 atom to the LEMO. Feature δ in contrast has contributions from all three carbon atoms.

At the low energy side of feature γ in the gas phase spectrum, a small shoulder is present. Although a CO π^* resonance (287.3 eV) could appear at this energy, the broad shape of the peak indicates a major contribution from the BTCDA molecule. In the solid state spectrum possibly the same peak is found in between features α and γ, red–shifted by about 0.5 eV. The assignment of these features is rather ambiguous since the very small transitions $C_{2,3}$ 1s→LEMO+2 and C_2 1s→LEMO+1 have to be considered. The extremely large shift of more than 0.5 eV of the $C_{2,3}$ 1s→LEMO+2 transitions upon condensation seems on the one hand very unlikely. On the other hand, without this shift, the very small C_2 1s→LEMO+1 transition has to provide the whole increased intensity in between features α and γ.

A very similar situation is found for NTCDA as described in chapter 5.3. In that case, the C_2 1s→LEMO+1 transition can been assigned to the more pronounced shoulder of the trailing edge of feature β. Consequently, the peak in between features α and β has been assigned to the shifted C_3 1s→LEMO+3 transition. Due to the close similarity of both molecules this explanation is adapted for BTCDA.

Also at the C–K edge, the *fixed mirror mode* of the monochromator causes a decrease of SNR in the gas phase spectrum above 289.5 eV even though not as dramatic as at the O–K edge. Nevertheless, special care has to be taken when interpreting these parts of the spectrum.

The overall appearance of the gas phase and the solid state spectra is not as similar as in case of the O–K edge. The solid state spectrum appears broadened[5], the FWHM of feature α (γ) increases by 60% (30%).

---

[4]For a consistent denotation, features with a main contribution from the carboxylic carbon are denoted as γ.

[5]The question whether this is caused by an increase of intrinsic line width or the vibrational coupling will be addressed in section 5.2.3.

Figure 5.7: BTCDA C–K edge NEXAFS spectrum in the gas phase (top) and the solid state (middle). The theoretical GSCF3 calculations (bottom) have a different energy scale (see chapter 2.5). Thelabels denote the transition from the respective carbon atoms (C_1 to C_3) into the LEMOs L to L+3.

For feature α the kinks in the trailing edge of the gas phase spectrum are not visible any more in the solid phase, but the asymmetry of the feature still persists. The fine structure of feature γ is very pronounced in the gas phase spectrum and still evident as distinct shoulders in the solid spectrum.

The peak intensities of features α and γ correspond well for both phases, whereas feature δ nearly vanishes completely upon condensation. One of the related orbitals, the C_3 LEMO+3 (see figure C.3), is wide spread (mixed Rydberg [5]) and is obviously quenched or shifted to higher energy upon condensation. The C_2 LEMO+3 in contrast is not as delocalised and still contributes to feature δ in the solid phase.

The region in between α and γ gains some intensity, although it seems unlikely that this intensity is supplied by the very small C_2 1s→LEMO+1 transition located right underneath. A similar situation is present at the trailing edge of feature γ. Here we find a significant redistribution of intensity of the feature δ towards lower energy upon condensation.

Therefore we can only evaluate the energy positions of the first two features. Upon condensation we find an increase of the energy splitting between feature α and γ of 170 and 130 meV for the onsets and the peak maxima, respectively.

At the C–K edge the well resolved fine structure in the gas phase and even the solid state spectrum is inviting to perform a more detailed analysis of the respective features. In order to better understand and quantify the first glance observations, we performed a Franck–Condon analysis as described previously in chapter 2.3.

5.2.3 FC fit analysis of BTCDA C–K edge

For BTCDA we also start the FC analysis with the spectrum of the single molecule in the gas phase, which comes closest to the ideal model of a non–interacting molecule. Based on the results of the GSCF3 calculations, two (one) electronic transitions will be used to build up the main part of feature α (γ) of the gas phase spectrum.

In a second step, we will then try to understand the changes that occur upon condensation by reproducing the solid state spectrum using the results of the gas phase analysis. Of course, different models for the transition from gas phase to solid state are possible and will be discussed in detail where applicable. All resulting fit parameters and plots of this FC analysis can be found in chapter B.3 on page 109.

Gas phase feature α

Feature α, especially the leading edge, seems to be built up by a single vibronic progression. On the other hand, the GSCF3 calculations yield two electronic transitions from the C_2 and C_3 1s into the LEMO. While the leading edge of the feature is reproduced very well with just one progression, the trailing edge in fact can only be described satisfyingly well with a second progression (GP09, see figure 5.8 top). The resulting residuum is in the range of 3%, and the overall agreement of

Table 5.2: Fit parameters of the FC analysis of BTCDA feature α based on the C_2 and C_3 1s→LEMO transition. Free parameters are set in italics. Intensity (int), shift (sh), scale (sc), and anharmonicity (ξ) are given in arbitrary units, the other parameters in eV.

FC fit label	pos	int	Γ_G	Γ_L	hν	sc	sh	ξ
				gas phase				
GP09	*284.52*	*1.332*	*0.160*	*0.112*	*0.192*	*0.447*	*2.694*	*0.030*
	285.03	*0.109*	*0.102*	0.112	*0.210*	*0.499*	*0.002*	*0.000*
			solid state from gas phase: broadened					
PEY03	*284.56*	*1.158*	*0.460*	0.112	0.192	0.447	2.694	0.030
	285.08	*0.094*	*0.471*	0.112	0.210	0.499	0.002	0.000

experimental data and fit is very good. Judging from the shape and the fast decay of this additional progression, the electronic transition does not necessarily need to couple to a vibration.

The resulting Lorentzian line width ($\Gamma_L = 110\,\text{meV}$) still is in a range that corresponds well to theoretical estimates ($\Gamma_L(C1s) \approx 0.1\,\text{eV}$) [85, 86] and former experimental results. This also applies to the Gaussian line width ($\Gamma_G = 160\,\text{meV}$).

Calculating the ground state vibration energy yields 0.21 eV for both progressions. A C=O or a C–C stretch vibration with 0.22 (1775) and 0.20 meV (1627 cm^{-1}) vibration energy [87], respectively, may be assigned.

In spite of a not very distinct fine structure in feature α, the FC–fit (GP09) convincingly describes the experimental data in accordance with the theoretical calculations.

Solid state feature α

Turning to the solid phase, we face a clearly broadened spectrum with even less structure that can not be fitted 'from scratch' convincingly. Applying the gas phase fit parameters is nevertheless feasible since the number of free parameters can then be limited to an absolute minimum.

Figure 5.8 (bottom) shows the simplest model of a mere broadening of the single peaks upon condensation. The exclusive increase of Gaussian line width with fixed intensity ratio and energy splitting of the two progressions already yields a reasonable result (PEY03) with a residuum of about 5%.

To further improve the agreement significantly, it is necessary to also vary the vibrational energy hν as well as the potential parameters *sh* and *sc* and also revoke the coupling of the energy positions. For this model of an adapted vibronic coupling
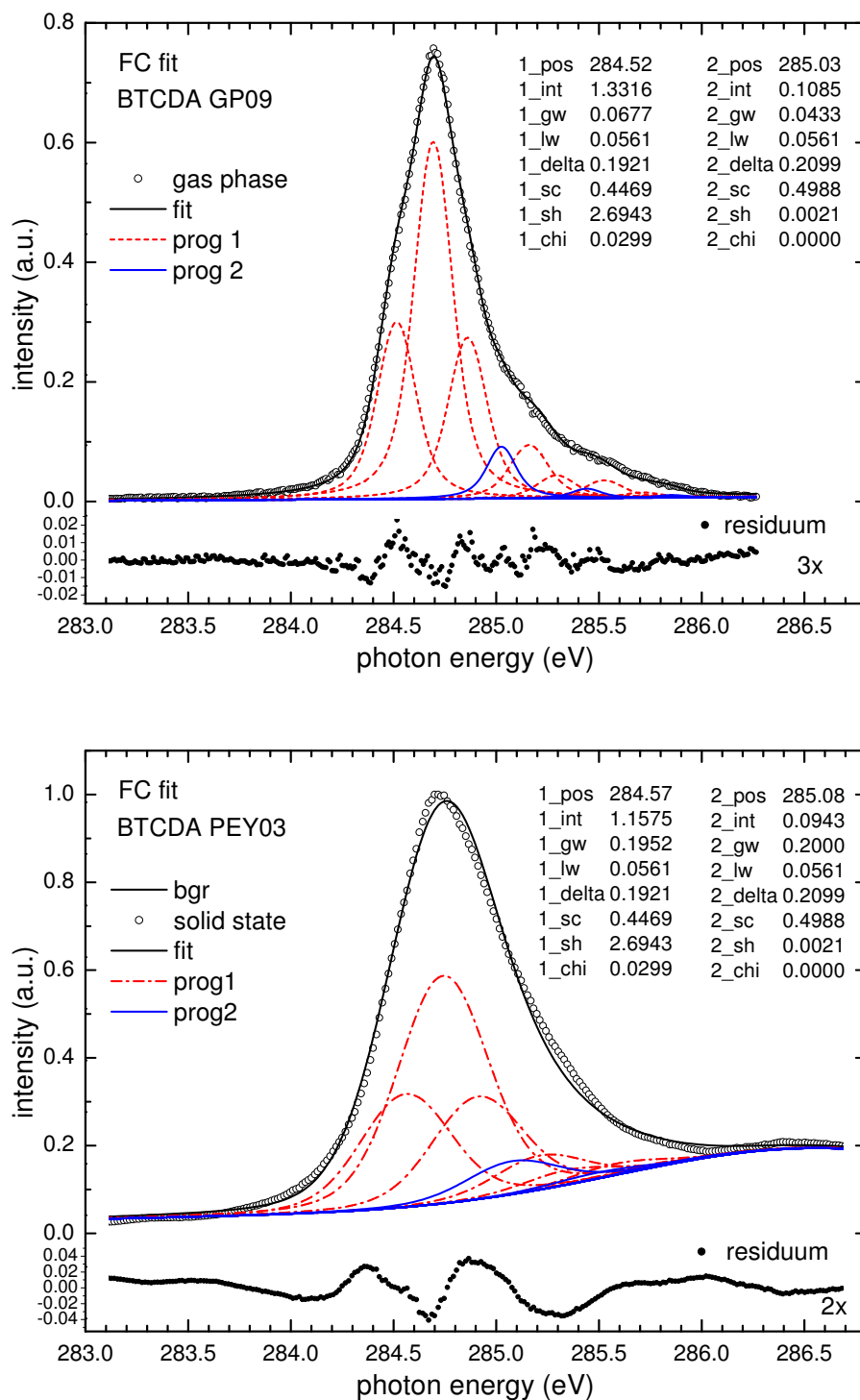
Figure 5.8: FC fit results for features α of BTCDA in the gas phase (top, GP09) and in the solid state (bottom, PEY03). Fit parameters see table 5.2.

(PEY04), the residuum decreases to about 2% at the cost of nearly doubling the number of free parameters.

Alternative approaches based on a splitting of the progressions due to solid state effects for example, are also conceivable and do not need as many free parameters. However, the approach using three components with fixed gas phase parameters turns out to completely fail to adequately reproduce the feet at the leading and trailing edge of the feature.

Comparing all possible scenarios, the first approach still impresses, apart from the small number of free parameters, by its simplicity and yet good agreement with the experimental solid state data. A further investigation of this feature regarding other models seemed not very promising due to the less distinct fine structure.

Gas phase feature γ

In contrast to feature α, feature γ of the gas phase spectrum provides much well resolved, detailed fine structure. In the region leading to feature δ, not as many details are present, also the data is not as reliable any more[6]. Therefore this part is accounted for by two single gaussian peaks representing all the non resolved progressions of the $C_{2,3}$ 1s→L+3 and C_1 1s→L+1 transitions.

In addition to the distinct fine structure, only one electronic transition is responsible for the whole feature. As a result of this unique combination, the FC analysis of feature γ is straightforward and yields a very good agreement (residuum in the 3% range) using one vibronic progression for the C_1 1s→LUMO transition (GP14). Solely the trailing edge is not reproduced as well as the leading edge of the feature.

The remaining alternating structure in the residuum, indicating a mismatch in line shape, can be eliminated by introducing an asymmetric gaussian line width. Unresolved low energy vibrations coupling to the electronic transition can broaden every single peak at the high energy side and cause this asymmetry [5].

Accounting for this effect, the resulting fit yields a perfect agreement with the experimental data, especially at the trailing edge (GP32). The potential parameters do not change due to this additional parameter except for the anharmonicity constant χ which decreases to zero. That means that the obvious asymmetry of the whole feature is rather caused by an asymmetric line shape than by unequally spaced vibrational peaks. The resulting Gaussian width of the high energy side is significantly larger (0.196 eV) compared to the width in the symmetric case, whereas the low energy side Gaussian width (0.142 eV) is comparable. All other parameters for this FC analysis are listed in table 5.3, and the fitted spectrum is displayed in figure 5.9.

Applying (the semi–empirical) equations 2.10 from section 2.3 we can calculate the vibrational energy. The resulting ground state vibration of 0.23(1) eV fits very

---

[6]This is due to the decrease of flux in this region.

Table 5.3: Fit parameters of the FC analysis of BTCDA feature γ based on the C_1 1s$\rightarrow$LEMO transition. Free parameters are set in italics. Intensity (int), shift (sh), scale (sc), and anharmonicity (ξ) are given in arbitrary units, the other parameters in eV.

FC fit label	pos	int	Γ_G	Γ_L	hν	sc	sh	ξ
				gas phase				
GP32	*287.52*	*2.402*	*0.142*[7]	0.065	*0.193*	*0.951*	*1.831*	0.000
			from scratch: equidistant components					
	287.63	*0.863*	*0.195*	0.065	*0.235*	*0.647*	*1.694*	*0.044*
PEY63	*287.82*	*0.297*	0.195	0.065	0.235	0.647	1.694	0.044
	288.01	*0.415*	0.195	0.065	0.235	0.647	1.694	0.044

well to two infrared (220 and 230 meV) and two raman active (222 and 232 meV) C=O stretching modes as assigned by infrared spectroscopy [87] and HREELS [88] measurements. This assignment is quite plausible since the electronic excitation of the C_1 atom will preferentially alter the potential surface in the ambit of the core hole and the excited electron.

Solid state feature γ

Feature γ of the solid state spectrum still provides enough structure to pursue the analysis of the gas phase data. There are two fundamental trends upon forming the solid state we have to distinguish:

1. A relatively weak interaction that does not affect the observed vibrations.

2. A totally different proximity of the molecules that alters the conditions for the vibrations and thereby the vibrations themselves.

The FC analysis of the solid state therefore has also two basic approaches:

1. Start with gas phase parameters, change as few parameters as possible to approach the solid state spectrum.

2. Start regular FC analysis 'from scratch'.

All figures to illustrate the different fit results are plotted in figure B.3 and the corresponding parameters are listed in table B.2. As a first step for approach 1., we performed a FC fit with a mere change of Gaussian line width, intensity, and energy position of the, apart from that, unchanged gas phase parameters (PEY24). The Gaussian line width increases by more than 25%, accounting for unresolved solid
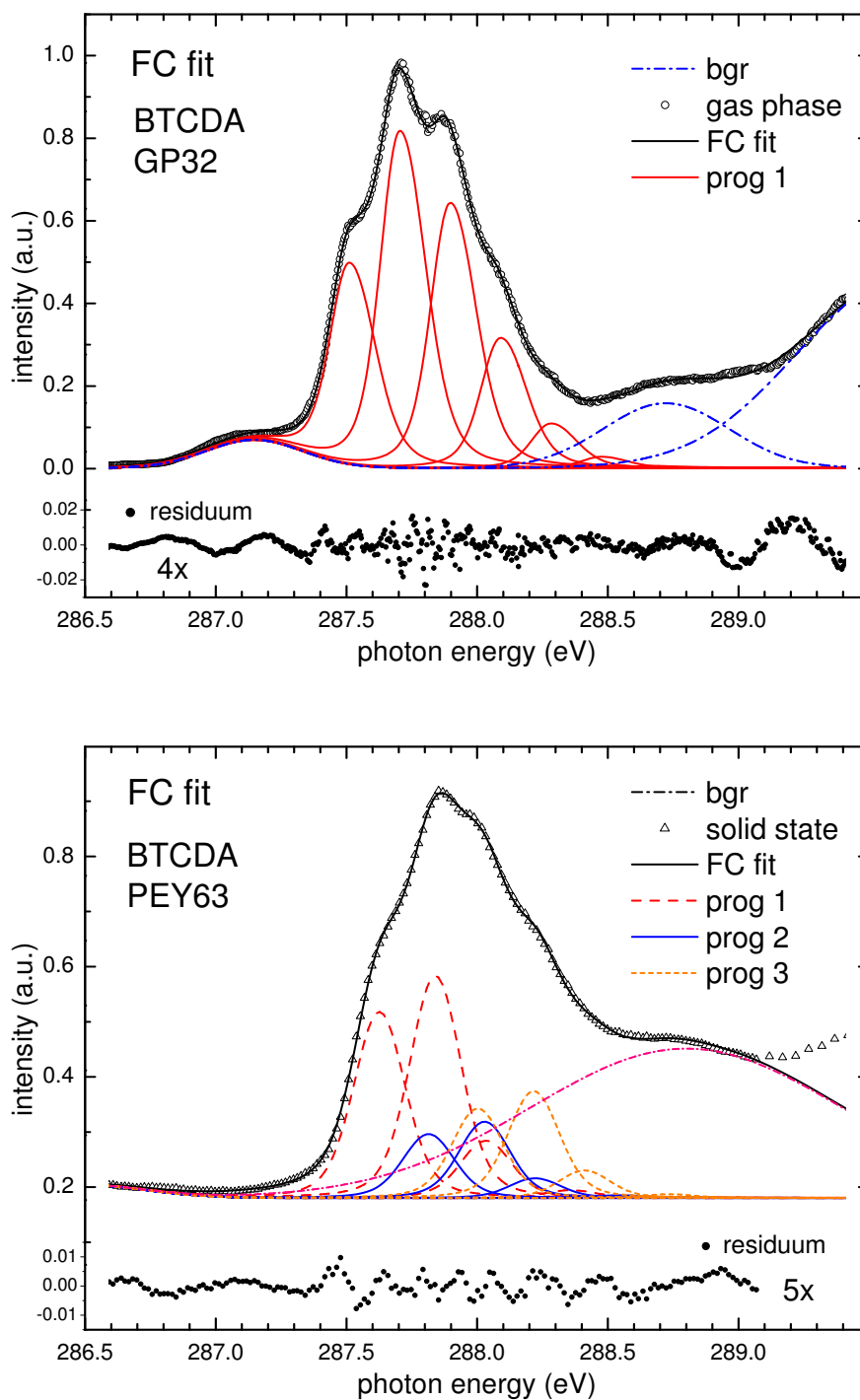
Figure 5.9: FC fit results for feature γ of BTCDA at the C–K edge. Top: gas phase spectrum fitted with an asymmetric line shape (GP32). Bottom: solid state spectrum fitted with 3 equally spaced components (PEY63). Fit parameters see table 5.3.

state effects. The resulting fit does not reproduce the leading edge well and the (double) peak is also not described convincingly. The single Gaussian peaks in the second part of the feature extend back to the leading edge but do not fit well to the shape of the spectrum at their actual energy position. These mismatches are also reflected in the large residuum in the range of 5%. This seems quite large though one has to consider that only 3 free parameters were used to perform the transition from gas phase to solid state. The asymmetric line shape, as introduced in case of the gas phase, does not improve the fit result, both components reach exactly the same value (PEY80). This is a clear hint that broadening effects other than in the gas phase occur in the solid state. Since the model of simple broadening, which has been successfully applied to other molecules (see chapter 5.3.3) fails for BTCDA, there have to be other mechanisms that influence the pristine spectrum.

In a second step several gas phase spectra with different intensities and energy positions were used to model the solid state spectrum. Each progression represents for example a different crystal phase, or Davydov component, and needs only two more parameters, namely intensity and energy position. Using two components (PEY21) does not yet improve the fit result significantly (residuum in the 4% range) compared to the mere increase of Gaussian line width (GP24). Not until a third component (PEY22), mainly contributing to the trailing edge, is added, the residuum will be reduced significantly (residuum in the 3% range). The single Gaussian peaks accounting for the background now contribute to the second part of feature γ in particular. Providing a fourth component (PEY23), however, does not improve the fit result any further, since the progression merges with the other components.

Although this approach provides a good overall agreement, the leading and trailing edges are not reproduced very nicely. Adding the Gaussian and Lorentzian line width as free parameter does, against expectations, not improve the fit strong enough to legitimate the additional parameters. As we will see, this model does not work as well as the following approaches in spite of a comparable number of free parameters.

Turning now to approach 2., we assume the solid state effects to completely alter the vibrational character of the gas phase spectrum, and start the FC fit of the solid state spectrum 'from scratch' with all potential parameters set free. This approach is not as easy to accomplish as for the gas phase since the existent fine structure is not as pronounced. Nevertheless, it is possible to reproduce the experimental data with one vibronic progression (PEY42). The resulting residuum is in the same range (3%) as in the gas phase, though the remaining wiggles indicate a major mismatch. Especially the fine structure at the trailing edge is not reproduced very well. For comparison, in case of the gas phase, the residuum might not be much smaller, but the present fine structure is at least accounted for by the FC analysis. As before, an asymmetric line shape does not improve the fit result for the solid state at all (PEY81).

Another drawback is the vibrational energy of 220 meV which corresponds to a ground state energy of 290 meV. In this energy range only two normal modes (combined stretching vibrations) with an energy of 256 meV ($2063\,\mathrm{cm^{-1}}$) and 360 meV ($2902\,\mathrm{cm^{-1}}$) are observed in the infrared spectrum [87, 88]. In the light of the good agreement for the C=O stretch vibration in case of the gas phase, the discrepancy is rather high for the solid state.

Since also this approach is not completely satisfying, one needs to look for other models leading to a better agreement with the experimental data. One possible cause for the mismatch at the trailing edge, which is present in all hitherto used approaches, are contributions of higher energy electronic transitions. It is quite conceivable that the C_2 or C_3 1s→L+3 transition is shifted towards lower energy by solid state effects. Unfortunately, neither in the gas phase, nor in the solid state spectrum any fine structure is present which would allow a convincing FC analysis to support this theory.

If we now exclude other electronic transition in this energy region, only two models for the effect of condensation are reasonable:

A) A (Davydov) splitting of the original progression into several identical components caused by intermolecular interaction or different crystal phases.

B) An additional vibration coupling to the same electronic transition.

Both approaches have been tested and all results are listed in table B.2 and figure B.3.

When splitting the electronic transition into several components it turns out that the individual progressions are equally spaced. That reduces the additional parameters to only one per additional progression. A significant improvement in shape and amplitude of the residuum is not reached until the third component is added (PEY63, figure 5.9 and table 5.3). Then the residuum is relatively flat and the amplitude is halved compared to using just one progression. The vibrational energy of 235 meV corresponds to a ground state vibration of 260 meV which just fits to a combined infrared vibration of 256 meV ($2063\,\mathrm{cm^{-1}}$).

Approach B), using an additional vibration coupling to the same electronic transition yields a residuum (PEY45) which is in amplitude and shape comparable to the before discussed 3–component fit. However, due to the independent vibration, three more parameters are needed in this case. The resulting vibration energies are 320 and 210 meV. The respective ground state energies of 430 and 250 meV correspond to combined stretching modes with 455 meV ($3669\,\mathrm{cm^{-1}}$) and 256 meV ($2063\,\mathrm{cm^{-1}}$) respectively.

Conclusion of the FC analysis of feature γ

In spite of the very well resolved fine structure even in the solid state spectrum of BTCDA, the FC analysis can not yield a unambiguous picture of the mechanisms that alter the NEXAFS spectrum upon condensation.

In view of a minimum of fitting parameters, the model of a mere gaussian broadening of the gas phase spectrum reproduces the solid state spectrum well. But even with several gas phase components, the leading and trailing edge cannot be reproduced exactly.

Measured by the fit quality of the gas phase spectrum, only the models of split components and additional vibration are acceptable.

However, neither by the fit quality nor by the possible assignment of the ground state vibrations can be determined which approach is more realistic.

5.2.4 Summary of BTCDA results

Summing up the main results of comparing gas phase and solid state NEXAFS spectra of BTCDA, we find changes at the O–K as well as the C–K edge. All differences at the O–K edge can be assigned to a mere change in intensity of the O_B 1s→LEMO+2, O_A 1s→LEMO+1, and O_B 1s→LEMO+3 transitions. An inspection of the respective excited molecular orbitals in figure C.2 however, yields no indication for the cause of these changes. At the C–K edge, relative red–shifts of 0.13 to 0.17 eV has been observed.

In the FC analysis of the C–K gas phase spectrum it has been shown that feature γ is built up by a C=O stretching vibration coupling to the C_1 1s→LEMO transition featuring an asymmetric Gaussian line shape.

The solid state spectrum, in contrast, cannot be understood as a mere broadened, shifted or splitted gas phase spectrum. Comparing different models in the FC analysis, we conclude that the vibrational parameters are certainly altered upon condensation. Beyond that an additional vibration coupling to the electronic transition or several equally spaced components of the same vibration are possible.
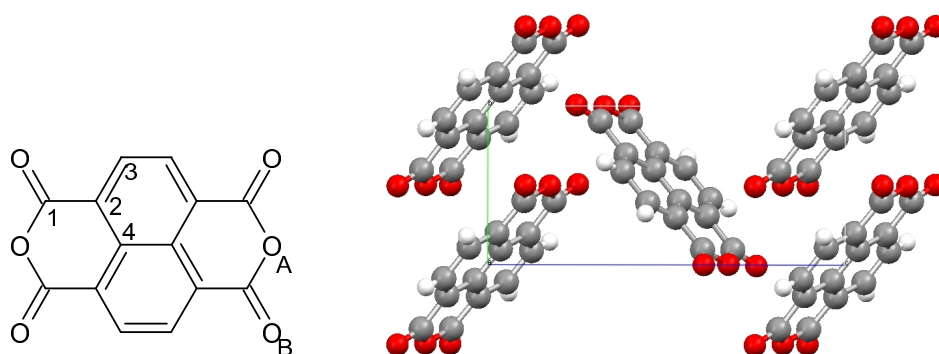
Figure 5.10: Structural formula (left) and crystal structure (right, view along a–axis) of NTCDA [89, 90].

5.3 NTCDA

The aromatic molecule NTCDA (structural formula see figure 5.10) consists of a naphthalene core with four carboxylic acid and two anhydride groups at each side. In contrast to the smaller BTCDA, the functional groups also form a 6–ring structure. Given the D_{2h} symmetry of the free molecule, we find four chemically different carbon atoms (C_1 to C_4) and two chemically different oxygen atoms O_A and O_B.

NTCDA crystallises in a monoclinic crystal structure with two molecules per unit cell and is assigned to the $P2_1/n$ space group. The basis vectors are $a = 7.867\text{Å}$, $b = 5.305\text{Å}$, and $c = 12.574\text{Å}$ with an angle of $72.73°$ between the a– and c–axis [89, 91]. The molecules stack along the b–axis with an interplanar distance of 3.5Å which is slightly smaller than the sum of the oxygen or carbon van–der–Waals radii [83]. The molecules form a herringbone structure with the short sides facing the neighbouring molecular planes.

The gas phase data presented in this work have been measured at BESSY II at a gas cell temperature of $\approx 500\text{K}$. Energy calibration has been performed using former results (ELETTRA) calibrated to CO_2 π^* resonances. The solid state data have also been measured at BESSY II and stem from a multilayer film (30 monolayers ML), prepared on a cold (160K) Ag(111) substrate (cold multilayer (CML)). This film has then been annealed to 260K (annealed multilayer (AML)). The CML film is known to have a relatively high degree of stress and low structural order with preferentially flat lying molecular orientation. Annealing yields a microcrystalline film with an average molecular tilt angle of $54°$ with respect to the substrate [92].

5.3.1 NTCDA O–K edge

Figure 5.11 presents the O–K NEXAFS data of gaseous (top) and condensed (middle) NTCDA. In case of the condensed phase, spectra recorded with s– and p–polarisation (from reference [93]) have been averaged to avoid dichroic effects from oriented molecular growth. All experimental NEXAFS features can be assigned to electronic transitions using GSCF3 calculations [93], which are plotted at the bottom of figure 5.11. The dominant transitions are denominated with respect to their initial (O_A, O_B 1s) and final states (LEMO L to L+4). While feature I and II are both built up by just one electronic transition, feature III has two contributions from the O_A 1s→LEMO+1 and O_B 1s→LEMO+3 transition.

The overall signature of the gas and solid phase spectra is very similar, and no additional fine structures can be resolved in either case. Upon condensation only the FWHM of features III increases significantly by ca. 20%, the width of the other features stays constant within the error bar. Within the accuracy of calibration the first two features align and no effect of intermolecular interaction can be identified.
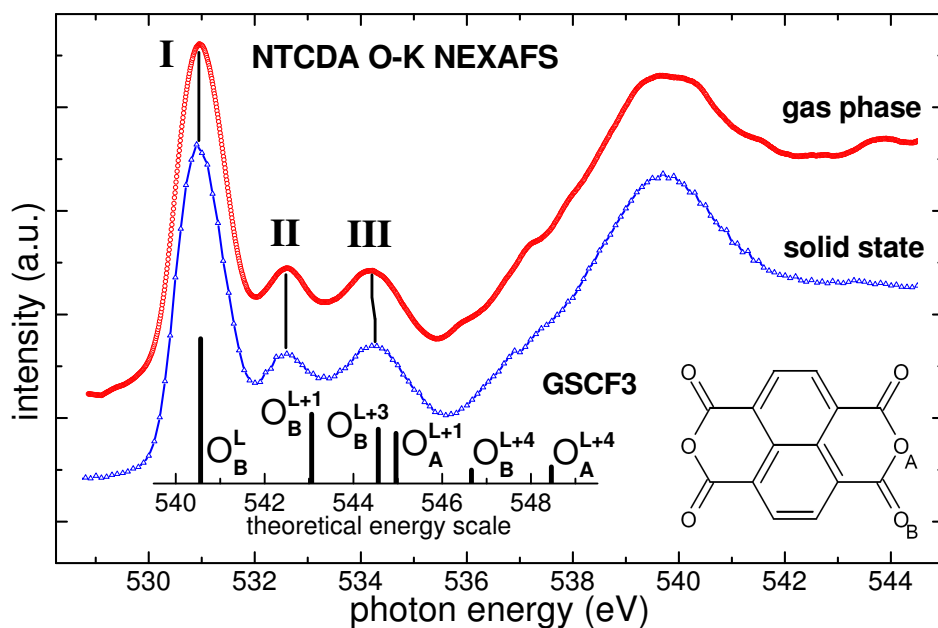
Figure 5.11: NTCDA O–K NEXAFS spectra of gas- (top) and condensed phase
(middle, average of s- and p–polarisation), and GSCF3 calculations (bottom) [93].
The labels denote the transitions from the respective O 1s sites O_A and O_B into
the LEMOs L to L4.

Gas phase feature III shows a very small energy shift ($< 70\,$meV) that can
be explained by a change in the intensity ratio of the two subjacent transitions
(O_B 1s$\rightarrow$L+3 and O_A 1s$\rightarrow$L+1). Given the very similar changes in case of BTCDA
(see figure 5.6), where the shift is a little bit more pronounced, this interpretation
is quite plausible. Interestingly, for both molecules the O_A LEMO+1 orbital is
involved in this feature.

Upon very close inspection, various small wiggles are observed in the very smooth
gas phase spectrum. These structures could arise from different contaminations of
CO ($534\,$eV), CO_2 ($535\,$eV), and H_2O (534, 536, and $537\,$eV). However, compared to
the contaminations in BTCDA (H_2O) and PTCDA (CO, CO_2), these contributions
are very small and will not alter the spectrum significantly.

5.3.2 NTCDA C–K edge

Figure 5.12 shows the C–K NEXAFS spectra of NTCDA in the gas phase (spec-
trum (1)), in comparison with the data recorded for the CML (spectrum (2)), and
the AML (spectrum (3)). The corresponding GSCF3 calculations are plotted at the
bottom [93].

According to theoretical calculations, features α and β can be assigned to C
1s$\rightarrow$LEMO and LEMO+1 transitions originating from the ring carbon atoms C_2, C_3,
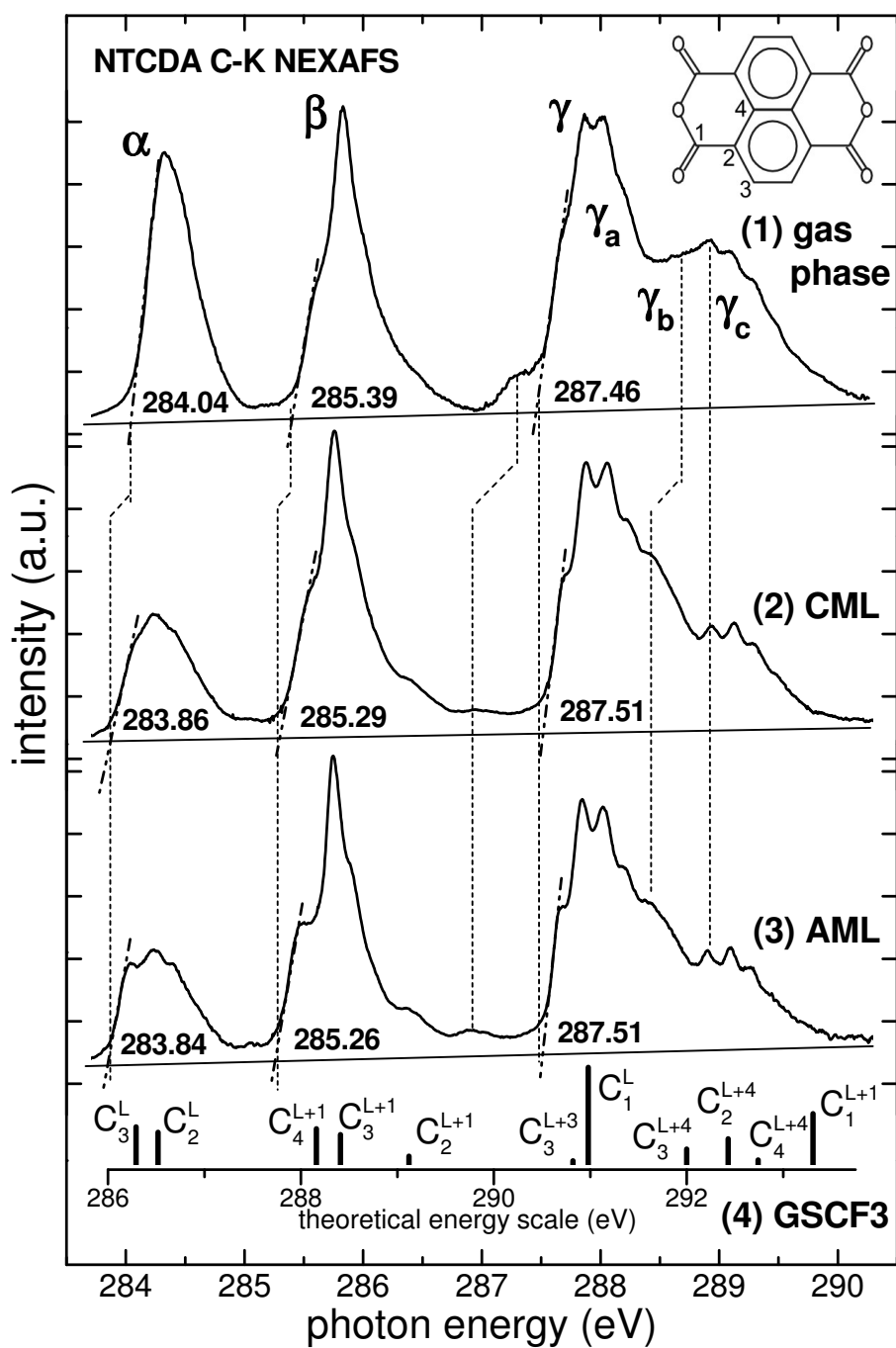
Figure 5.12: NTCDA C–K NEXAFS of the gas phase (1), the condensed cold multilayer (2), after annealing (3), and GSCF3 calculations (4) [93]. The chemically nonequivalent C 1s sites (C_1 to C_4) are denominated in the inset.

and C_4. Feature γ is dominated by C_1 1s→LEMO and LEMO+1 transitions at the anhydride carbon, but it also contains a smaller contribution from a C_2 1s→LEMO+4 transition. The GSCF3 and the WAVELS calculations (see chapter 2.5) yield an additional contribution of the C_3 1s→LEMO+4 transition. Interestingly, neither the CML nor the AML show any sign of polarisation dependence in this energy region. As depicted in table C.1, the respective orbital has a clear Rydberg character and is widely extended, especially in the x–y plane. Thus this transition might be quenched or shifted to higher energies in the solid state spectra. This issue will also be addressed in the FC analysis in the following section.

Not all features in the spectrum can be explained solely by electronic transitions. The rich fine structure is due to the coupling to vibrational modes, each leading to a progression of (vibrational) peaks for each electronic transition [93]. The positions of the peak maxima therefore also depend on the shape of the respective vibronic progression (represented by the Franck–Condon factors). Consequently, the peak onsets, which are associated with the energy of the adiabatic transitions, are used as a reference in the following.

Although the experimental spectra are similar at first glance, subtle differences in all three main features are evident upon closer inspection. As can be clearly observed, e.g., for the vibronic fine structure in feature γ, the gas phase data are broadened (see also curve fit analysis and fit results in table B.4). Since we can exclude experimental broadening effects (see chapter 3.2.2), we assign the increased line width to a thermal excitation of low–energy vibrational modes (<40 meV) in the initial state which occurs due to the high temperature in the gas cell. Density functional theory (DFT) calculations [94] yield three out–of–plane folding and two in–plane deformation modes of the anhydride group, which fit to the temperature range of about 500K (gas cell temperature). A similar broadening effect has also been observed in the gas phase spectra of C_{60} [32].

As reported earlier [92] the higher order of the annealed film leads to a reduction of inhomogeneous broadening and hence to better resolved fine structure. The three main features of both solid state spectra have the same energy positions, although measured at different temperatures. Feature γ of the gas phase spectrum obviously also aligns well with the solid state spectra within the accuracy of energy calibration (± 50 meV). For features α and β, however, *relative* shifts of both, the peak maxima and the peak onset positions occur. In the CML (AML) spectra the onsets of features α and β are shifted by 0.23 eV (0.25 eV) and 0.15 eV (0.18 eV), respectively, towards lower energy compared to the gas phase data.

Feature γ contains overlapping contributions of mainly three transitions, two of which are derived from the functional groups (γ_a and γ_c in figure 5.12) and one from the naphthalene core (γ_b).

Note that upon condensation, a redistribution of intensity in the centre of this feature is evident which possibly is caused by a shift of the γ_b peak to lower energy. Such a shift would be in accordance with the shifts of the other transitions α and β

located at the naphthalene core. Together with alternative interpretations this will be examined in detail in section 5.3.3.

In passing we note that the small peak at the leading edge of feature γ at 287.3 eV in the gas phase spectrum shifts to 286.9 eV in the AML spectrum. However, this peak most probably has some contribution from the C 1s→π^*–transition of spurious CO in the case of the gas phase spectrum and thus complicates an exact determination of its energy position. Without doubt, the main contribution is from the C_3 1s→L+3 transition since the CO resonance is much sharper.

Apart from the overall red shift of the features associated with the ring system, the intermolecular interaction leads to additional changes concerning the line shape and relative intensities. Although the difficult normalisation of the gas phase spectrum complicates a quantitative analysis, the intensity decrease of feature α is significant. Moreover, the shape of this feature is completely altered. In the gas phase spectrum feature α appears as one single (though asymmetric) peak with a relatively small FWHM of 0.44 eV. In the solid state this peak is split up and shows two shoulders on both sides of the maximum for the CML data, which become clearly resolved in the AML spectrum. At the same time, the width of feature α is increased to 0.64 eV. These severe changes of the shape of the feature can be attributed to a shift of one of the subjacent transitions, producing the shoulder at the leading edge and revealing the, possibly altered, vibrational fine structure of the remaining transition.

Similar observations can be made for features β and γ, where in particular the shoulders on the low energy side become more pronounced for the CML and appear as well–resolved peaks in the AML data. Interestingly, these effects are getting less distinct from feature α to γ.

The general blurring of fine structure in the gas phase can be understood on the one hand by the absence of splitting effects (e.g. Davydov Splitting) that produces the distinct shoulders of the features in the solid state. This is a strong support of earlier interpretation since the solid state NEXAFS data could only be described well by considering a *Davydov Splitting* in the order of 100 meV for all resonances [92]. On the other hand, thermal broadening will smooth out the remaining fine structure even further in the gas phase.

5.3.3 FC fit analysis of NTCDA C–K edge

In order to find an appropriate model to describe the changes in structure γ, we performed a Franck–Condon (FC) peak fit analysis as explained in detail in chapter 2.2. In a first approach only three electronic transitions were used to build up the structure since any fourth component would vanish during the iterations or merge with another progression.

The fit result for the gas phase spectrum (GP09) is displayed in figure B.2 (top), the respective fit parameters are summarised in table B.4. Theoretical and experimental curves match very well, the remaining periodic structures in the residuum (2%

range) are very likely due to the neglect of contributions from additional unresolved vibrations. The Lorentzian line width (Γ_L) of 78 meV is consistent with former results [95, 96] and theoretical data [86] for the C 1s core hole life time. Strikingly, the vibrational energy (hν) and the potential parameters (sc, sh) are very similar for γ_a and γ_c, whereas γ_b differs significantly. Obviously both transitions at the C_1 carbon atoms (into LEMO+1 and LEMO+4) couple to the same C=O vibrational stretching mode with a vibrational energy in the ground state of 230 meV as formerly shown for the solid state data [92]. Calculating the vibrational ground state energy for γ_b yields a comparable value, but given the less distinct fine structure in this region, the assignment is not as convincing (see also chapter 5.6).

In order to even better understand the changes upon condensation, the solid state data (CML and AML) were also fitted. In the following, different approaches for an implementation of the transition to the solid state will be introduced. Starting with a fit procedure where the two spectra are fitted consecutively, a more sophisticated method with a simultaneous fit procedure will be presented.

Sequential fit: shift of γ_b

As a first approach, the initial fit parameters derived from the gas phase analysis (GP09) were used as starting point for the sold state spectra. Subsequently, as few parameters as possible were varied in order to identify those parameters that are responsible for the spectral changes between gas phase and CML/AML spectra. In a first step only a variation of background, transition intensities, and Gaussian line width (Γ_G) was allowed[8]. The respective curve fits provide a satisfying result only for the leading and trailing edge of the entire feature γ, especially if the small number of used free parameters is considered.

For a clearly better (46%) χ^2 value it was sufficient to only add the energy position of the γ_b transition as fit parameter. This leads to a shift of the adiabatic transition relative to the C_1 1s→L transition of 0.19 eV (0.14 eV) for the CML (AML) data. In figure B.2 the respective curve fits for the gas phase (GP09, top) and AML (AML203, bottom) spectra are displayed. The fit parameters for all three phases are summarised in table B.4. All characteristic features of the condensed phases are reproduced satisfyingly well considering the above mentioned constraints and the neglect of solid state effects, such as, e.g., a *Davydov Splitting* [92]. Using this model, the transition from gas to solid phase is performed by solely changing six parameters (2x pos, 3x int, Γ_G).

Please note that, of course, other sets of fit parameters are also feasible, but only at the expense of more fit parameters and no significantly improved (41%) χ^2.

---

[8]The χ^2 value of this approach provides the basis for the *relative* χ^2 values of the following fit models.

The important result of this first peak fit analysis of feature γ is an energy shift of feature γ_b, which is in the order of $0.2\,\text{eV}$ and hence equal to those of the other transitions located at the naphthalene ring system.

Simultaneous fit: shift of γ_b

In the first approach, the solid state data is clearly under represented since the actual fit is just performed for the gas phase spectrum. To better account for the structure of the solid state spectrum, a *simultaneous* adjustment of the theoretical spectra to the gas phase and the solid state data is needed. Thereupon, parameters can be coupled within one data set and even between the theoretical curves for gas phase and solid phase data. Only this procedure ensures an equal treatment of both phases, provided an identical number of points and point density for both sets of data.

The result of reproducing the previous model is shown in figure 5.13 (AML13). The new fit convinces with a clearly better fitted trailing edge of the solid state spectrum without loosing fit quality in the gas phase spectrum (GP13). The parameters differing for gas and solid phase are the same previously used for the transition from one phase to the other. The resulting shift of feature γ_b of $120\,\text{meV}$ is comparable to the former result ($140\,\text{meV}$).

Simultaneous fit: quenching of *mixed Rydberg–state*

Using this fitting technique, it is now also possible to use a model applying *four* progressions in case of the gas phase and thereby accounting for the Rydberg–like C_3 1s$\rightarrow$L+4 transition. To clarify the expression, talking about the Rydberg–like transition means a single electronic transition to a Rydberg–like state that couples to a vibronic progression rather than a whole Rydberg *series* [97–100]. The latter of course would be very different in shape and hence cannot be described by a Franck–Condon profile.

In this model, the relative spacing of all transitions is coupled for both phases and the vibrational parameters are identical for the corresponding progressions in each phase. In spite of the seven transitions (for both spectra), the number of free parameters (27) is still acceptable. The agreement of theoretical and experimental data, shown in figure 5.14, is in general as good as for the 'shift–model'. In the region from $288.4\,\text{eV}$ to $289.2\,\text{eV}$ of the gas phase spectrum (GP10), the accordance is even better, albeit somewhat more wiggly, than in the previous model. Apart from the energy position of γ_b in the solid state spectrum (AML10), the same parameters (pos, 3(4)x int, Γ_G) change from gas– to the solid phase.
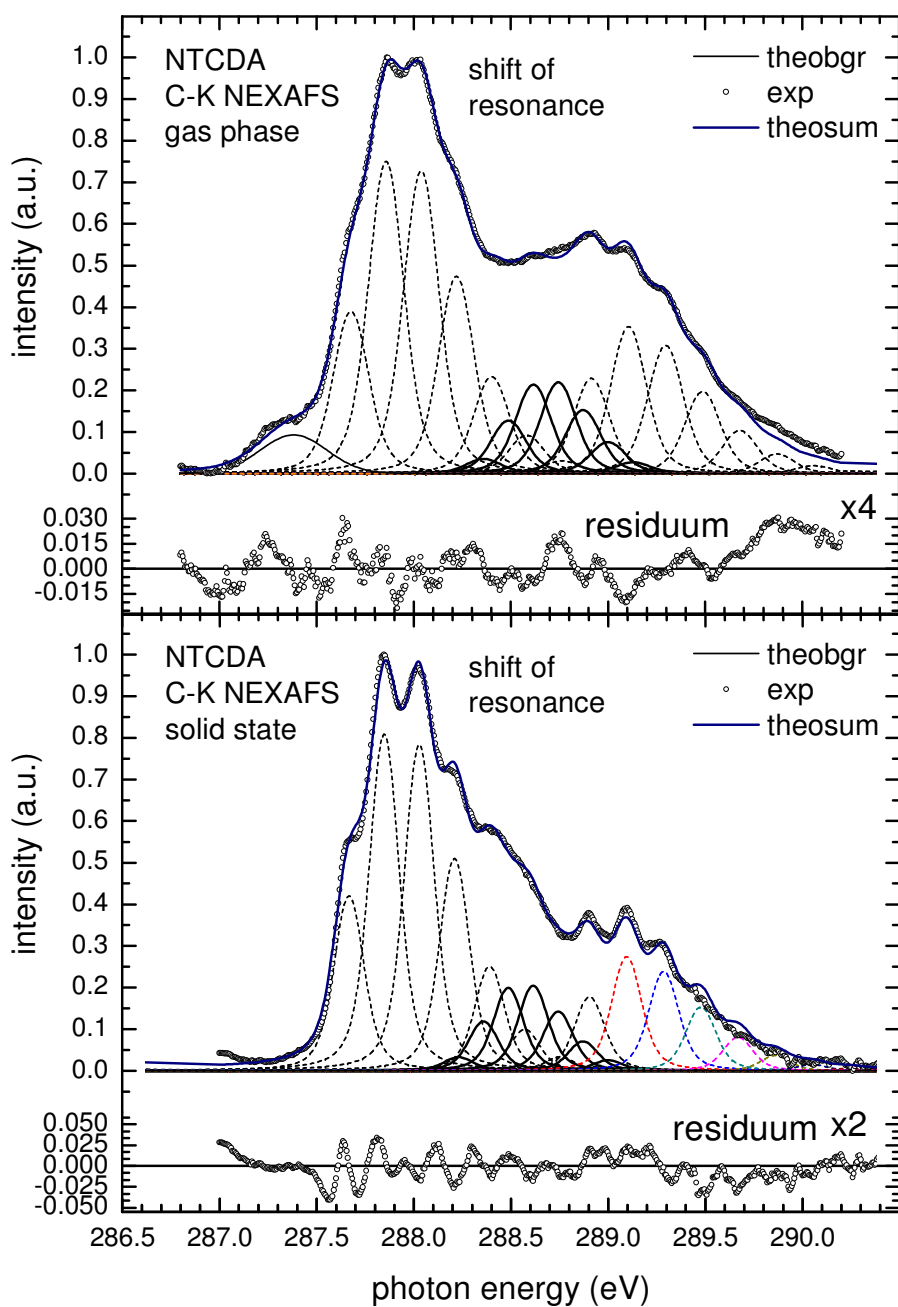
Figure 5.13: Simultaneous FC fit using a shift of one progression to model the transition from gas phase to solid state. Fit parameters are listed in table B.4 (GP13, AML13).
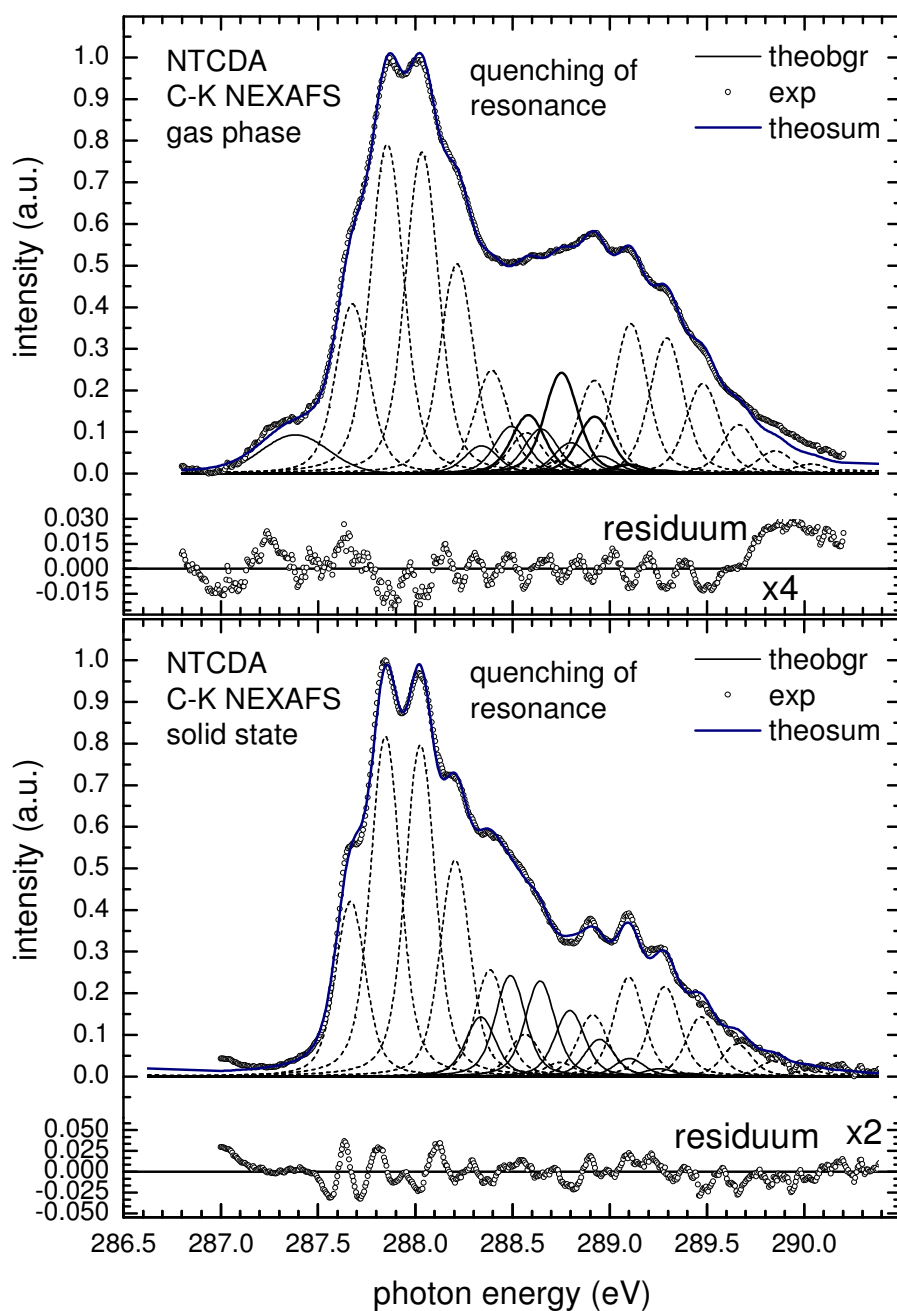
Figure 5.14: Simultaneous FC fit using a quenching of one progression to model the transition from gas phase to solid state. Fit parameters are listed in table B.4 (GP10, AML10) of gas phase and solid state spectra.

Approaching the *leading edge*

None of the two FC fits presented above does convincingly reproduce the distinct leading edge of the solid state AML spectrum. As described in reference [93], only a splitting of each progression into two, in that case *Davydov* components yields a satisfying result for this pronounced shoulder. Figure 5.15 (AML08, top) presents such a fit with a constant splitting of $85\,\mathrm{meV}$ of the respective progressions.

Encouraged by the good results for the gas phase spectrum of BTCDA (see chapter 5.2.3), a FC fit with an asymmetric line shape was performed for the NTCDA AML spectrum. Since only the leading edge, i.e. γ_a, is of special interest in this case, the standard line shape and completely free parameters were used for the other progressions $\gamma_{b,c}$. As displayed in figure 5.15 (AML02, bottom) this model can be applied very successfully and the result is comparable with the approach using splitted progressions. The ratio of the two Gaussian widths is 2.2 and thereby much larger compared to 1.4 in case of the BTCDA gas phase. All parameters for both spectra are listed in table B.4.

Compared to the standard fit procedure, one additional parameter (Γ'_G) is needed for the model of the asymmetric line shape, and two (energy splitting ΔE_{DS}, intensity) in case of the splitted progression. Thus, the asymmetric line shape accounting for, i.e., unresolved vibrational coupling to the excited state has to be considered as an equally suited model to explain the pronounced shoulder of the NTCDA AML spectrum.

Summary of FC analysis

In summary, we find that for NTCDA, in contrast to BTCDA, it is possible to reproduce the solid state data with the parameters of the gas phase spectrum quite well. Different FC fit procedures consistently yield hard evidence that the C=O vibration coupling to the C_1 transitions is not altered upon condensation, apart from a general increase in line width.

For the transitions contributing to the central part of feature γ in contrast, no definite model could be found. The most self–evident approaches, a shift of feature γ_b and a quenching of the Rydberg–like transition, are both equally suited to reproduce the solid state spectrum with the same number of free parameters. Hence it is not possible to reveal the mechanism causing the redistribution of intensity in feature γ upon condensation in full detail.

For the NTCDA AML spectrum a new model was introduced to account for the very distinct shoulder at the leading edge of feature γ. The results show that also unresolved vibrations causing an asymmetric line shape have to be considered as an alternative explanation to the hitherto used model of splitted progressions due to solid state interactions.

5.3.4 Summary of NTCDA results

In summary, we have presented a consistent analysis of high–resolution NEXAFS data of NTCDA in both, gas and solid phase. When comparing these phases we find significant changes in the energy position, intensity, and fine structure of some π^*–resonances in the C–K NEXAFS spectra.

Most important, all features associated with the aromatic ring system show a red shift of about $0.2\,\mathrm{eV}$ whereas transitions located at the anhydride group show no energy shift and no major changes in line shape. Moreover, no changes in the O–K NEXAFS or of the signature of the C=O vibrations are distinguishable.

This shows that only the electronic levels of the aromatic ring system of the naphthalene core are significantly affected by solid state formation.

Apart from this local information, the size of the shift ($0.2\,\mathrm{eV}$) and the change of the shape of the naphthalene features are surprisingly large. We note that the NEXAFS process leads to a neutral final state and hence intermolecular polarisation or charge transfer screening effects do not play a role (in contrast to, e.g., photoemission). This is consistent with the finding that molecules like CO and O_2 chemisorbed on metals, which are chemically very different compared to the gas phase, show shifts of the same order [27, 101].

Considering these results, we must conclude that the observed changes in the spectra represent the intermolecular π–π–interaction between the aromatic (naphthalene) cores and that this interaction is much stronger than mere dispersive (van–der–Waals) interaction. Indeed, to our knowledge no such NEXAFS shifts are observed for van–der–Waals interacting condensates [63].

In this context, an appropriate model of the intermolecular interaction is an enhanced delocalisation of the aromatic π–system, whereupon the unoccupied orbitals are lowered in energy in the condensate, and appear at lower energy in the NEXAFS spectra. Further, more comprehensive interpretations will be given in the discussion for all dianhydrides in chapter 5.5.
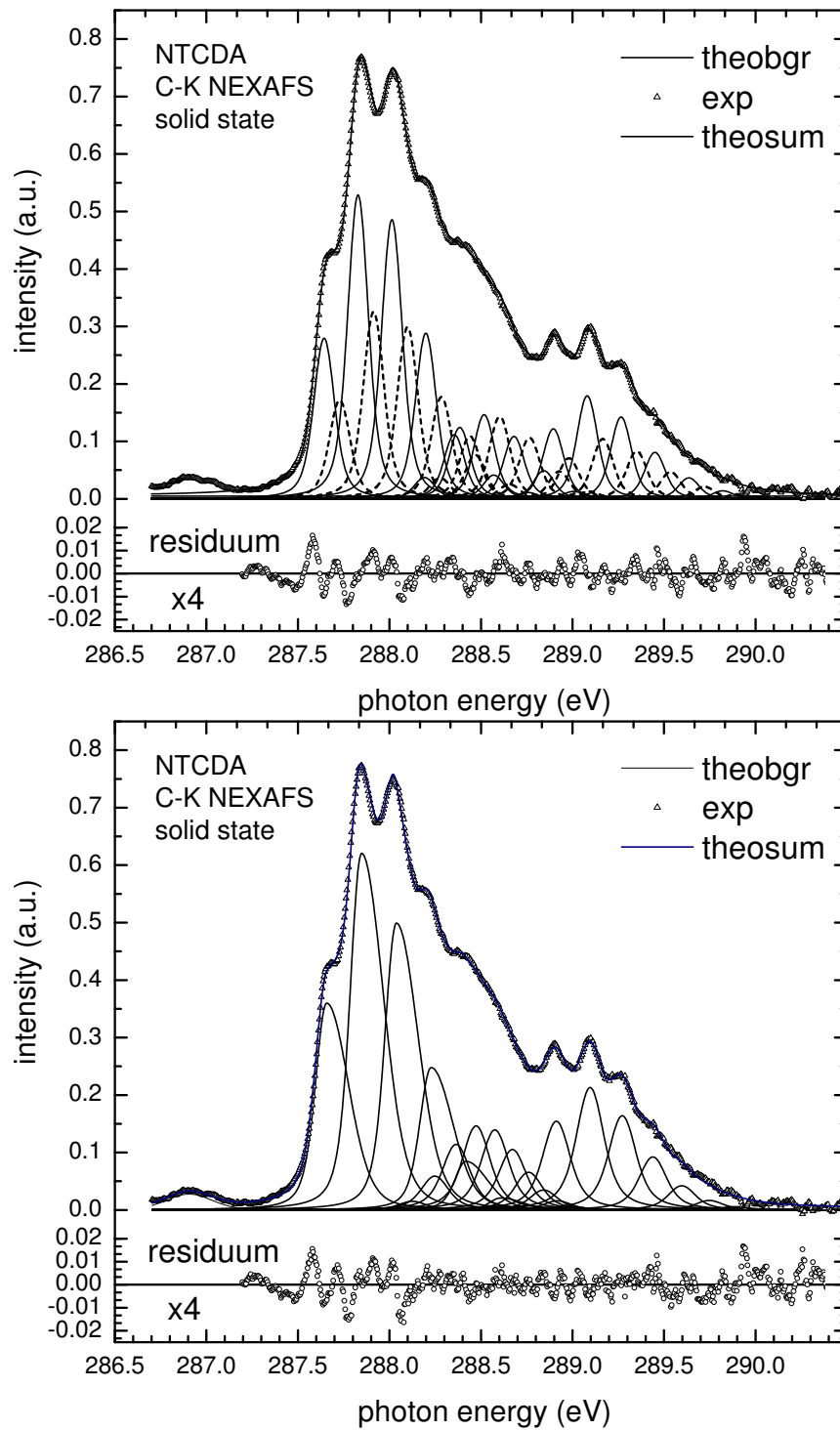
Figure 5.15: NTCDA feature γ of AML. Comparison of FC fit using splitted features (AML08, top) and an asymmetric line shape (AML02, bottom) as model for solid state effects. Fit parameters see table B.4.

5.4 PTCDA

When reporting on investigations on organic compounds, the 'drosophila of organics', PTCDA must not be missing. The interaction of PTCDA with surfaces is well understood by many studies of thin films on single crystals [102–106]. Also the electronic structure of PTCDA on metal single crystals has been intensively studied by XPS, UPS, and IPES [73]. UPS measurements of PTCDA in the gas phase have shown that the electronic structure of the valence states, especially below the HOMO-1, severely changes when the molecules form the solid state [29]. With the present investigation of gaseous PTCDA via NEXAFS, complementary information on the unoccupied levels is gained.

PTCDA is the largest representative in our systematic study of aromatic dianhydrides (for the structural formula and crystal structure see figure 5.16). The functional groups are identical to those of NTCDA, just the aromatic core is twice as large in PTCDA. In the free molecule, which belongs to the D_{2h} point group, we find seven carbon atoms in symmetrically different sites (C_1 to C_7) and again two chemically different oxygen atoms O_A and O_B.

PTCDA crystallises in the $P2_1/c$ space group with two molecules per unit cell and forms a herringbone pattern due to its quadrupole moment. Depending on the preparation conditions, two different bulk structures, the α and the β–PTCDA exist [107–109] which particularly differ in the stacking of the (102) plane.

The multilayer film presented in the following has been prepared on a clean Ag(111) substrate at a temperature of 150K. Under these preparation conditions, the β phase with flat lying molecules with respect to the substrate has been found [29, 103, 110]. The lattice constants are $a = 3.74(7)$, $b = 18.95(8)$, and $c = 10.75(9)$ and the angle between the a– and b–axis $\gamma = 96(1)°$ [107]. The solid state sample has been measured at room temperature at the beamline UE52/PGM at BESSY II. The gas phase spectrum has been measured in the gas cell at a temperature of about 650K at the same beam line.
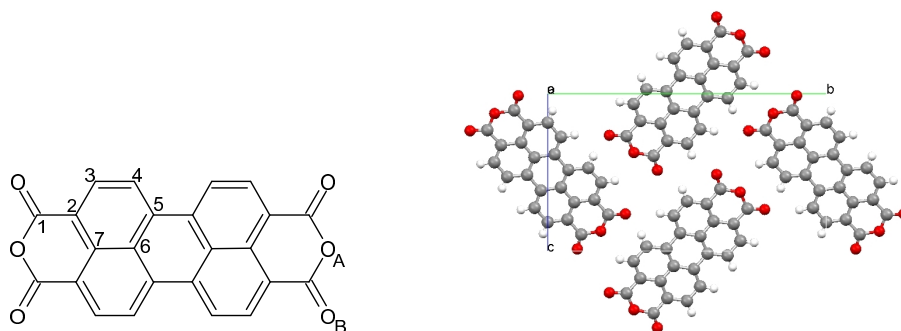
Figure 5.16: Structural formula of PTCDA (left) and crystal structure (right) of the β phase [90, 107] (view along the a–axis).
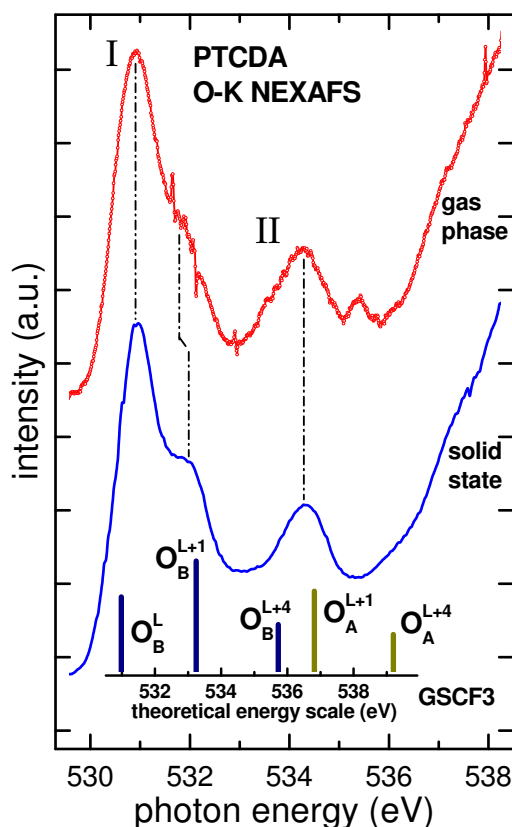
Figure 5.17: Gas phase spectrum (top), corresponding solid state spectrum (averaged over s– and p– polarisation, middle), and GSCF3 calculations (bottom). The small peak at 535.5 eV probably stems from the CO_2 contamination. For details on data processing, see chapter 3.6 and figure 3.7.

Given the high similarity of NTCDA and PTCDA in view of molecular shape and functional group, similar effects of solid state formation can be expected.

5.4.1 PTCDA O–K edge

The analysis of the PTCDA gas phase spectrum at the oxygen edge has been complicated by spurious contributions of CO and CO_2. Nevertheless, it was possible to reveal the pristine gas phase spectrum of PTCDA in a reasonable quality as described in detail in chapter 3.6. In figure 5.17, the gas phase spectrum (top) and the corresponding solid state spectrum, averaged over s– and p–polarisation (middle) are displayed together with the theoretical GSCF3 calculations (bottom). Of course the quality of the gas phase spectrum is not comparable to the BTCDA and NTCDA O–K spectra. Therefore the analysis will be limited to a more basic level in this case with special attention to possible effects caused by the data processing.

Two contributions from the O_B atom form the main peak (1s→L) and the shoulder (1s→L+1) of feature I. Feature II is built up by a 1s→L+4 transition at the O_B and a 1s→L+1 transition of the O_A atom.

As already shown for the O–K spectra of the other compounds investigated so far, the general shape of the gas and solid state spectra is very similar. Considering

the peak maxima[9] of the two main features, the spacing stays constant upon condensation. While the leading edge of feature I is identical in both phases, the solid state spectrum shows a much more pronounced shoulder at the trailing edge. This is accompanied by an increased FWHM of more than $0.3\,\mathrm{eV}$. The large change in FWHM clearly indicates a shift of the O_B 1s $\rightarrow$L+1 transition towards higher energy. Although the exact size of this shift can not be determined due to the low SNR in this region of the gas phase spectrum, $200\,\mathrm{meV}$ seem appropriate as an upper limit.

Feature II has to be considered with special care since its position and especially its shape strongly depend on the actual subtraction of the CO contamination. Therefore we just daresay that there is no dramatic change neither of the intensity, nor of the energy position or shape of the feature.

In the gas phase spectrum we find a small hump right after feature II which is not present in the solid state spectrum. The position right at the energy of the CO_2 contamination (see also figure 3.7) clearly indicates an improper subtraction of the spurious contribution. Different temperatures and pressures are plausible explanations for a discrepancy in the shapes of the CO_2 resonance for the gas cell and the reference spectrum.

5.4.2 PTCDA C–K edge

Figure 5.18 displays the C–K NEXAFS spectra of PTCDA in the gas phase (top) and the solid state (middle) together with the result of the GSCF3 calculations (bottom). In the gas phase spectrum, the spurious CO contamination has been subtracted as described before in chapter 3.6.

As the calculations show, many different electronic transitions contribute to the individual features. In feature α contributions from all carbon atoms except the C_1 and C_4 are found. All transitions are 1s$\rightarrow$L+1 except for the C_5 1s$\rightarrow$L.

A similar situation exists for feature β. The shoulder of the leading edge is very probably built up by the C_7 1s$\rightarrow$L+2, the main part by C_{3-5} 1s$\rightarrow$L+1 and the C_6 1s$\rightarrow$L+2 transitions. Interestingly, the shape of both features is still very similar to those of NTCDA, despite the much larger number of subjacent electronic transitions. Probably, the individual transitions at the perylene ring system do not differ as much in excitation energy as proposed by the calculations.

In feature γ, the situation is very different since it is solely[10] based on transitions from the C_1 carbon atom. The leading edge is formed by the 1s$\rightarrow$L transition that partly overlaps with the 1s$\rightarrow$L+1 transition building up the middle part of the

---

[9]Using the onsets as a measure, a differential shift can be observed. However, we like to recall the change due to the contaminations which may alter the shape of the main feature and thereby also the onset position.

[10]The FC analysis in the next section shows that the small C_5 contribution in between can be neglected.
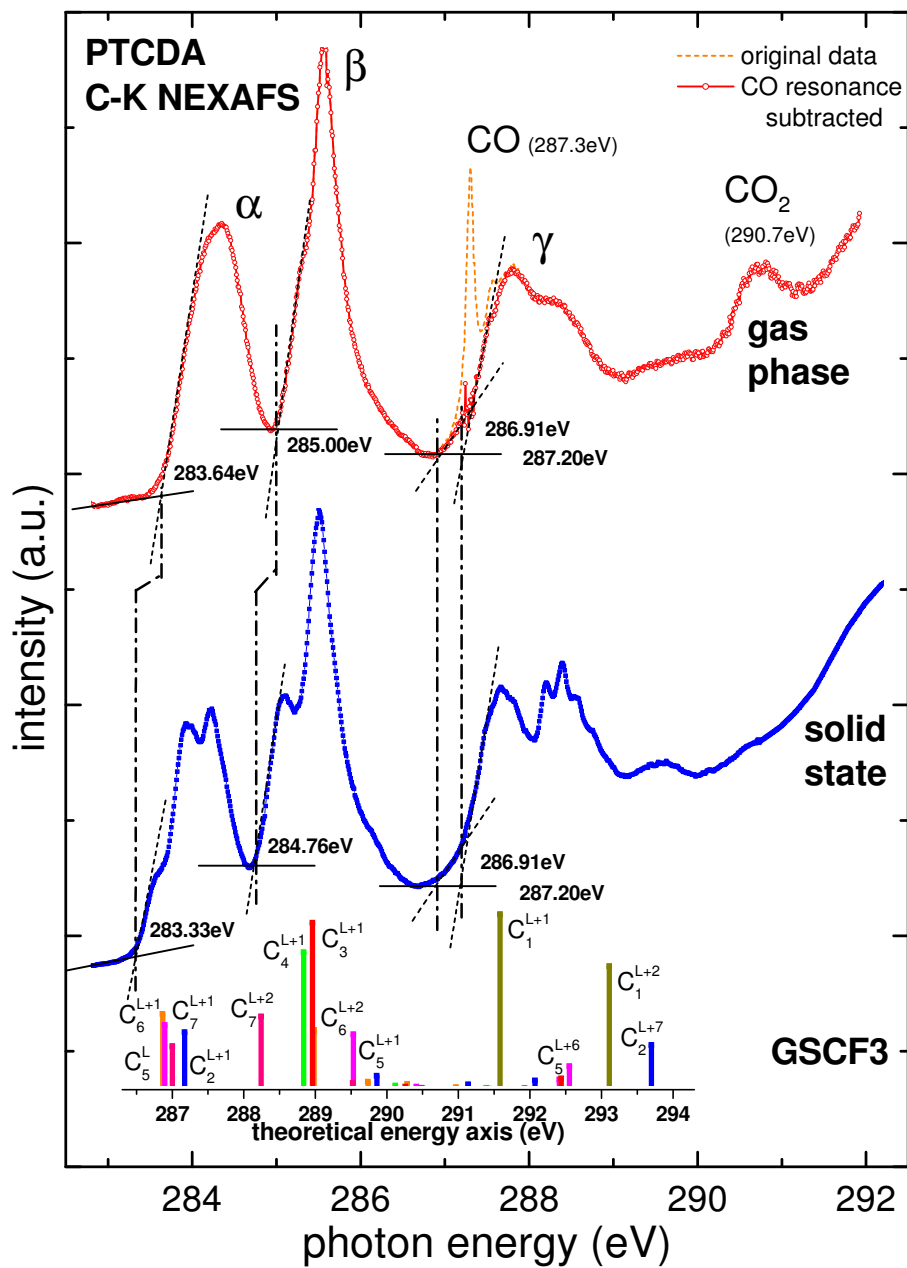
Figure 5.18: C–K edge of PTCDA in gas (top) and solid state (middle) with GSCF3 calculations (bottom).

feature. The trailing edge with a contribution from the C_2 1s $\rightarrow$L+7 directly merges with the absorption edge.

Compared to the other dianhydrides, the relative intensity of feature γ is smaller. This is due to the increased aromatic ring system whereas the number of C_1 atoms is constant. In contrast to NTCDA for example, the shape of feature γ is much more altered by solid state formation. The broad doublet feature of the gas phase splits into two clearly separated parts, one of which develops a very distinct vibrational fine structure.

The trend of a better resolved fine structure in the solid state spectrum for an increasing molecular size is clearly continued with PTCDA. Each feature of the solid state spectrum shows a distinct fine structure, whereas the gas phase spectrum is completely featureless. This is attributed to the very high gas cell temperature of about 650K whereby low energy vibrational modes up to 85 meV can be thermally populated in the electronic ground state. For PTCDA about twelve normal modes exist in the respective energy range, primarily folding– and bending–modes [111] that may smear out any distinct features in the gas phase.

Turning to the energy positions of the individual features, we find again differential shifts in the order of several hundred meV.

The onset of feature α is red–shifted by 0.31 eV in the solid phase, also the trailing edge moves towards lower energy. Therefore more than one transition has to be affected by solid state formation that causes the splitting of the broad gas phase feature into three very distinct parts.

In feature β, a 0.24 eV red–shift of the onset is observed, whereas the energy of the peak maximum is almost unchanged. Possibly, the main effect is caused by a shift of the C_7 1s$\rightarrow$L+2 transition which then produces the very pronounced shoulder in the solid phase.

In feature γ, the determination of the onset is complicated by the special shape of the leading edge. However, two different attempts accordingly yield identical onsets for the gas and solid phase.

5.4.3 FC fit analysis of PTCDA C–K edge

As already mentioned, the wealth of electronic transitions in the PTCDA C–K spectra makes a comprehensive FC analysis impossible. Solely feature γ, with just three different electronic transitions, provides a reasonable basis for a more detailed fit analysis.

In contrast to the other dianhydrides, the leading edge does not provide enough structure to perform a precise line shape analysis. Just the middle part, built up by the C_1 1s$\rightarrow$L+1 transition, shows enough distinct features as a basis for a reasonable fit. Therefore the leading and trailing edge are rather considered as background for the well resolved progression and will not be analysed in detail. Figure 5.19 shows that it is possible to very well reproduce feature γ, despite all the constraints

Table 5.4: Parameters of PTCDA FC analysis for feature γ. All values are given in eV except for int, sh, and sc. The line widths of the C_1 1s→L+1 transition have been used for the C_1 1s→L+2 transition as well.

	C_1→L+1	C_1→L+2
pos	*287.33*	*288.20*
int	*1.122*	*0.961*
Γ_G	*0.150*	*0.150*
Γ_L	*0.087*	*0.087*
δ	*0.164*	*0.202*
sc	*0.959*	*1.100*
sh	*2.429*	*1.653*
ξ	*0.000*	*0.022*
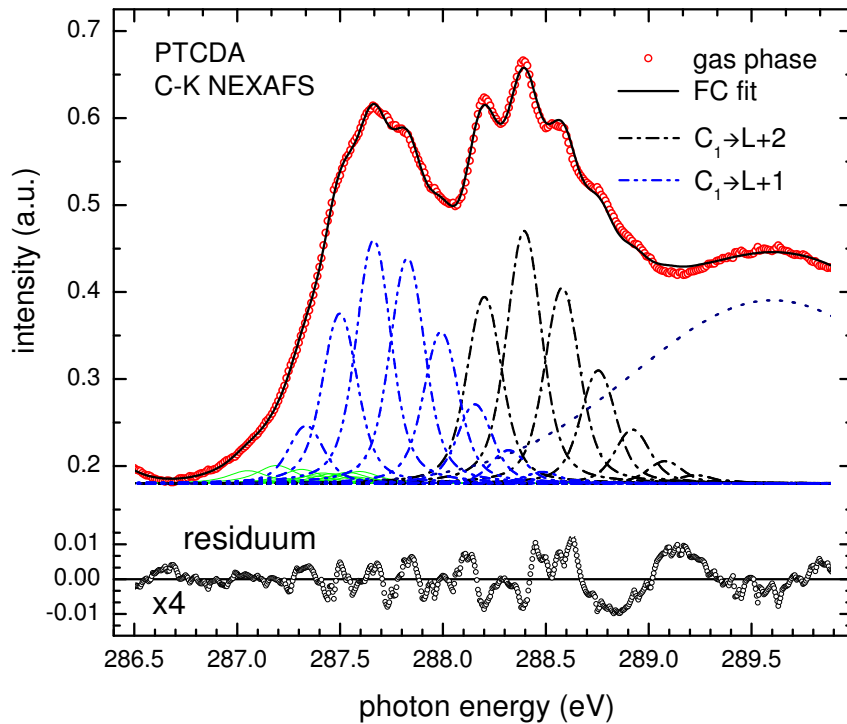
Figure 5.19: Result of the FC analysis of PTCDA feature γ in the solid state.

named above. The respective fit–parameters are listed in table 5.4, for the sake of completeness, the results of the C_1 1s→L+1 transition are given as well.

The vibrational spacing of the C_1 1s→L+1 transition is predetermined by the distinct fine structure in the middle part of the feature and can be assigned very exactly to 200 meV. Admittedly, the leading edge of this progression completely overlaps with the trailing edge of feature γ_a. Thus, the energy position of feature γ_b can not be determined very exactly, whereby the potential parameters, which strongly depend on the overall shape of the progression, have to be considered with some precaution. Calculating the vibrational spacing in the ground state results in a relatively large value of 260 meV. The highest normal mode observed by high resolution electron energy loss spectroscopy (HREELS) in a PTCDA multilayer [111] is a C=O stretching mode with a wavenumber of 1771 cm^{-1} (220 meV). Although stated by theoretical density functional theory (DFT) calculations, no normal modes above this energy have been observed by HREELS or fourier transform infrared (FTIR) spectroscopy [112].

Given the uncertainty of the potential parameters, the agreement within an error of less than 20% is still reasonable. The assignment to the C=O stretching mode is corroborated by the similar findings for the other dianhydrides and recent NEXAFS investigations of 3,4,9,10–perylene–tetracarboxylic acid diimide (PTCDI) [113]. Although feature γ is chemically shifted by about 0.2 meV in case of PTCDI, the fine structure is still very similar to that of PTCDA.

Unfortunately the gas phase spectrum is not suited for a FC analysis so no information can be gained about the change in line width from one phase to the other.

5.4.4 Comparison with UPS investigation

For PTCDA, also gas phase measurements by means of UPS have been performed in a former work [29] (see figure 5.20). Compared to the differences observed in solid state and gas phase UPS spectra [29, 79], the changes in the NEXAFS spectra are rather small. Since the final state is *ionic* in the case of UPS, and *neutral* for the NEXAFS process, this difference is not very surprising. Also the absence of a comparable energy shift due to polarisation of the surrounding molecules in case of the solid state NEXAFS spectrum can be attributed to this fact.

Also the UPS spectra show differential shifts and intensity changes that are, in contrast to the NEXAFS results, not so easily assigned to specific orbitals. Interestingly, the vibronic coupling of the HOMO is much better resolved in the gas phase, and the Gaussian line width is even smaller compared to the vibrational coupling in the solid state NEXAFS feature γ. This contradicts to some extent the picture of temperature broadened gas phase spectra. Of course, the core states may be much more sensitive to vibrations due to their local character compared to the valence states.
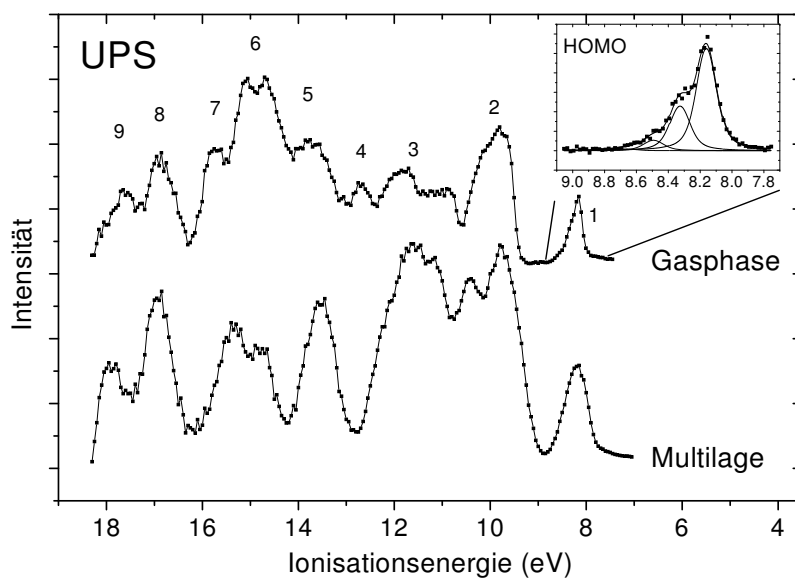
Figure 5.20: Gas phase (top) and solid state (bottom) UPS spectrum of PTCDA, taken from reference [29]. FC analysis of the HOMO resonance is plotted in the inset. To align the HOMO levels the solid state data have been shifted by 1.2 eV, representing the reorganisation energy.

Both, the UPS and the NEXAFS investigation have in common, that the observed changes in intensity, peak shape, and energy positions can not be explained easily with the commonly applied models of a weakly coupled van–der–Waals crystal.

5.4.5 Summary of PTCDA results

In this chapter NEXAFS gas phase data for PTCDA, the hitherto largest organic molecule investigated, have been presented. We find detailed differences between gas phase and solid state spectra in energy position and shape of features primarily at the C–K and, in contrast to all other molecules so far, also at the O–K edge. At the C–K edge the changes are similar to those already reported for other dianhydrides. Red–shifts for all features except for γ are again observed, increased in size compared to the other molecules. Surprisingly, the fine structure is much more distinct for the solid state than for the gaseous molecule.

In spite of the numerous electronic transitions, most changes could be assigned to specific atoms and transitions. For feature γ, the fine structure, apparent in the solid state spectrum only, was analysed and the underlying vibration assigned to a C=O stretching mode.

5.5 Discussion for Dianhydrides

The following section will give a summary of the important results obtained for the series of the dianhydrides BTCDA, NTCDA, and PTCDA. For a more comprehensive approach to the molecular interaction, the observed changes between the gas and the solid phase will be considered in conjunction with molecular and crystal geometry. The different theoretical models that have been introduced in chapter 2.6 and come into consideration will be discussed afterwards.

5.5.1 Wrap–up of results

For a better orientation, an overview of all spectra taken at the C–K edge is given in figure 5.21.

Molecular and crystal structure

First, we want to recall the main points of the molecular properties and the crystal phases. All three molecules have the same functional group and just differ in size of the aromatic core. While the free molecules in the gas phase belong to the D_{2h} point group, the molecular symmetry is reduced to C_i in the solid phase.

When considering the molecular geometry[11] within the crystal structure [80, 89, 107], special care has to be taken concerning the position of the hydrogen atoms. Since the hydrogen positions are difficult to be determined precisely using x–ray diffraction (XRD), [114, 115], the deduced C–H bond–lengths and to some degree the bond–angles are probably wrong. Therefore, C–H bond–lengths of aromatic compounds determined by neutron scattering [116] have been used instead[12]. However, small deviations from real bond–length and bond–angles can not be excluded entirely.

The character of the distortion of the molecules, that comes along with the condensation, is similar for the individual compounds, but becomes more distinct with increasing size.With respect to the plane of the aromatic core, the O_B and the adjacent C_1 atom show the largest deviation (see table 5.5). The twisting of the functional group increases slightly from BTCDA to NTCDA, and is nearly doubled for PTCDA. Compared to the free, planar molecules of the gas phase, bond–lengths and bond–angles only change within a few per cent.

The molecules condense in different crystal structures, BTCDA in a tetragonal lattice with space group $P4_2/n$, NTCDA and β–PTCDA monoclinic with $P2_1/c$ symmetry. While the PTCDA molecules are all parallel, the molecular planes of

---

[11]The geometries of the free molecules have been determined by DFT calculations using the B3–LYP functional and a 6–31G basis set.

[12]In chapter D.2.2 a comparative calculation for the different C–H bond lengths given for NTCDA impressively documents their influence on spectral features.
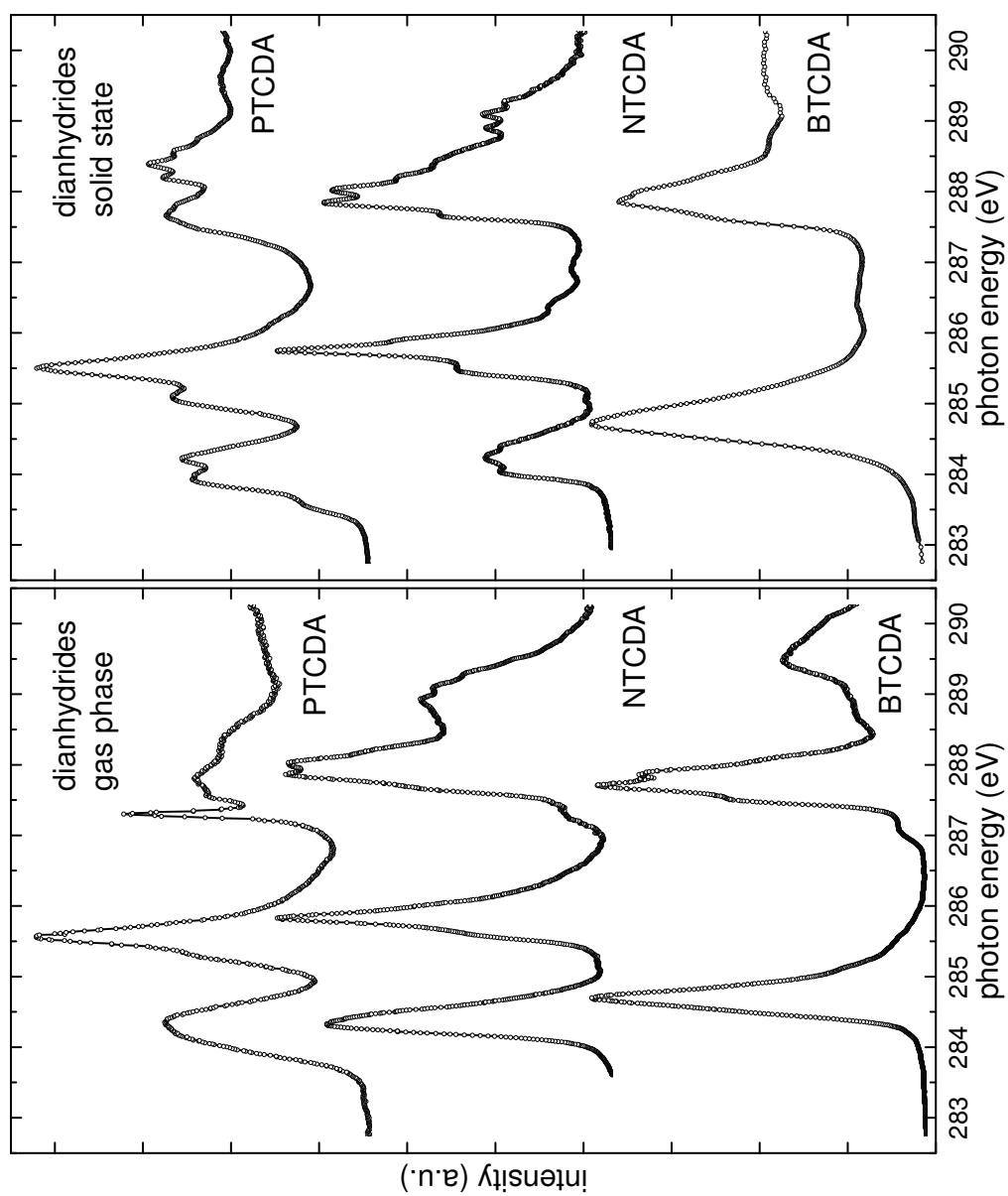
Figure 5.21: Overview of C–K NEXAFS spectra of dianhydrides in the gas phase and the solid state.

NTCDA and BTCDA are tilted 68° and 87° with respect to their next neighbours which are therefore referred to as *angled neighbour* (AN) in the following.

The extended π–systems of all compounds make the stacking axis probably the most important direction concerning intermolecular interaction. Figure 5.23 depicts the overlap of the molecules in a stack with a view perpendicular to the plane of the aromatic system. Not only the overlap increases from BTCDA to PTCDA, but also the interplanar distance of two adjacent molecules decreases extremely (see figure 5.23).

As both, the molecular shape itself, and its surrounding heavily depend on the size of the molecule, the question arises whether these changes are also reflected in the NEXAFS spectra.

General effects

In the gas phase as well as in the solid state, the FWHM of the spectral structures increases with the size of the molecule. On the one hand this broadening can be caused by additional normal modes available in larger molecules. On the other hand, additional electronic transitions necessarily come along with an increasing number of symmetrically non–equivalent atoms. For the gas phase spectra, increasing temperature contributes to the line width.

With increasing size of the compound under investigation, the observed shifts of the NEXAFS features also increase. Table 5.5 lists the respective onset–shifts between gas and solid state NEXAFS spectra relative to the highest energy feature γ.

Besides the increasing shift, we also find an increasing change in shape for features α. While in BTCDA both phases can be described by similar vibrational structures, in NTCDA already a real splitting of the feature occurs. Even without a FC analysis, a severe change in vibrational coupling is evident. The same applies for PTCDA, where the splitting gets even more pronounced, even though many more transitions contribute to this feature.

Features β in NTCDA and PTCDA look very similar and the main peak is built up by the C_3 1s$\rightarrow$L+1 transitions in both cases. The shoulder that is mainly responsible for the shift in case of PTCDA, stems from the C_7 and the C_4 atom, respectively which have an identical chemical surrounding in PTCDA and NTCDA. The orbitals of the corresponding transitions are also very similar for both molecules (see tables C.1 and C.2).

For BTCDA and NTCDA a small peak is observed at the foot of feature γ, assigned to a C_2 and C_3 1s$\rightarrow$L+2 transition, respectively. Assigning these transitions also to the peak in between features β and γ in the solid state spectra, means a rather large shift of more than 0.3 and 0.6 eV, respectively. This assignment can only be maintained since it is observed for both compounds and no other transitions are predicted in this energy range.

Table 5.5: Differential shifts of features α and β between Dianhydride NEXAFS spectra of gas and condensed phase. Deviations from the mean plane of the aromatic system of molecules in the solid phase, given in Å. Atoms with largest deviations are denoted only.

	$\Delta\overline{\alpha\gamma}$	$\Delta\overline{\beta\gamma}$	C_1	C_2	C_3	O_A	O_B
BTCDA	0.17 eV	—	0.039	0.001	0.001	0.031	0.090
NTCDA	0.25 eV	0.18 eV	0.046	0.009	0.003	0.031	0.101
PTCDA	0.31 eV	0.24 eV	0.087	0.016	0.009	0.053	0.198

All spectra accordingly show no significant change in energy of feature γ which arises from transitions at the C_1 atom in all cases. The performed FC analyses have shown that this transition always couples to a C=O stretching vibration. The resulting fine structure is getting better (worse) resolved in the solid state (gas phase) with increasing molecular size (see also chapter 5.6). This fact has been attributed to an increasing thermal broadening in case of the gas phase.

5.5.2 Models for interaction

Putting all facts gathered so far together, we will now try to find a model that may describe the observations for all molecules. Three different models will be discussed.

Molecular geometry

In general we have seen that differences between gas phase and solid state spectra are very similar for all dianhydrides, despite a very different arrangement of the molecules in the crystal. Especially the mutual orientation of the nearest neighbours differs considerably for, i.e., BTCDA and NTCDA. The increasing molecular size, however, not only comes along with an increase of the energy shifts, but also with an increased distortion of the molecules, as is shown in table 5.5. Therefore it is quite plausible that the molecular structure itself rather than the crystal structure is accountable for the observed changes upon condensation.

The general increase of FWHM and the splitting of transitions, respectively, as observed for features α for example, can be attributed to the reduced molecular symmetry in the solid phase. The splitting of degenerate levels in a crystal is also known as the Jahn–Teller effect [35]. In case of NEXFAS spectroscopy, however, it is the degeneracy of the core levels, not of the valence levels or of the unoccupied levels that is revoked due to the reduced symmetry in the crystal. Also the calculations for gas phase and crystal geometry, presented in figure D.1 yield an, admittedly small ($\simeq$30-60 meV), splitting of most transitions, caused by the no longer symmetry equivalent atomic sites. By introducing nearest neighbours, this effect is even enhanced, as is shown in figure D.2.
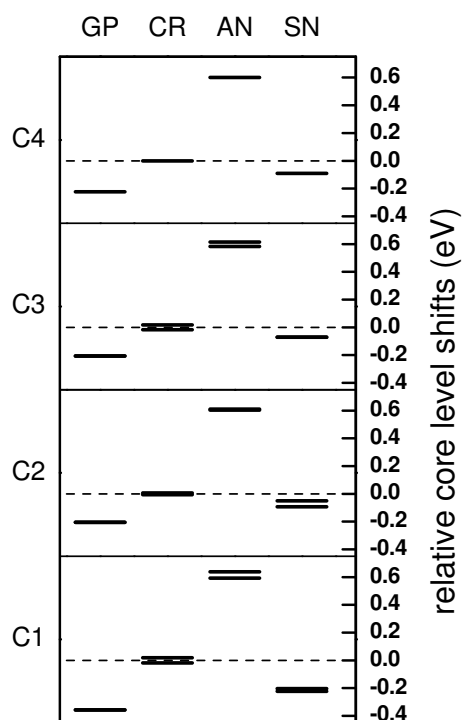
Figure 5.22: Shifts of C 1s core levels of NTCDA for different molecular structures (gas Phase (GP), crystal (CR), angled neighbours (AN), and stacked neighbours (SN)) with respect to the C1s core level of the single molecule in the crystal structure (CR).

Especially for features β and γ in the NTCDA solid state spectrum, this can provide an alternative explanation for the pronounced shoulder at the leading edge. This structure could only be reproduced satisfactorily using a doubled vibronic progression and was therefore assigned to a Davydov Splitting [92].

Due to the altered molecular geometry in the crystal, also differential shifts are observed in the calculation for NTCDA (see figure D.1). Although these results do not agree well with the experimental data, they are still a strong hint that even very small differences in molecular geometry can alter the electronic transitions considerably.

However, similar shifts and also a splitting is observed for calculations of the O–K edge, quite contrary to the experimental findings for NTCDA. This is also the main weakness of the molecular geometry model. Those parts of the molecule that show the largest difference in geometry, namely the oxygen atoms and the C_1 carbon atoms, exhibit in general no differences in the NEXAFS spectra.

In summary, we can say that the molecular structure certainly has an effect on the NEXAFS spectra, but never can solely explain all the detailed differences found between gas and solid phase. In fact, the distorted molecule has to be considered within its surrounding of nearest neighbours.

| 4.43Å | 3.52Å | 3.34Å |
| BTCDA | NTCDA | β–PTCDA |
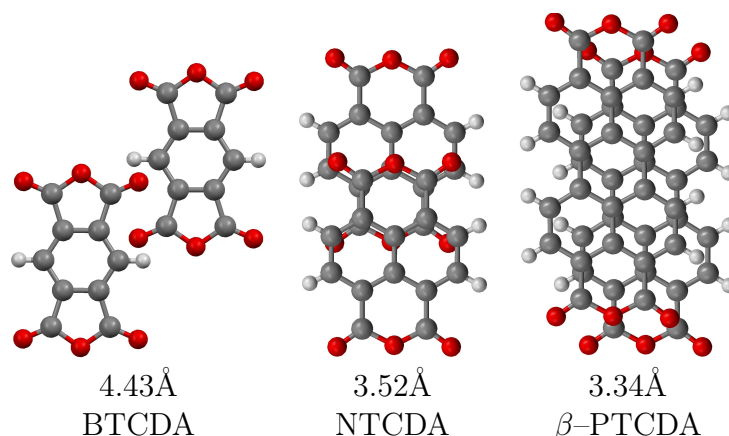
Figure 5.23: Overlap of stacked molecules, view perpendicular to plane of aromatic system. Interplanar distance.

Orbital interaction

This consideration consequently leads to a model of nearest neighbour interaction, incorporating directly interacting wave functions. If the molecules in the crystal are packed closely enough, their wave functions will begin to overlap. In view of linear combination of orbitals, this will result in a splitting or even more complex redistribution of molecular orbitals. Thereupon, shifted, split, and also new transitions may be found in the solid state NEXAFS spectra.

For NTCDA this model is quite plausible since the molecules are stacked with large overlap and at a distance that comes close to the sum of the respective van–der–Waals radii (see figure 5.23). PTCDA is packed even more closely and the adjacent molecules almost overlap completely. Consequently, the increased overlap will increase the energy splitting, which in turn causes the larger shifts observed in the PTCDA NEXAFS spectrum.

Also the more pronounced features of the NTCDA AML spectrum compared to the CML spectrum can be readily explained by an enhanced overlap of the molecular orbitals caused by a better mutual alignment of the molecules upon annealing.

Considering the NTCDA crystal structure, even explanations for the differential shifts may be found. The C_3 and C_4 carbon atoms for example, where most spectral changes are observed, may be affected directly by the oxygen atoms of the next molecule in the stack. The C_1 atom in contrast only sees the subjacent aromatic naphthalene core.

The C_1 carbon atoms of PTCDA in contrast, are directly located above the O_A and O_B oxygen atoms of the next molecule in the stack. However, for both compounds, transitions of the C_1 atom do not shift upon condensation.

For BTCDA, it is admittedly hard to imagine that the overlap as such is responsible for changes similar to those found for the other two compounds. BTCDA has no

overlap with its stacked neighbours and the interplanar spacing is relatively large (see figure 5.23). Nevertheless, it is of course still possible that BTCDA couples to its angled neighbour via the numerous short contacts[13] that are, admittedly, not located at the ring system.

Also for NTCDA, the remaining neighbours, especially the angled neighbour (AN), have to be taken into account as well. This means that also the C_1 carbon atom has neighbouring oxygen atoms at short contact distances to interact with.

In order to approach this model from a more technical point of view one has to have a look at the excited, as well as the ground state molecular orbitals (see chapter C). For an essential interaction of wave functions, widely spread orbitals are advantageous. Especially orbitals extending perpendicular to the molecular plane, or reaching in direction of the next neighbour, can more effectively interact with each other. On the other hand, a firm spatial separation is needed to explain the observed differential shifts that state very different conditions for different atomic sites.

To judge from the orbital plots, whether the above mentioned criteria apply or not, is very difficult. Essentially, the spatial differences between energetically shifted and non–shifted orbitals should be much more pronounced than the differences among the respective party.

In view of delocalisation, no general difference between the two parties can be observed[14]. Also for the surrounding of the excited atom in the molecule, no general trend is seen regarding the orbital arrangement.

For the overlap and resulting coupling of the orbitals one always has to bear in mind that the overlap needs not to occur right at the excited atomic site. In fact, any interaction of the respective orbital may (but does not have to) affect the orbital energy, which is of course constant for the whole orbital. Therefore, overlapping of an orbital at one end of the molecule may affect the excitation energy of an atom right at the opposite end of the molecule. In addition, for most transitions the assignment to the 'shifted', and 'non–shifted' party is admittedly ambiguous.

Consequently, no clear statement can be drawn from the mere inspection of the molecular orbitals.

To shed more light on the influence on the molecular orbitals, quantum chemical calculations are indispensable. Already 'Z+1' calculations (631G(d,p) basis set) can help to find out, for example, which neighbours mostly affect the excited molecule.

For the stacked nearest neighbours SN of NTCDA, a sharing of wave function–density is already observed for some orbitals in the ground state and several excited molecular orbitals. The transition energies at the C–K edge exhibit a general increase

---

[13]Distances that are smaller than the sum of the van–der–Waals radii of the respective atoms.

[14]The degree of orbital distortion compared to the ground state of course differs among the orbitals, but is similar for shifed and non–shifted excitations. Extreme changes are observed for the PTCDA C_7 L+1 and the mixed Rydberg orbitals of C_3 in BTCDA and NTCDA (L+3 and L+4, respectively).

in the order of $0.3\,\mathrm{eV}$ due to the presence of the stacked neighbours. Differential shifts with respect to the C_1 1s→LEMO transition are about 10 to $20\,\mathrm{meV}$ (see figure D.2). Although this finding is not conform with the experimental data, it shows that interactions between adjacent molecular orbitals are possible in principal.

For the angled neighbours, an overlap of wave function–density can only be observed for the L and L+4 orbital of the C_3 carbon atom. Compared to the stacked neighbours, this sharing of orbitals is rather small. These neighbours cause as well a blue–shift of about $0.3\,\mathrm{eV}$ for all transitions. Differential shifts with respect to the C_1 1s→L transition are in the order of $\pm\,100\,\mathrm{meV}$ (see figure D.2). The splitting of some levels, already observed for the single molecule in its crystal geometry, is further enhanced by the angled neighbours.

As shown in figure 5.22, a large portion of the shifts and splitting of the transition energies is already introduced by the core levels. Especially for the C_2 it is quite evident that the splitting occurs in fact not until the stacked neighbours are introduced.

At present more advanced calculations using the WAVELS code are being carried out, the results are therefore still pending. Even more sophisticated, and therefore also more demanding calculations, amongst others taking into account configuration interaction and dispersive forces are being set up at present.

Excitonic coupling

Extending the model of a static kind of interaction of the molecules, a dynamic interaction between the excited molecule and its neighbours is the next step. As shown in chapter 2.6.2 (equation (2.25)), an excitonic coupling between the excited molecule and adjacent non–excited molecules, mediated by the electric field vector, is the appropriate approach.

In contrast to the previous models, a splitting of transitions can be attributed to the crystal structure, without the need to revert to the reduced symmetry of the distorted molecules in the crystal.

As a first qualitative approach to this model, the mutual alignment of neighbours can be considered.

According to (2.30), the coplanar stacked neighbours of NTCDA and PTCDA will cause a red–shift of excitonic coupled transitions. In table 5.6 the relevant parameters, the angle θ between transition dipole and line of molecular centres and their spacing x are listed for the stacked neighbours of the dianhydrides. Due to the smaller spacing and the better overlap, i.e. smaller θ in case of PTCDA, the shift will turn out larger as compared to NTCDA (see also figure 2.4). BTCDA in contrast is put into a region of negligible energy shifts due to the relatively large spacing and lateral displacement of its stacked neighbours.

The angled neighbours of BTCDA and NTCDA may cause a splitting of transitions, since both components of the exciton splitting term (positive and negative) in

Table 5.6: Geometry consideration for excitonic coupling of stacked neighbours. θ denotes the angle between polarisation axis and the line of molecular centres, whose spacing is given by x. See also figure 2.4.

	BTCDA	NTCDA	PTCDA
θ	53°	48°	26°
x	7.4Å	5.3Å	3.7Å

equation (2.25) have a significant transition probability. In case of PTCDA, where no angled neighbours are present, this part has to be taken over by the reduced molecular symmetry in the crystal again.

Altogether, already the nearest neighbours may explain most observed features for the dianhydrides in a reasonable way. Far–off neighbours may be neglected since the splitting term is inversely proportional to r^3.

For a better understanding of the potential influence of the different adjacent molecules, calculations of the geometry part G in equation (2.31) have been performed for NTCDA and its nearest neighbours. Figure 5.24 depicts these geometry factors G classified by the individual neighbours (SN, AN, and SI) and the individual carbon species (C_1 to C_4). Each bar represents the geometry factor of two carbon atoms of the same species located in two neighbouring molecules.

On the conditions mentioned in chapter 2.6.2, we find in general an energy lowering[15] for the stacked neighbours (SN), which is in agreement with the experimental findings. In addition, some very effective couplings, for the C_1 and C_2 atoms are found. The angled neighbours (AN) in contrast do not show such peaks and offer a more homogeneous result. Just the side neighbours (SI) yield an, albeit small, general increase, except for one negative peak at the C_3 atom. Although these pronounced geometry factors for certain atomic pairings may lead to differential shifts, the results are not in good agreement with the experimental data.

More sophisticated calculations for the angled neighbours using the extended WAVELS code have also been performed [49]. In accordance with the geometry considerations, no prominent shifts for special atoms have been found. The general splitting in energy, however, is in the range of a few meV and therefore quite small. For the other neighbours, results are still pending. Given the more heterogeneous geometry factors of the other neighbour species (figure 5.24, SN and SI), more differentiated results may be expected.

The theory of excitonic coupling also provides a 'van der Waals term' (see equation (2.26)), that equates to an extramolecular screening varying with the atomic site which has been excited. Thus, differential shifts may be explained by a different reaction of the surroundings to different excitations. A splitting of

---

[15]For PTCDA, an increased shift caused by the stacked neighbours could be reproduced as well.
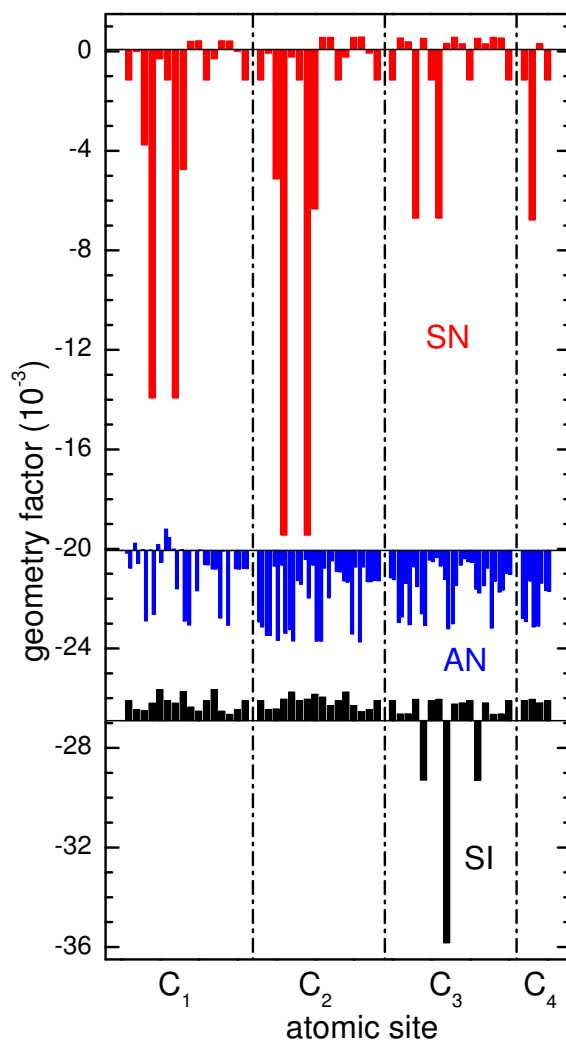
Figure 5.24: Geometry factors G (see equation (2.31)) for NTCDA stacked (SN), angled (AN), and side (SI) neighbours. Each bar corresponds to a coupling of two atoms of the same species on two neighbouring molecules. Negative values correspond to a red–shift. For better visibility the plots of the AN and SI are shifted downwards.

transitions, however, again depends on the reduced symmetry of the molecule just as in case of the orbital coupling or pure molecular geometry models.

To calculate the size of this effect, the interaction with 'all' other molecules in the crystal has to be taken into account. Since this issue is not easy to tackle, no theoretical calculations are available yet.

In summary, the model of excitonic coupling is in principle capable of explaining all observed features, as has been shown by the geometric considerations in figure 5.24. In order to reliably reproduce the experimental findings, highly sophisticated calculations are needed and are being performed at present.

5.5.3 Summary of dianhydrides

At first glance, all presented models seem very plausible, and an appropriate one may be found for each individual compound. In the comprehensive comparison, however, severe discrepancies become evident, unmasking the proposed models to oversimplify reality when considered separately. Therefore, a combination of some, or maybe even all introduced theories may be needed to adequately describe the observed effects for all three molecules.

Due to the complicated crystal structure with several neighbours that have to be taken into account, simple estimations for whatever model are bound to fail, and the support of high quality quantum chemical calculations is needed. At present, supplementary calculations are being performed (effect of neighbours, excitonic coupling), others are being set up (van–der–Waals term, including configuration interaction, etc.).

In view of the experimental side, the investigation presented here shows that it is not yet well understood how sensitive NEXAFS really is on changes in molecular and crystal structure. Basic experiments, like NEXAFS on single crystals in different morphologies, may help to shed some more light on this issue.

5.6 Vibrations

The changes of vibronic properties of large organic molecules in different environments has been the aim of many spectroscopic investigations [22]. While HREELS, Raman, and FTIR spectroscopy probe the molecular vibrations directly in the ground state, PES and NEXAFS investigations yield information on the vibronic properties in the electronically excited molecule. Therefore, different vibronic energies are observed with theses spectroscopic methods. As already mentioned in chapter 2.3, for small molecules the ground state vibronic energies can be calculated quite exactly using equation (2.9). In order to verify this correlation for the large organic molecules investigated in this work, as many data on vibronic structures as possible have to be gathered. The data presented in the following stem from FC analyses of the present work and former investigations [16, 93, 117].

The vibronic energies can be determined from the FC fits with an uncertainty in the range of about 10%. The Franck–Condon shift ΔE_{FC} has been determined from the 0–0 transition and the maximum intensity of the respective progression. The uncertainty of this method is about 25 to 50% of the respective vibronic energy. In table 5.7 all collected vibrations are listed, including the vibronic parameters.

Figure 5.25 displays the vibrations for the different molecules. The energy axis shows the Franck–Condon shift, at the y–axis the energy ratio of the ground state vibration $h\nu_0$ to the vibration in the excited state $h\nu$ is displayed. Empty symbols represent gas phase data, filled ones solid state measurements. The dashed line depicts the dependence according to (2.9). Since several different normal modes of the ground state come into consideration for each vibration observed in the excited state, also several energy ratios appear for one particular Franck–Condon shift. The individual, closely spaced normal modes are bundled to vibronic bands of C–H and C=O stretching, and C–C skeletal modes for most molecules.

As can be seen in the plots of the anhydrides BTCDA, NTCDA, PTCDA, and NDCI, the C=O stretching vibrations fit very well to the predetermined line. The correct assignment is therefore quite obvious, and the other ground state modes with a very different energy ratio may be omitted. The same approach can be applied for the other data sets, though the assignment is not as clear in some cases. Putting all these data together, results in the plot shown in figure 5.26, where the omitted vibrations are plotted in light grey.

From this plot, also the limitations of this investigation become evident. While a lot of data points are available for Franck–Condon shifts in the range of 0.2–0.4 eV, higher energies are not as frequent. Therefore the correct dependency, linear or non–linear, is not as evident, and different lines can be found describing the data points comparatively well. However, the trend of increasing frequency ratios with increasing FC–shifts is unambiguous, but can not be quantified as an exact linear slope.

Nevertheless, valuable information can be extracted from this plot. The linear curve can be used as a reference to rate the validity of the proposed model and the FC analysis for the respective spectrum. In case of BTCDA for example, all but one vibrations fit very well to the proposed linear line. The outlier affiliates to the solid state FC fit that has also been rated as not very reliable in the data evaluation (chapter 5.2.3). The same applies to the highest FC shift for NTCDA, which is associated with the second progression in feature γ (see chapter 5.3.3). While the first and third progression with $\Delta E_{FC} = 0.24$ and 0.27 eV, respectively, could be fitted readily due to the rich fine structure, the fit of the second progression is rather ambiguous. This uncertainty is reflected by the rather large discrepancy in this plot.

In summary, for future FC analyses the correct vibronic assignment should be checked already during the fit procedure by a comparison with ground state vibronic energies using equation (2.9). In order to increase the reliability of this plot, additional data points should be added in the future.

Figure 5.25: Ratio of vibronic energy in the ground– and excited state, plotted versus the Franck–Condon shift ΔE_{FC} for different large organic molecules. Each point represents one possible assignment of a vibronic ground state mode, resulting in several points for one ΔE_{FC}. Open symbols represent gas phase data.
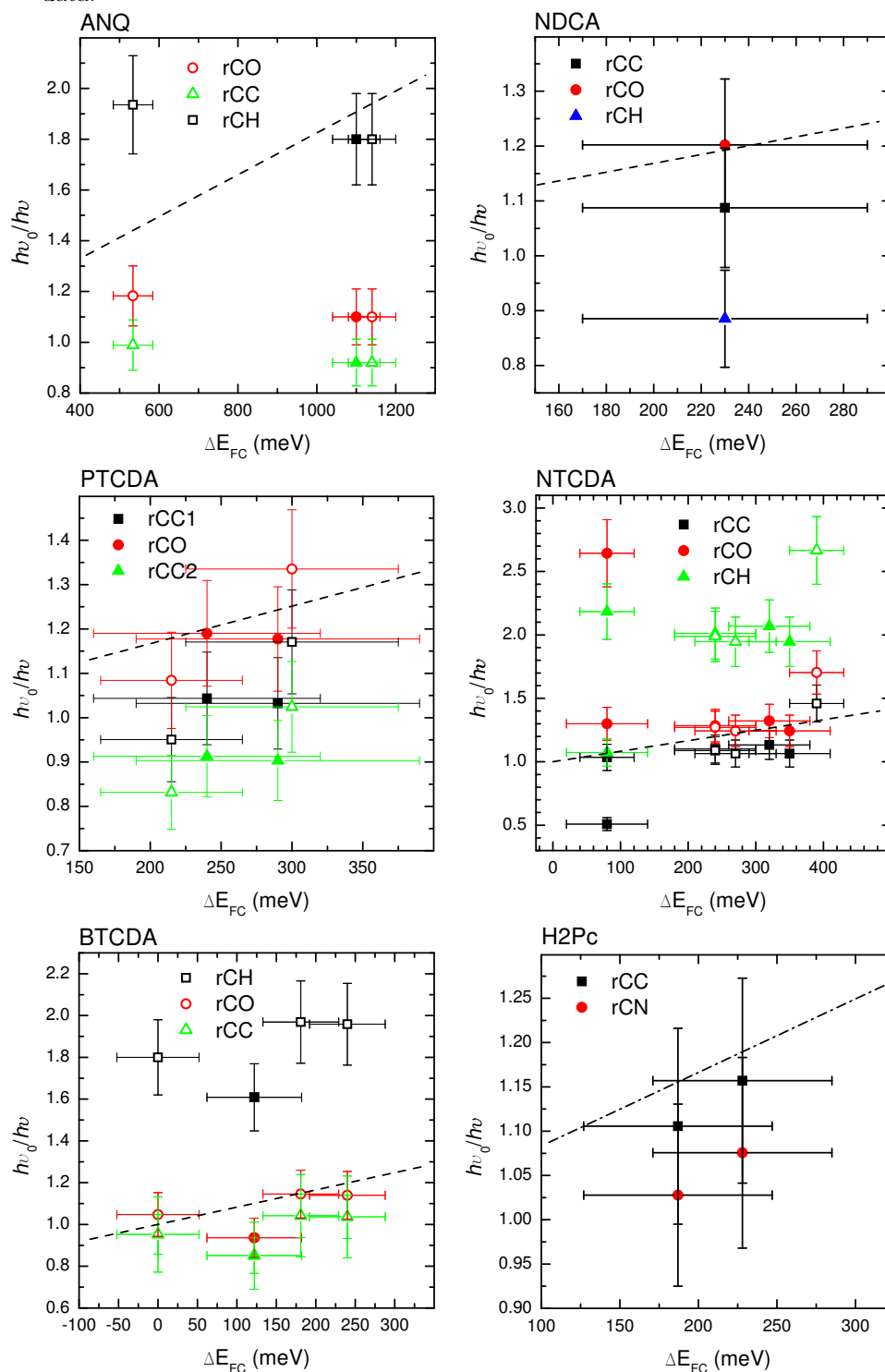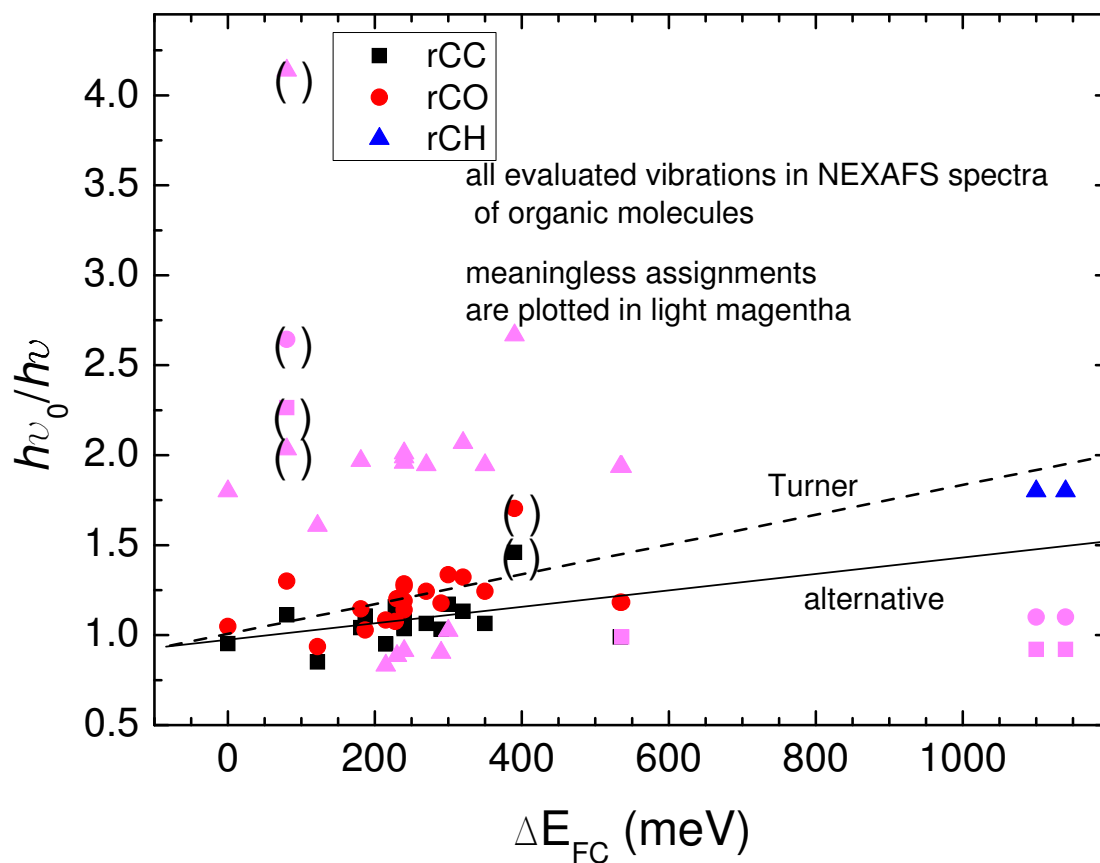
Figure 5.26: Ratio of vibronic energy in the ground– and excited state, plotted versus the Franck–Condon shift ΔE_{FC}. The dashed line represents equation (2.9), the solid line is a proposed alternative. Symbols plotted in light grey represent datapoints for which it is evident that the respective ground state vibration is not assigned correctly.

Table 5.7: Overview over moste relevant vibrations that have been analysed by FC fitting.

molecule	$h\nu$ [eV]	ΔE_{FC} [eV]	GS normal modes C=O, C–C, C–H
BTCDA C–K GP α	0.19	0.18	
	0.21	2E-4	
BTCDA C–K GP γ	0.19	0.24	0.22, 0.20, 0.38 [a]
BTCDA C–K SS γ	0.24	0.12	
NTCDA C–K GP γ	0.18	0.24	
NTCDA C–K GP γ	0.19	0.27	0.23, 0.20, 0.36 [j]
PTCDA C–K SS γ	0.16	0.30	
	0.20	0.22	
PTCDA C–K SS γ [i]	0.186	0.29	0.22, 0.19, 0.17 [c]
	0.184	0.24	
NDCA C–K SS γ [i]	0.183	0.23	0.22, 0.19, 0.17 [e]
ANQ O–K GP [f]	0.186	0.534	
ANQ O–K GP [g]	0.200	1.140	0.22, 0.18, 0.36 [b]
ANQ O–K SS [g]	0.200	1.100	
H_2–Pc N–K [h]	0.172	0.228	0.199 (C=C), 0.185 (C=N)[d]
	0.180	0.187	

[a]Ref. [87], [b]Ref. [118], [c]Ref. [111]
[d]Ref. [119], [e]Ref. [120], [f]Ref. [16]
[g]Ref. [117], [h]Ref. [121], [i]Ref. [93]
[j]Ref.

Concluding Discussion 6

The different effects of solid state formation that have been observed in the NEXAFS gas phase and solid state spectra are all in the range of a few hundred meV. The largest shift of 0.31 eV has been found for the C–K edge feature α of PTCDA. Such differential shifts of individual peaks have been proven for all compounds investigated in this work. However, the individual spectra of the different atomic species within one compound do not necessarily show the same behaviour, as was observed amongst others for the C–K and O–K edge of NTCDA. Also for the shape of the features and the intensity distribution, differences were evident for all molecules, again with large differences for the individual absorption edges. Among the family of the dianhydrides all these solid state effects are similar and getting more pronounced with increasing size of the molecule. For the more weakly interacting molecule Alq$_3$ however, a completely different behaviour has been found. The shape of the features is preserved at all edges to a large extent and the observed peak–shifts are restricted to one unoccupied orbital, the LEMO+2.

Different theoretical models have been proposed to explain the observed changes in NEXAFS spectra of gaseous and condensed molecules. The effect of an altered geometry of the molecule in the crystal structure is, together with the reduced symmetry compared to the gas phase molecule, the most basic one. The potential effect on the NEXAFS signature has been shown by calculations for the free and distorted molecule. Only for calculations using a non–physically short C–H bond lengths, the size of the resulting changes compares with the experimental findings. The other proposed models are based on a coupling of orbitals or wave functions of neighbouring molecules in the ground and the electronically excited state. Especially for the differential changes, the interaction in the excited state is favourable.

As long as just one compound is considered separately, surely one model can be found that will explain the observed differences at least in a qualitative way. In case of NTCDA for example, a $\pi - \pi$–overlap of the aromatic system can explain most changes observed upon solid state formation satisfactorily well. A more comprehensive investigation of a series of molecules, however, reveals severe discrepancies if this model is transferred to another system. In the line of the dianhydrides for example, the model suited for NTCDA was not compatible with the crystal configuration of the smaller BTCDA. Furthermore, when considering similar

sets of data simultaneously, none of these models alone will yield consistent results for the individual compounds. The interaction between the molecules is just much more complicated since different interaction effects act together. Consequently, also a joint interpretation including several phenomena is needed for a comprehensive explanation of the experimental findings.

Considering the available optical spectroscopic data of organic compounds in various phases, the investigations by means of NEXAFS spectroscopy have given additional, valuable information. For strongly interacting molecules as the dian-hydrides, as well as for the more weakly interacting Alq_3, the NEXAFS results are in good accordance with the results of optical spectroscopy with respect to the size of the changes observed upon condensation. Of course, the results may be compared qualitatively only, i.e. by a crude classification as interacting and non–interacting compounds. Due to its chemical selectively, NEXAFS yields more detailed information compared to optical spectroscopy. In the case of Alq_3, the principal part of the interaction could be ascribed to the LEMO+2 orbital. In addition, it has been shown that the interaction is more pronounced for the N– and C– atoms.

This more detailed information of course also bears a disadvantage. NEXAFS is a quite complex spectroscopic method since the observed changes may be assigned to the initial or final state and core or unoccupied orbital effects, respectively. Therefore, help from the theoretical side is coercively needed in order to better understand and interpret the experimental findings. Embedding the excitonic coupling into the calculations of NEXAFS spectra can be considered as a first step. Accounting for the detailed effects of the next neighbours, and incorporating Kasha's 'van–der–Waals' term mark the next steps.

From a experimental point of view, other electron spectroscopic methods may seem helpful for a better understanding of the changes in the NEXAFS spectra. However, in case of UPS or XPS, the situation is different due to the ionic final state and the resulting polarisation effects.

In general, more data of gas phase and respective solid phase NEXAFS is needed, also in order to further extend the collection of vibronic data. Even more important is an additional *systematic* experiment of, e.g., the corresponding diimides to the already examined dianhydrides. Such an investigation will yield valuable information on the role of the functional group in intermolecular interaction.

Acronyms

A

AES	Auger electron spectroscopy
Alq$_3$	tris (8–quinolinol) aluminum
AML	annealed multilayer
AN	angled neighbour
ANQ	acenaphthene quinone
BTCDA	benzene–tetracarboxylic acid dianhydride
CI	configuration interaction
CML	cold multilayer
DFT	density functional theory
EELS	electron energy loss spectroscopy
FC	Franck–Condon
FTIR	fourier transform infrared
FWHM	full width at half maximum
HOMO	highest occupied molecular orbital
HREELS	high resolution electron energy loss spectroscopy
IPES	inverse photoelectron spectroscopy
IVO	improved virtual orbital
LEMO	lowest excited molecular orbital
ML	monolayer

NDCI	naphthalene–dicarboxylic acid imide
NEXAFS	near–edge x–ray absorption fine structure
NTCDA	1,4,5,8–naphthalene–tetracarboxylic acid dianhydride
OLED	organic light emitting diode
OMBD	organic molecular beam deposition
OMC	organic molecular crystal
OPVD	organic photovoltaic device
PES	photoelectron spectroscopy
PEY	partial electron yield
PID	proportional–integral–differential
PL	photo luminescense
PMDA	pyromellitic dianhydride
PTCDA	3,4,9,10–perylene–tetracarboxylic acid dianhydride
PTCDI	3,4,9,10–perylene–tetracarboxylic acid diimide
SN	stacked neighbour
SNR	signal to noise ratio
STXM	scanning transmission X–ray microscopy
TEY	total (photo) electron yield
TIY	total ion yield
UPS	ultraviolett photoelectron spectroscopy
XPS	x–ray photoelectron spectroscopy
XRD	x–ray diffraction

B Additional Results

B.1 NDCI

In the first gas phase NEXAFS investigations, naphthalene–dicarboxylic acid imide (NDCI) has been measured at the gas phase beamline ELETTRA. The molecule was evaporated at a temperature of 400K. Figure B.1 depicts the gas phase (top) and solid state spectra (bottom) of NDCI a the C–K edge. The energy scale has been calibrated to the CO_2 C 1s→π^* resonance in case of the gas phase and to the Ag^{3d} substrate lines in case of the solid state spectrum. However, the resulting overall red–shift in the range of $0.5\,eV$ is very large compared to the hitherto observed shifts. Therefore the calibration should be verified by additional measurements. Meanwhile, relative shifts in energy will be considered.

The well resolved fine structure of features one, three, and four indicates vibronic progressions. If theoretical calculation yield only few electronic transitions for these features, which are good candidates for a FC fit analysis. The signature of the fine structure in all features, except for the first one, is getting more pronounced upon solid state formation. Similar observations have been made for NTCDA.

The discrepancies between energy shifts of the onsets and the peak maxima indicate a significant change in the subjacent vibronic fine structure. Interesting is also the change in intensity observed for the first and third feature. While an decrease of intensity for the first feature is also observed in NTCDA and PTCDA, the third feature is hardly affected in the dianhydrides. This indicates that the imide functional group is more involved in the solid state formation as the anhydride functional group.
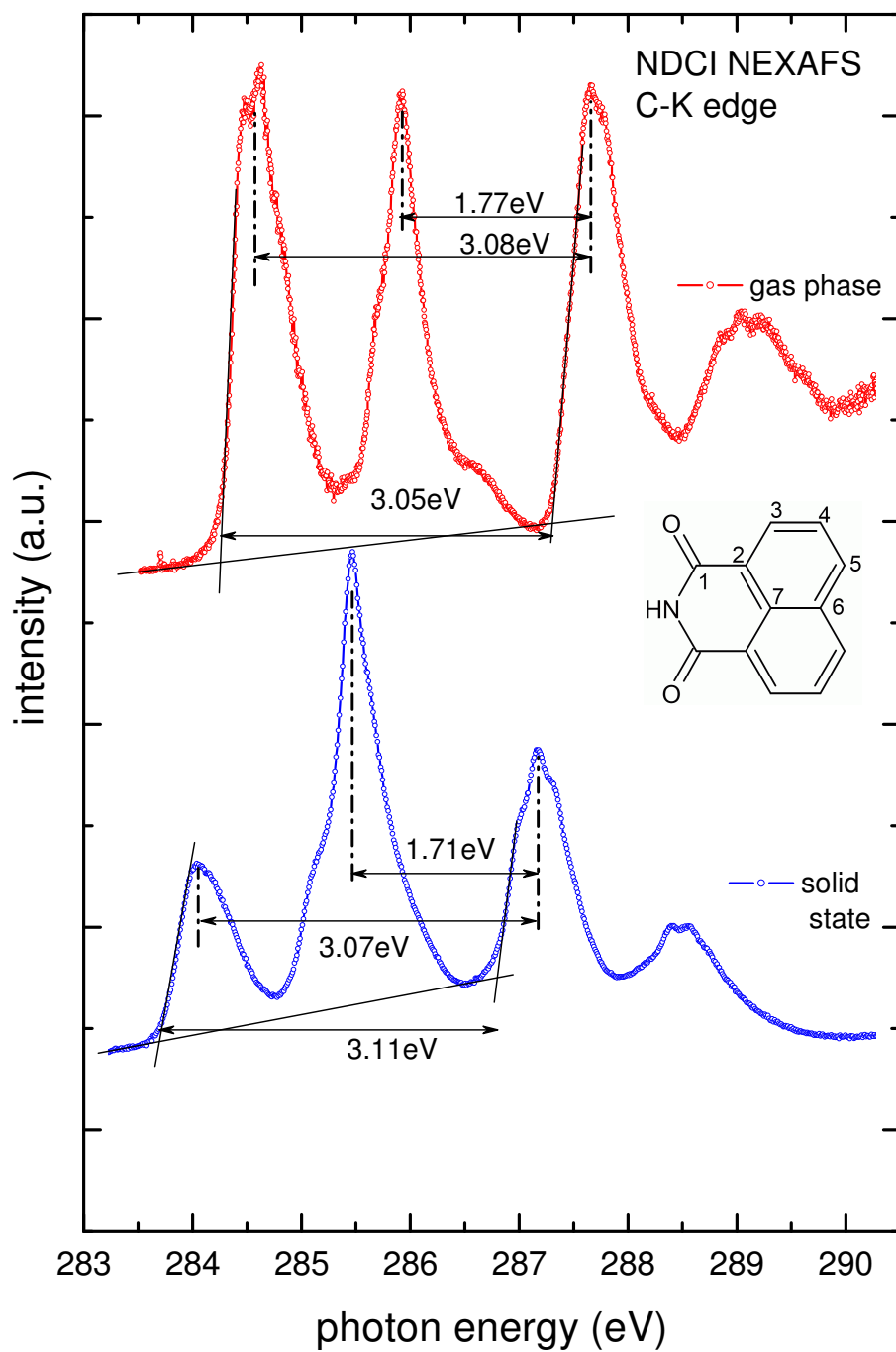
Figure B.1: C–K NEXAFS spectra of NDCI in the gas phase (top) and in the solid state (bottom).

B.2 FC–fit results

B.3 BTCDA

Feature α

Table B.1: Fit parameters of the FC analysis of BTCDA feature α based on the C_2 and C_3 1s→LEMO transition. Free parameters are set in italics. Intensity (int), shift (sh), scale (sc), and anharmonicity (ξ) are given in arbitrary units, the other parameters in eV.

FC fit label	pos	int	Γ_G	Γ_L	hν	sc	sh	ξ
solid state from gas phase: splitting								
PEY04	*284.59*	*1.152*	*0.448*	0.112	*0.142*	*0.384*	*2.8*	*0.03*
	285.14	*0.094*	*0.470*	0.112	*0.210*	0.499	0.002	0.000

Feature γ

Table B.2: Fit parameters of the FC analysis of BTCDA feature γ based on the C_1 1s→LEMO transition. Free parameters are set in italics. Intensity (int), shift (sh), scale (sc), and anharmonicity (ξ) are given in arbitrary units, the other parameters in eV.

FC fit label	pos	int	Γ_G	Γ_L	hν	sc	sh	ξ
gas phase								
GP14	*287.52*	*2.589*	*0.151*	*0.065*	*0.191*	*0.971*	*1.875*	*0.010*
GP32	*287.52*	*2.402*	*0.142*[1]	*0.065*	*0.193*	*0.951*	*1.831*	0.000
from gas phase: gaussian broadening								
PEY24	*287.62*	*1.463*	*0.191*	0.065	0.191	0.971	1.875	0.010
PEY80	*287.62*	*1.454*	*0.199*[2]	0.065	0.193	0.951	1.831	0.000
from gas phase: splitting into components								
PEY21	*287.56*	*0.599*	0.151	0.065	0.191	0.971	1.875	0.010
	287.66	*1.126*	0.151	0.065	0.191	0.971	1.875	0.010

---

[1]Γ'_G of high energy side is *0.196* eV.
[2]Γ'_G of high energy side is *0.199* eV.

BTCDA FC parameters feature γ. (continued)

FC fit label	pos	int	Γ_G	Γ_L	hν	sc	sh	ξ
PEY22	*287.53*	*0.548*	0.151	0.065	0.191	0.971	1.875	0.010
	287.64	*1.301*	0.151	0.065	0.191	0.971	1.875	0.010
	287.93	*0.366*	0.151	0.065	0.191	0.971	1.875	0.010
PEY23	*287.52*	*0.547*	0.151	0.065	0.191	0.971	1.875	0.010
	287.63	*0.648*	0.151	0.065	0.191	0.971	1.875	0.010
	287.63	*0.653*	0.151	0.065	0.191	0.971	1.875	0.010
	287.92	*0.364*	0.151	0.065	0.191	0.971	1.875	0.010
from scratch: equidistant components								
PEY42	*287.63*	*1.572*	*0.193*	0.065	*0.223*	*1.012*	*1.738*	*0.042*
PEY81	*287.63*	*1.359*	*0.194*[3]	*0.065*	*0.240*	*0.940*	*1.675*	*0.035*
PEY61	*287.60*	*0.995*	*0.162*	0.065	*0.245*	*0.842*	*1.712*	*0.000*
	287.74	*0.775*	0.162	0.065	0.245	0.842	1.712	0.000
PEY63	*287.63*	*0.863*	*0.195*	0.065	*0.235*	*0.647*	*1.694*	*0.044*
	287.82	*0.297*	0.195	0.065	0.235	0.647	1.694	0.044
	288.01	*0.415*	0.195	0.065	0.235	0.647	1.694	0.044
PEY64	*287.62*	*0.797*	*0.183*	0.065	*0.237*	*0.659*	*1.670*	*0.050*
	287.75	*0.259*	0.183	0.065	0.237	0.659	1.670	0.050
	287.89	*0.223*	0.183	0.065	0.237	0.659	1.670	0.050
	288.02	*0.352*	0.183	0.065	0.237	0.659	1.670	0.050
from scratch: two independent vibrations								
PEY45	*287.62*	*1.065*	*0.185*	*0.065*	*0.208*	*0.771*	*1.877*	*0.000*
	287.67	*0.509*	*0.200*	*0.065*	*0.322*	*0.649*	*2.487*	*0.060*

---

[3]Γ'_G of high energy side is *0.266* eV.

Table B.3: Additional BTCDA FC fit results for feature γ.
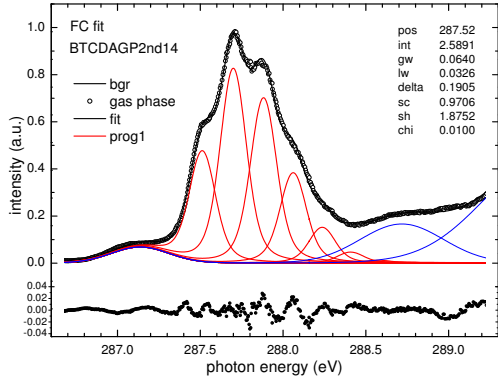
GP14: gas phase from scratch, 8 parameters
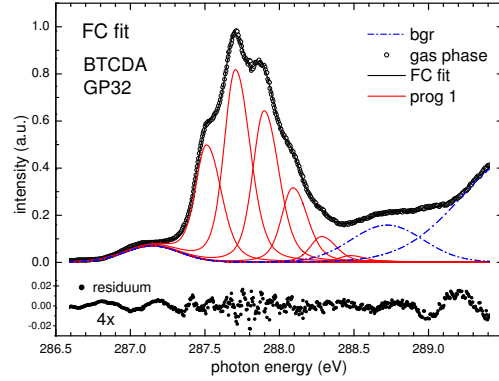
GP32: gas phase from scratch, asymmetric line shape, 8 parameters
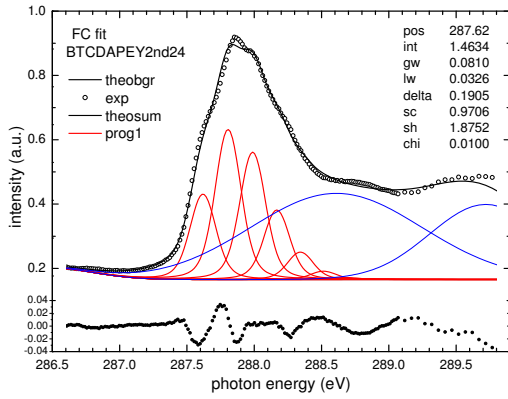
PEY24: solid state from gas phase, 3 parameters
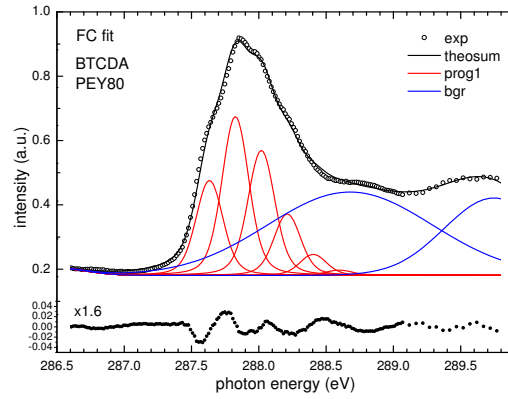
PEY80: solid state from gas phase, asymmetric line shape, 4 parameters
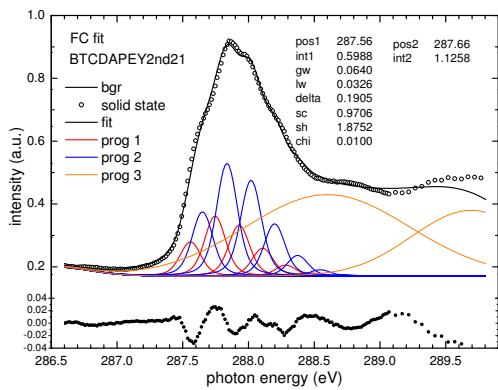
PEY21: solid state from gas phase, 2 components, 4 parameters
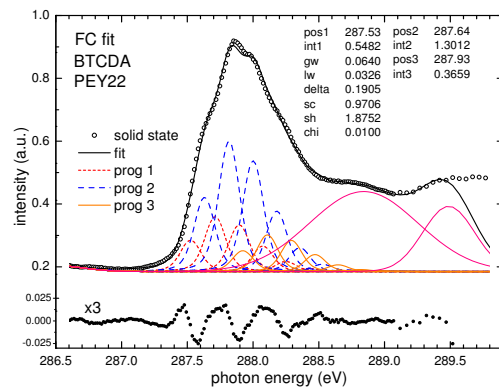
PEY22: solid state from gas phase, 3 components, 6 parameters

Table B.3: Additional BTCDA FC fit results for feature γ. (continued)
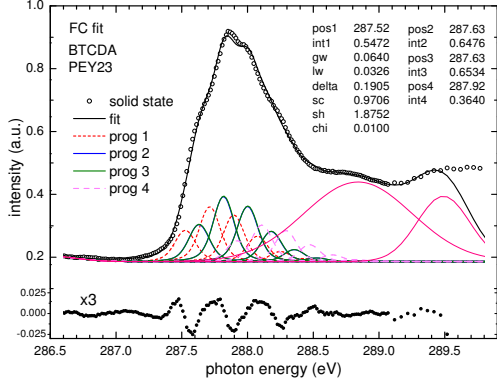
PEY23: solid state from gas phase, 4 components, 8 parameters
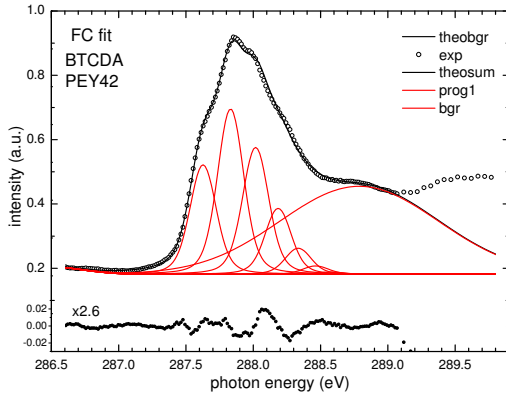
PEY42: solid state from scratch, 7 parameters
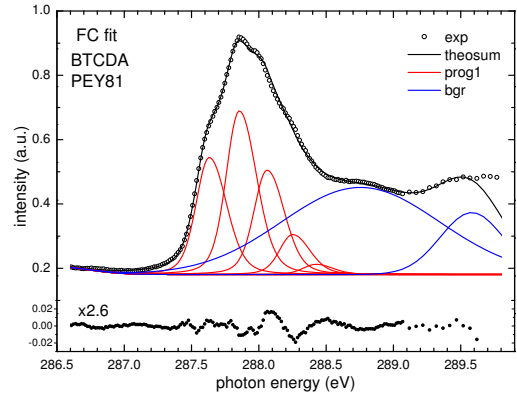
PEY81: solid state from scratch, asymmetric line shape, 8 parameters
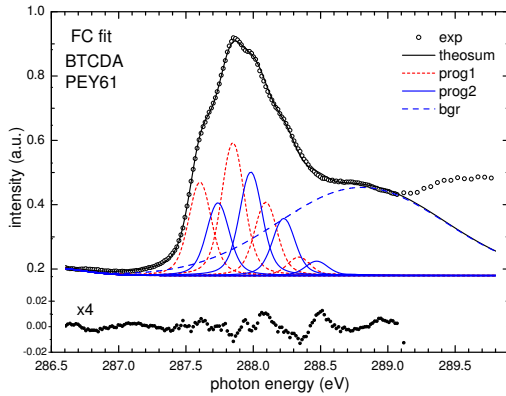
PEY61: solid state from scratch, 2 components, 9 parameters
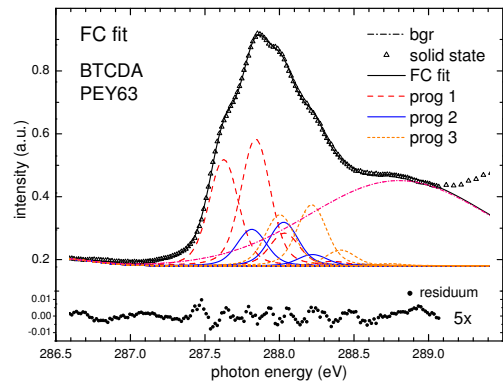
PEY63: solid state from scratch, 3 components, 10 parameters
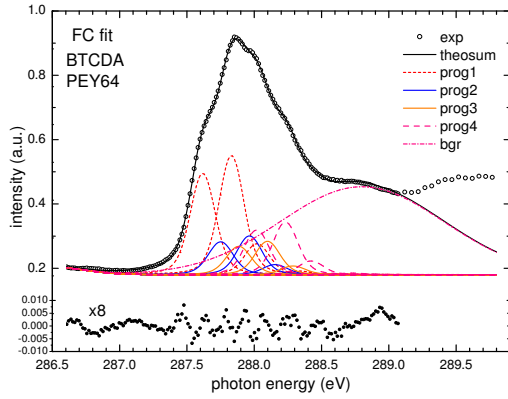
PEY64: solid state from scratch, 4 components, 11 parameters
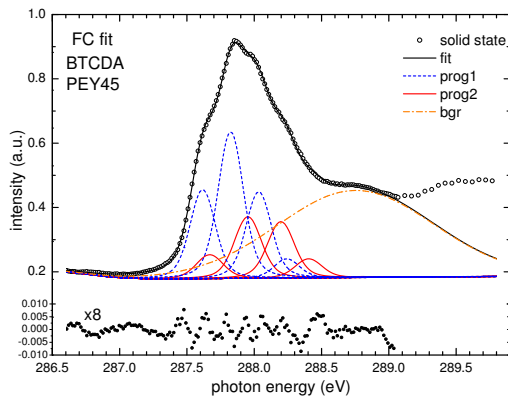
PEY45: solid state from scratch, 2 vibrations, 13 parameters

B.4 NTCDA

Table B.4: Comparison of the parameters derived from the FC fits of the NTCDA
C–K edge feature γ. Free parameters are set in *italics*. See text for details.

FC fit label	pos	int	Γ_G	Γ_L	δ	sc	sh	ξ
			GP to AML: shifted *sequentially*					
	287.71	*2.867*	0.166	0.078	*0.181*	*1.048*	*1.924*	0.000
GP09	*288.43*	*1.061*	0.166	0.078	*0.135*	*0.976*	*2.578*	0.000
	288.97	*0.989*	0.166	0.078	*0.185*	*1.084*	*1.923*	0.000
	287.66	*3.086*	0.137	0.078	0.181	1.048	1.924	0.000
AML203	*288.24*	*0.909*	0.137	0.078	0.135	0.976	2.578	0.000
	288.92	*0.956*	0.137	0.078	0.185	1.084	1.923	0.000
			GP to AML: shifted *simultaneously*					
	287.68	*2.710*	*0.172*	*0.077*	*0.181*	*1.007*	*1.962*	0.000
GP13	*288.36*	*0.860*	0.172	0.077	*0.128*	*0.871*	*2.719*	0.000
	288.91	*1.268*	0.172	0.077	*0.191*	*1.100*	*1.766*	0.000
	287.67	*2.920*	0.138	0.077	0.181	1.007	1.962	0.000
AML13	*288.23*	*0.801*	0.138	0.077	0.128	0.871	2.719	0.000
	288.90	*0.984*	0.138	0.077	0.191	1.100	1.766	0.000
			GP to AML: Rydberg quenching *simultaneously*					
	287.68	*2.867*	*0.161*	*0.072*	*0.179*	*1.004*	*1.971*	0.000
GP10	*288.58*	*0.545*	0.161	0.072	*0.171*	*0.710*	*1.970*	0.000
	288.34	*0.437*	0.161	0.072	*0.153*	*1.100*	*1.850*	0.000
	288.92	*1.334*	0.161	0.072	*0.186*	*1.100*	*1.804*	0.000
	287.67	*2.960*	*0.139*	0.072	0.179	1.004	1.971	0.000
AML10	288.34	*0.935*	0.139	0.072	0.153	1.100	1.850	0.000
	288.91	*0.885*	0.138	0.072	0.186	1.100	1.804	0.000
			leading edge of AML: *splitted[4] progressions*					
	287.64	*1.762*	*0.098*	*0.061*	*0.185*	*0.972*	*1.946*	0.000
AML08	*288.20*	*0.468*	0.098	0.061	*0.163*	*0.821*	*2.498*	0.000
	288.88	*0.582*	0.098	0.061	*0.185*	*1.059*	*1.718*	0.000

---

[4]Additional progressions are splitted by *85* meV with intensities of *1.085*, *0.468*, and *0.338*.

NTCDA FC fit parameters feature γ. (continued)

FC fit label	pos	int	Γ_G	Γ_L	δ	sc	sh	ξ
	leading edge of AML: *asymmetric line shape*							
	287.66	*1.837*	*0.111*[5]	*0.064*	*0.190*	*0.943*	*1.861*	0.000
AML02	*288.13*	*0.705*	0.111	*0.110*	*0.130*	*0.983*	*2.797*	*0.026*
	288.91	*0.691*	0.111	*0.110*	*0.193*	*1.080*	*1.666*	*0.023*
	287.66	*1.862*	*0.107*[6]	*0.071*	*0.190*	*0.937*	*1.879*	*0.000*
AML01	*288.12*	*0.787*	*0.134*	0.071	*0.131*	*0.993*	*2.799*	*0.022*
	288.91	*0.729*	0.134	0.071	*0.191*	*1.080*	*1.701*	*0.021*

[5]Γ'_G of high energy side is *0.246* eV.
[6]Γ'_G of high energy side is *0.234* eV.
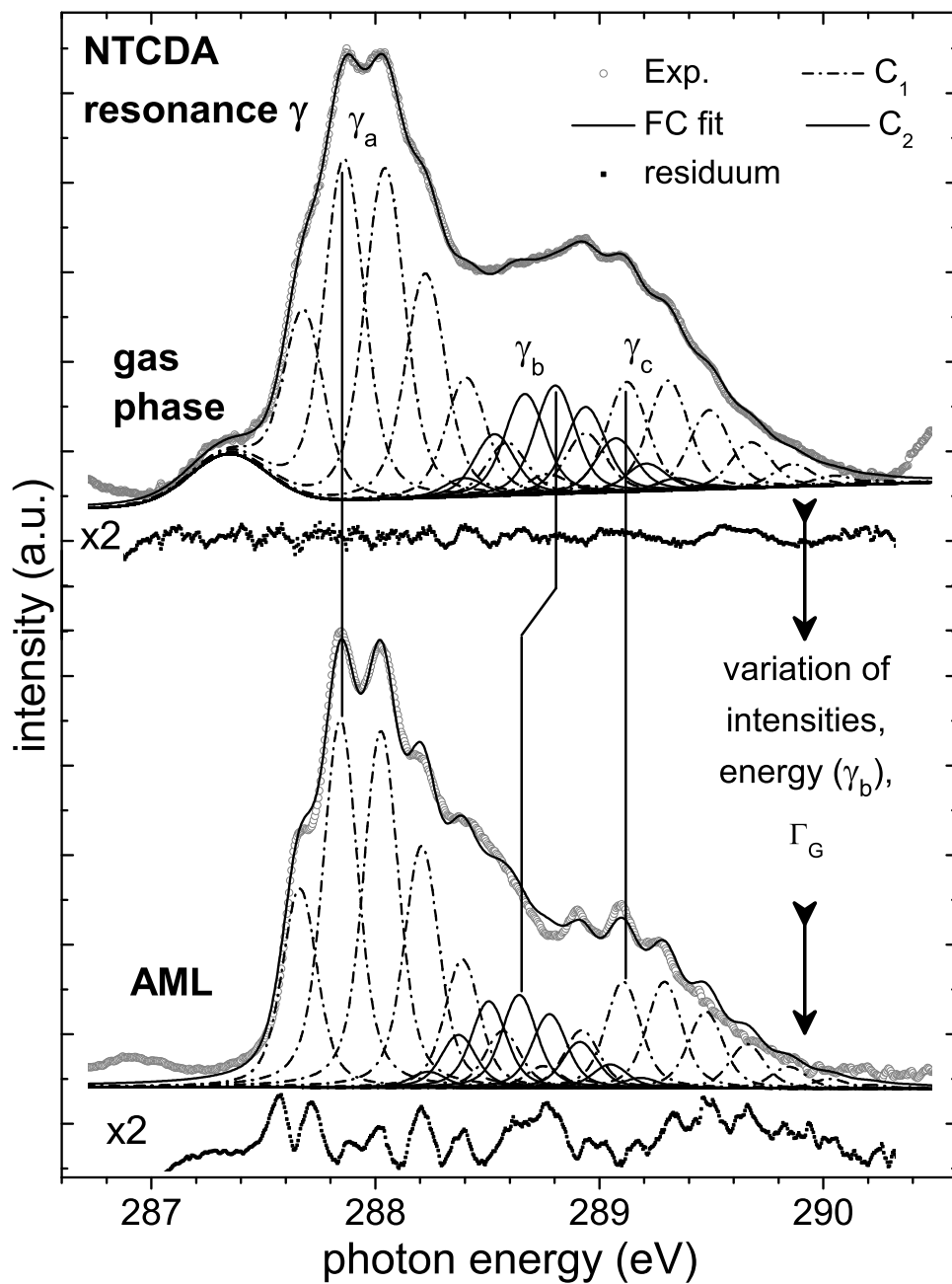
Figure B.2: FC fit analysis of feature γ of NTCDA C–K NEXAFS spectra, obtained from the gas phase (GP09, top) and AML data (AML203, bottom). For fit details see text and table B.4.

Molecular Orbitals

In this chapter the results of 'Z+1' Hartree–Fock calculations with a 6–31G(d,p) basis set are presented.

C.1 BTCDA Orbitals
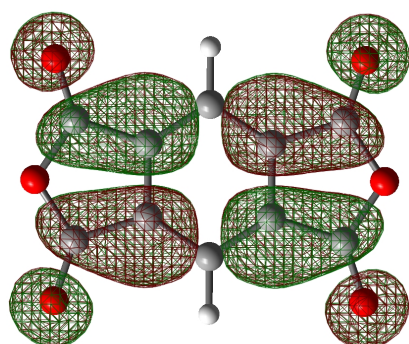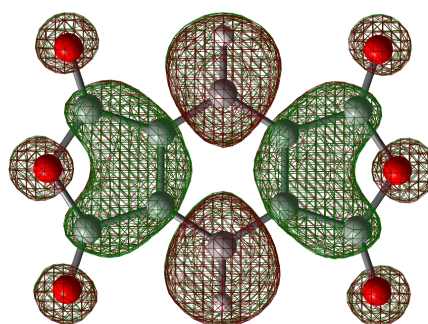
BTCDA LUMO   BTCDA LUMO+1
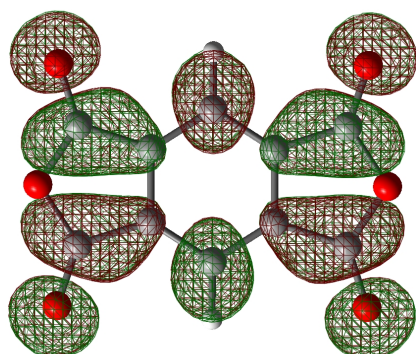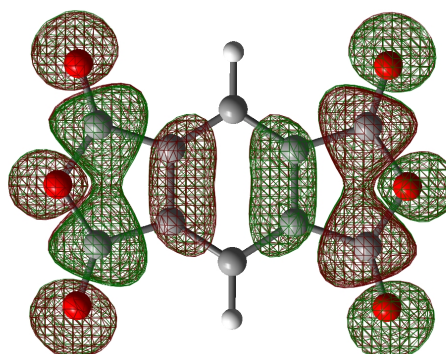
BTCDA LUMO+2   BTCDA LUMO+3

Figure C.1: Ground state orbitals of BTCDA.

BTCDA O$_A$ LEMO+1   BTCDA O$_A$ LEMO+3   BTCDA O$_A$ LEMO+4

BTCDA O$_A$ LEMO+6

BTCDA O$_B$ LEMO   BTCDA O$_B$ LEMO+1   BTCDA O$_B$ LEMO+2

BTCDA O$_B$ LEMO+3   BTCDA O$_B$ LEMO+4   BTCDA O$_B$ LEMO+5
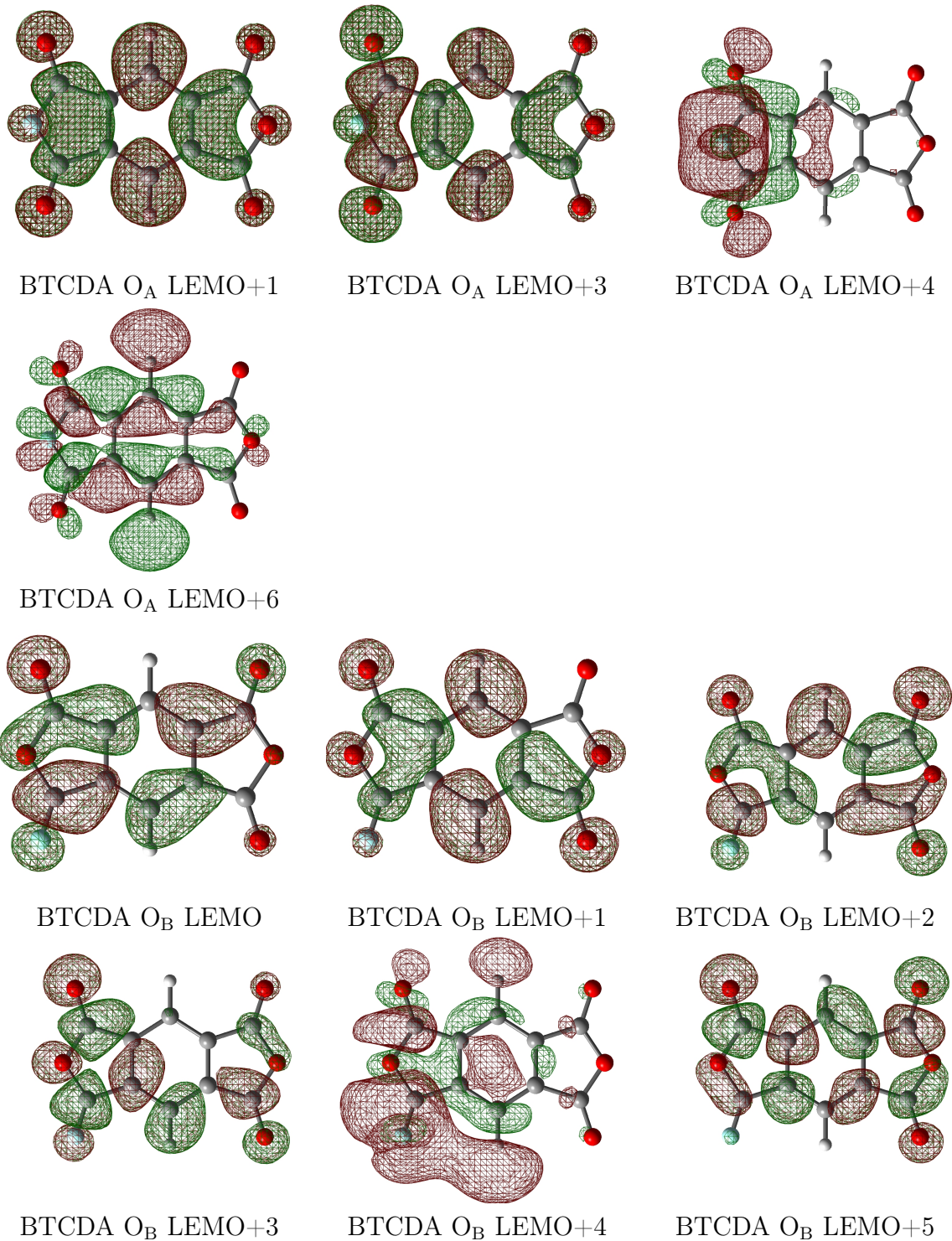
Figure C.2: Excited molecular orbitals of BTCDA oxygens, calculated in Z+1 approximation.

BTCDA C$_1$ LEMO

BTCDA C$_1$ LEMO+1

BTCDA C$_2$ LEMO

BTCDA C$_2$ LEMO+2

BTCDA C$_2$ LEMO+3

BTCDA C$_3$ LEMO

BTCDA C$_3$ LEMO+2

BTCDA C$_3$ LEMO+3
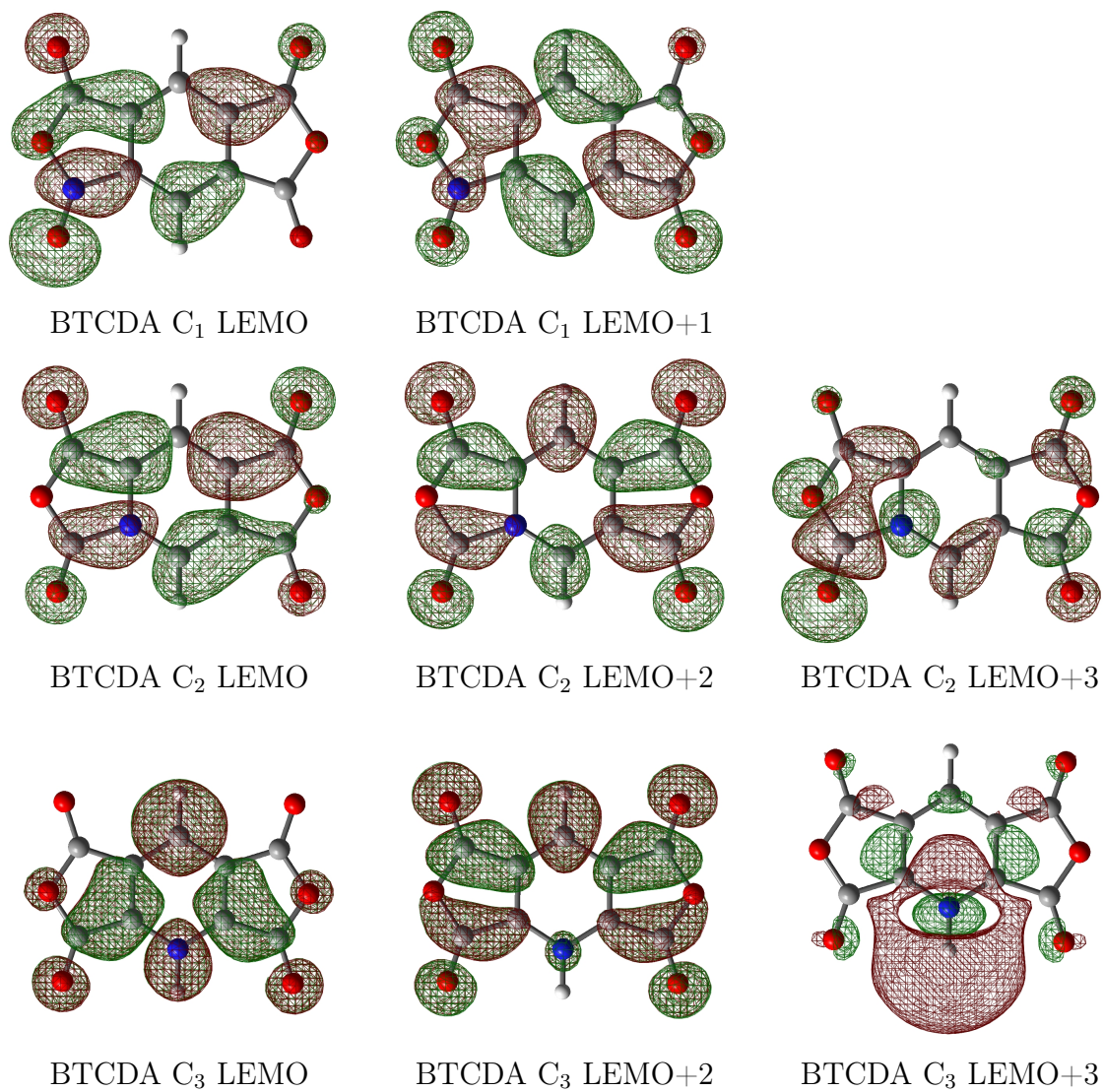
Figure C.3: Excited molecular orbitals of BTCDA carbons, calculated in Z+1 approximation.

C.2 NTCDA Orbitals

Table C.1: Molecular orbitals of NTCDA calculated in 'Z+1' approximation with a 631G(d,p) basis set.

GS LUMO

GS LUMO+1

GS LUMO+2

GS LUMO+3

GS LUMO+4

GS LUMO+5
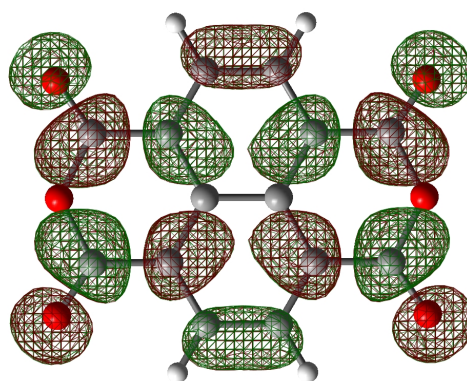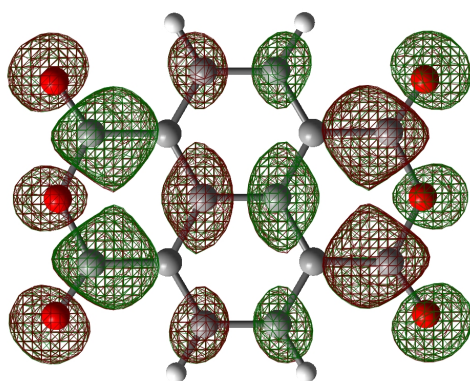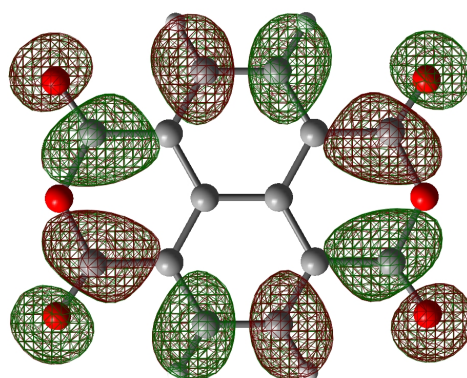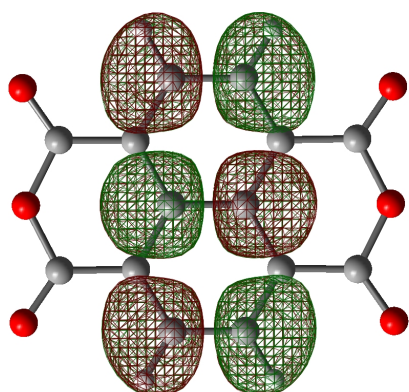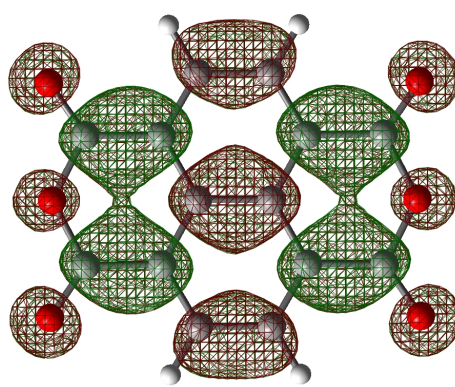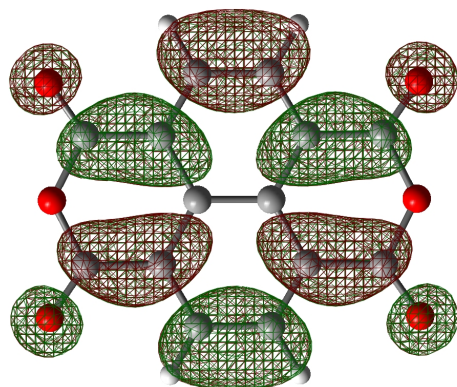
Table C.1: NTCDA molecular orbitals. (continued)

C$_1$ LEMO

C$_1$ LEMO+1

C$_2$ LEMO

C$_2$ LEMO+1

C$_2$ LEMO+4
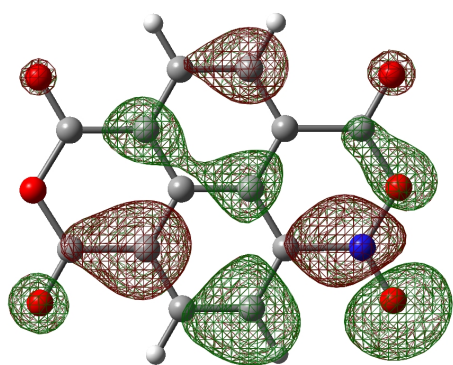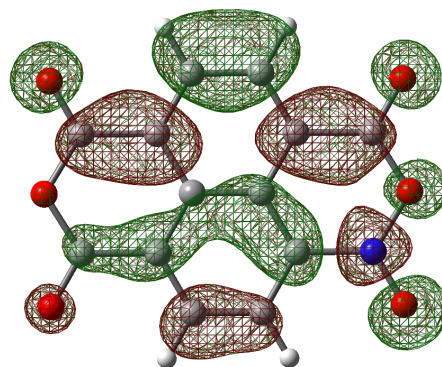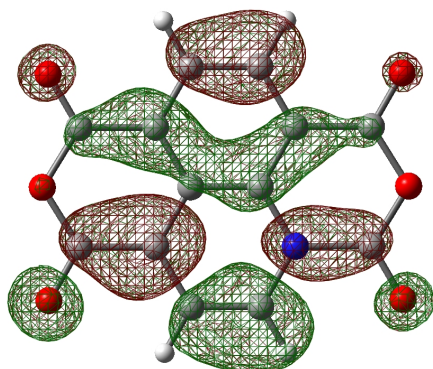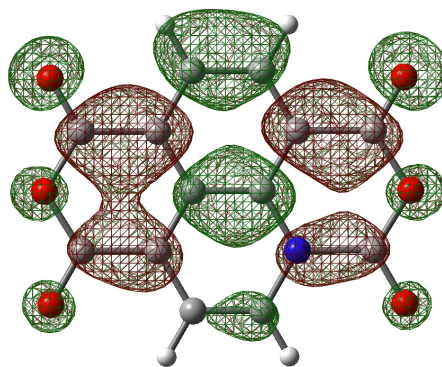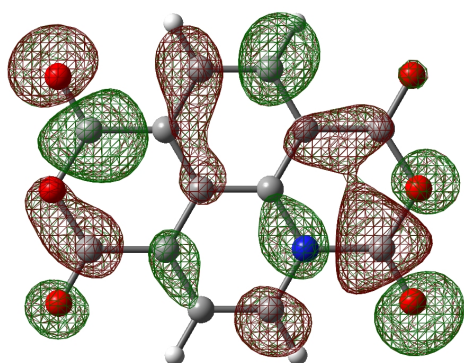
Table C.1: NTCDA molecular orbitals. (continued)

C$_3$ LEMO

C$_3$ LEMO+1

C$_3$ LEMO+3

C$_3$ LEMO+4

C$_4$ LEMO+1

C$_4$ LEMO+4
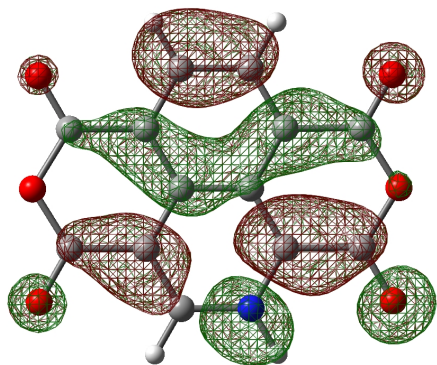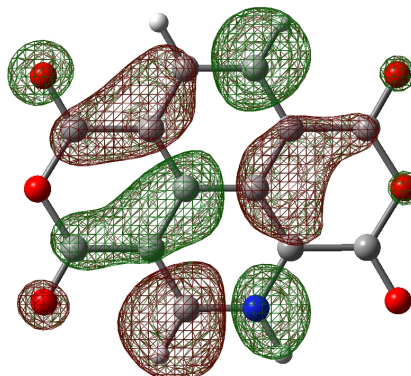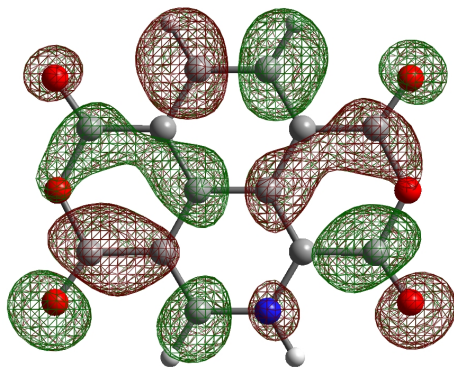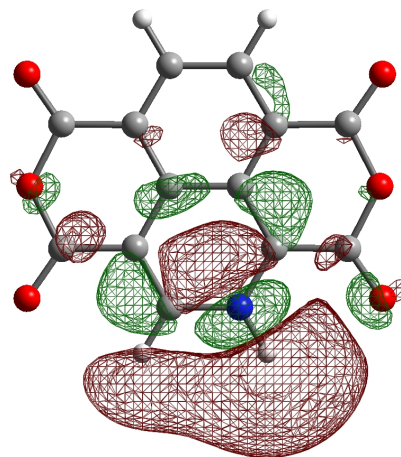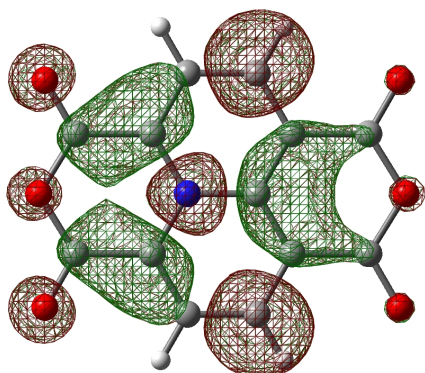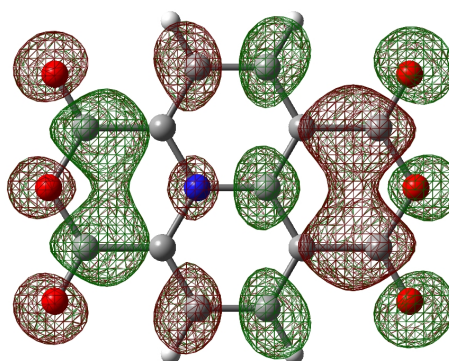
Table C.1: NTCDA molecular orbitals. (continued)
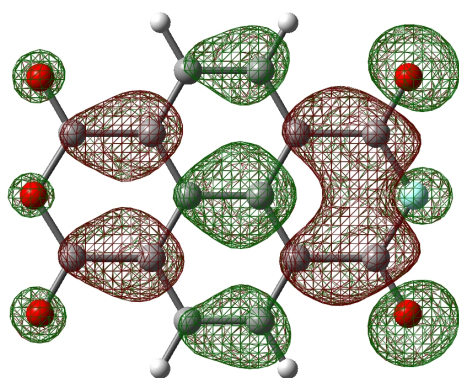
O$_A$ LEMO+1
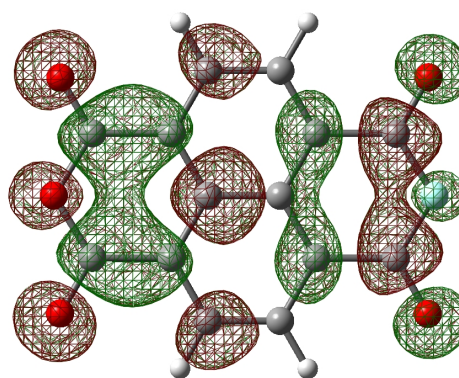
O$_A$ LEMO+4
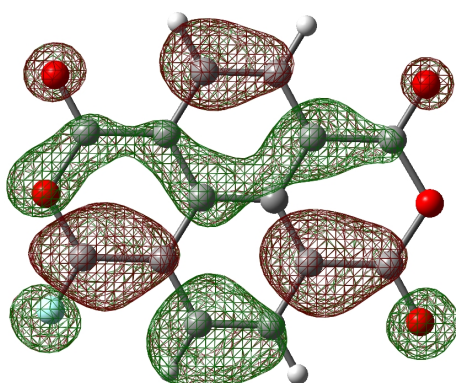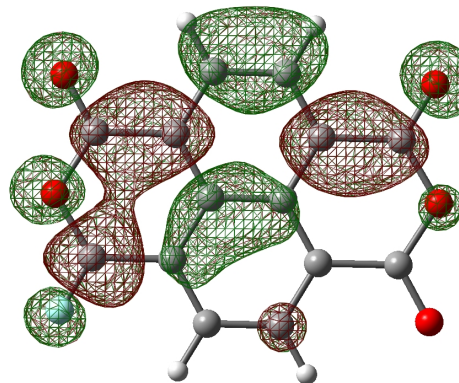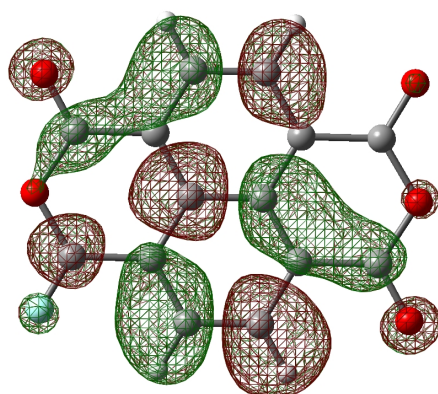
O$_B$ LEMO

O$_B$ LEMO+1

O$_B$ LEMO+2
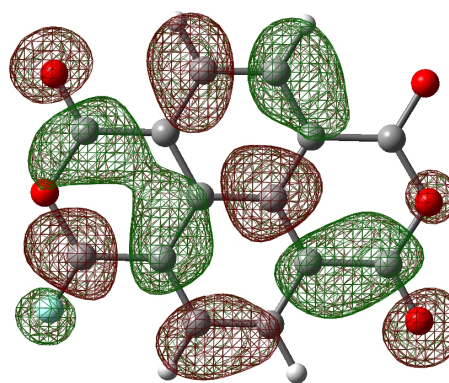
O$_B$ LEMO+3

Table C.1: NTCDA molecular orbitals. (continued)
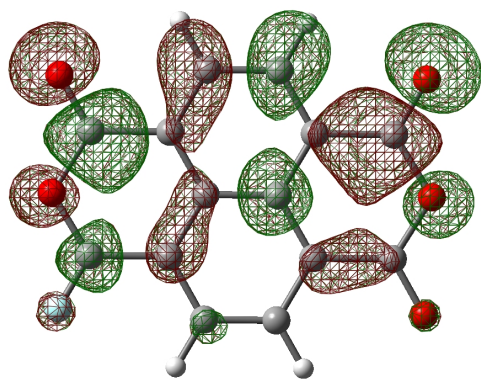
O$_B$ LEMO+4
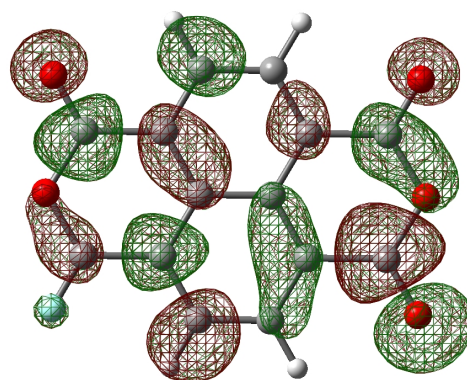
O$_B$ LEMO+5

C.3 PTCDA orbitals

Table C.2: Excited molecular orbitals of PTCDA, calculated in 'Z+1' approximation with a HF functional and a 631G(d,p) basis set.

| C_1 LEMO+1 | C_1 LEMO+2 | C_2 LEMO+1 | C_3 LEMO+1 |

| C_4 LEMO+1 | C_5 LEMO | C_5 LEMO+1 | C_5 LEMO+6 |

| C_6 LEMO+1 | C_6 LEMO+2 | C_7 LEMO+1 | C_7 LEMO+2 |
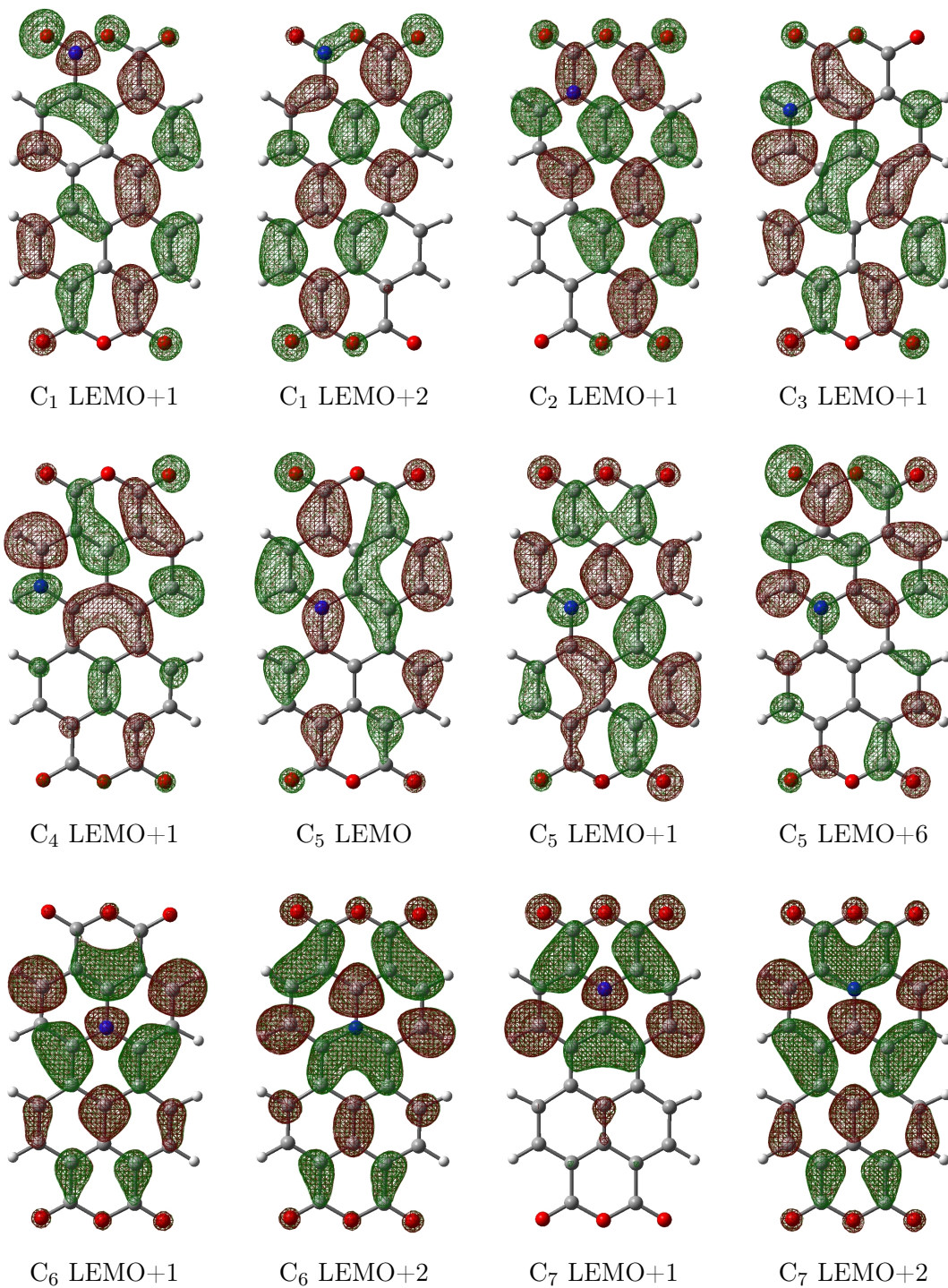
Table C.2: Excited molecular orbitals of PTCDA. (continued)
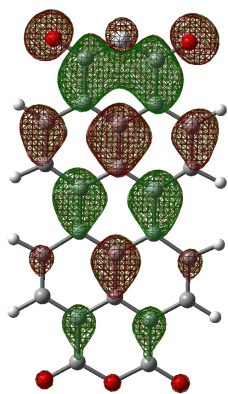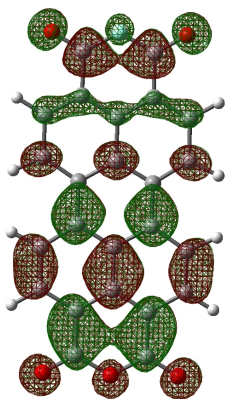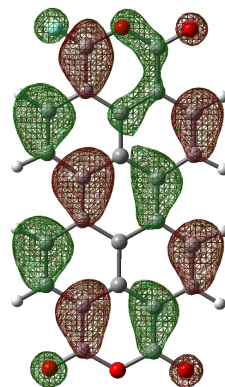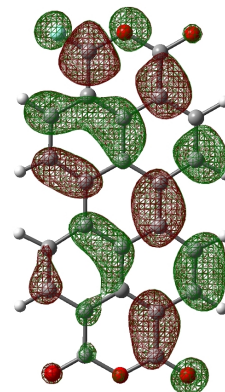
O$_A$ LEMO+1   O$_A$ LEMO+4   O$_B$ LEMO   O$_B$ LEMO+1
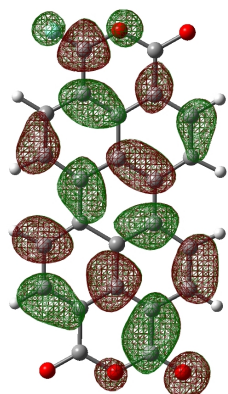
O$_B$ LEMO+4

Additional Calculations D

D.1 Additional Calculations

Coulomb Gauge

The Coulomb Gauge can be applied in case of the perturbed system as follows:

$$\hat{H}_0 = \frac{p^2}{2m} \text{ for perturbation use vector potential: } \hat{p} \to \hat{p} + \vec{e}\,\hat{A} \qquad (D.1)$$

$$p^2 = \hat{p}\hat{p} = \left(\hat{p} + \vec{e}\,\hat{A}\right)\left(\hat{p} + \vec{e}\,\hat{A}\right) = p^2 + \vec{e}\left(\hat{p}\hat{A} + \hat{A}\hat{p}\right) + A^2 \qquad (D.2)$$

using the Coulomb Gauge $\nabla\hat{A} = 0$ makes $\hat{p}$ and $\hat{A}$ commute: $\qquad (D.3)$

$$\hat{p}\hat{A}\Psi = -i\hbar\left(\hat{A}\nabla\Psi + \underbrace{\nabla\hat{A}}_{=0}\Psi\right) = \hat{A}\hat{p}\Psi \qquad (D.4)$$

D.2 Z+1 calculations for NTCDA

D.2.1 Effect of nearest neighbours

For NTCDA, Z+1 calculations have been performed to investigate the influence of molecular geometry and the nearest neighbours in the crystal. Figure D.1 shows the results for NTCDA in the optimised gas phase geometry (left) and in the geometry as found in the crystal [89]. The C–H bond length has been set to 1.803Å. As can be seen upon close inspection, already these small changes in geometry cause visible effects on the transition energies. Compared to the experimental results however, these shifts are still too small.

Introducing the next neighbours, additional, though small, effects are observed, as is depicted in figure D.2.
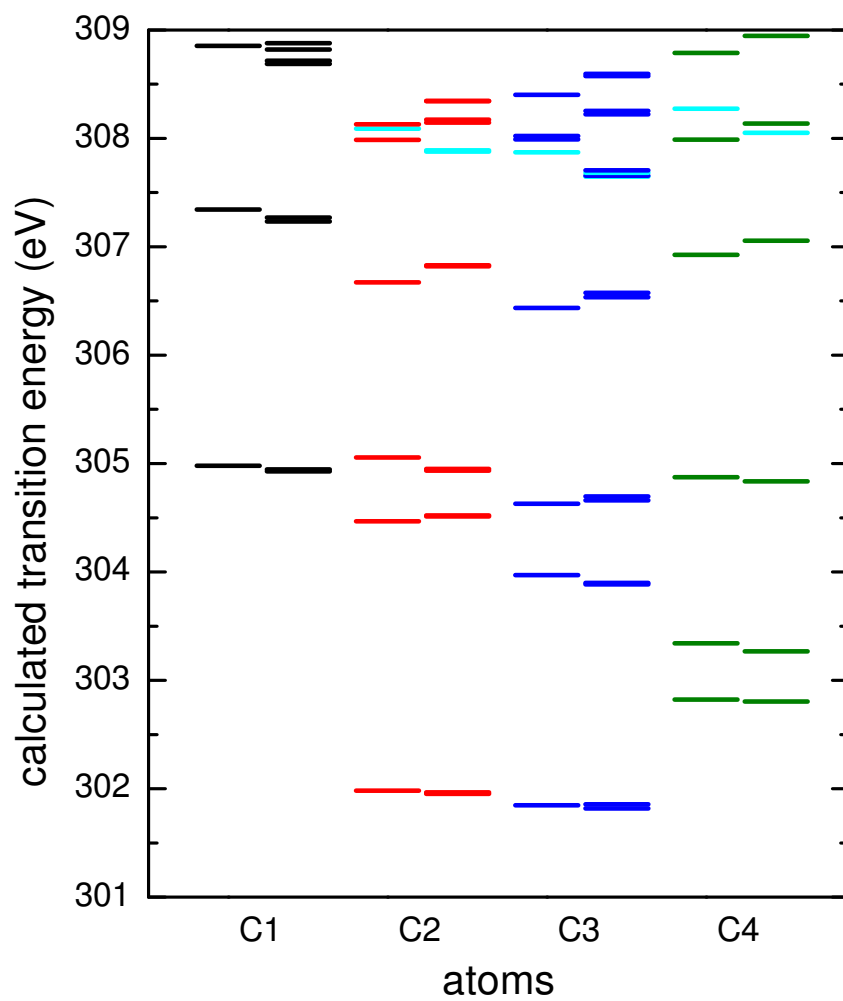
Figure D.1: NTCDA Z+1 calculations for a single molecule in its gas phase and crystal geometry. Plotted are all transition levels, also those that are not observed experimentally.
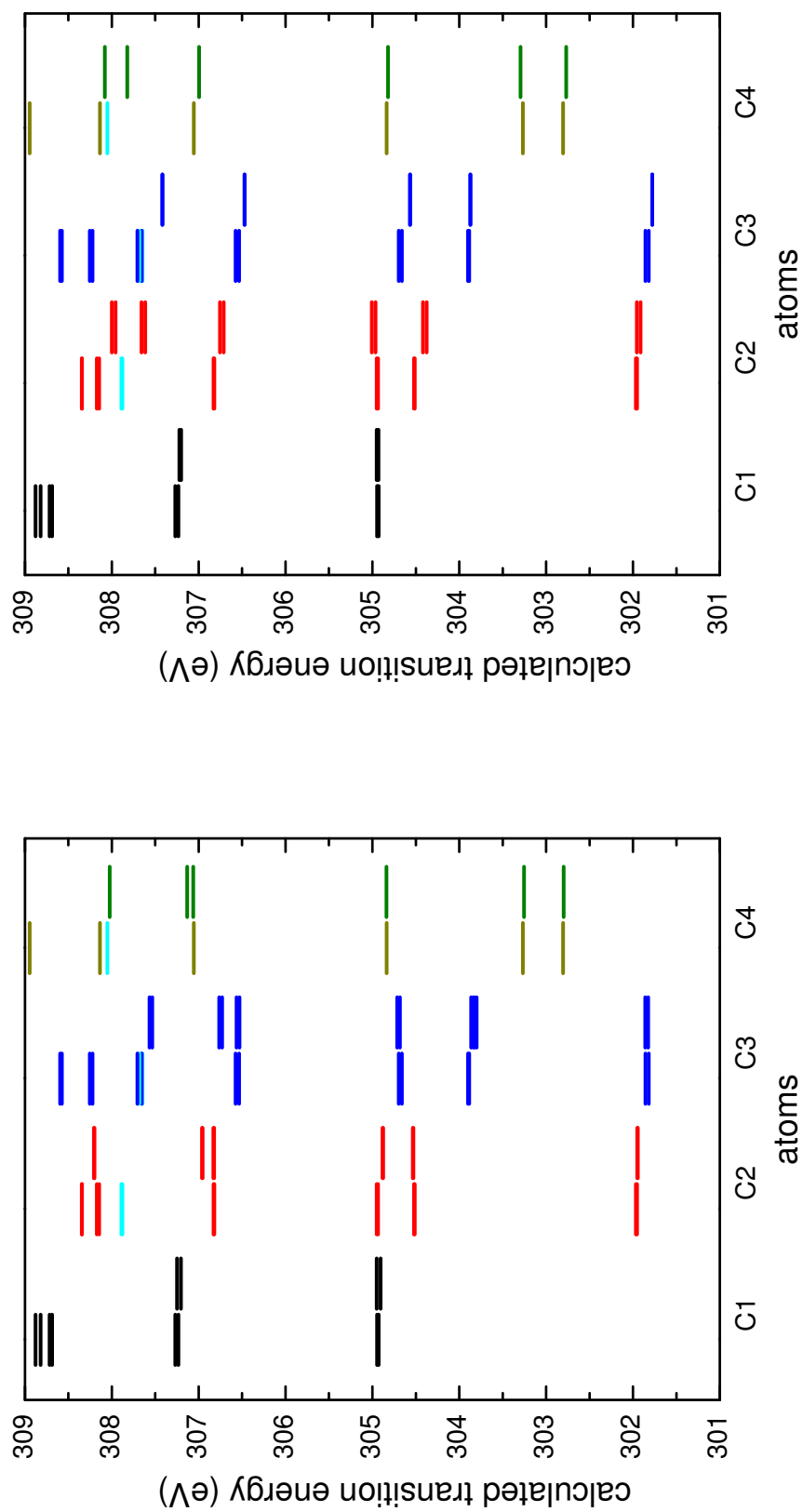
Figure D.2: Influence of angled next neighbours (left plot) and stacked next neighbours (right plot) on a NTCDA molecule in its crystal geometry (left levels). Plotted are all transition levels, also those that are not observed experimentally.

D.2.2 Dependence on C–H bond–length

The influence of the molecular structure on the transition energies can be seen nicely by the dependency on the C–H bond length.

Thermal motion and positively polarised H atoms cause XRD studies to yield too short C–H bond lengths [114, 115]. For nearly all molecules investigated in this work, literature states C–H bond lengths smaller than 1Å [80, 89, 107]. The average C–H distance determined by neutron scattering for $C_{aromatic}$–H, however, is 1.083(11)Å [116, 122]. Optimisation of the molecular geometry yields similar values.

For the dianhydrides, calculations using the short, *wrong* C–H bond lengths have been performed. As can be seen in figures D.3 and D.4 this yields significant shifts in transition energy not only for the directly connected C–atoms, but also for the other carbon and also oxygen atoms. This is caused by a general increase of the 1s core levels which in turn causes the transition energies to decrease. These shifts are in the same order of magnitude as the experimentally observed shifts.
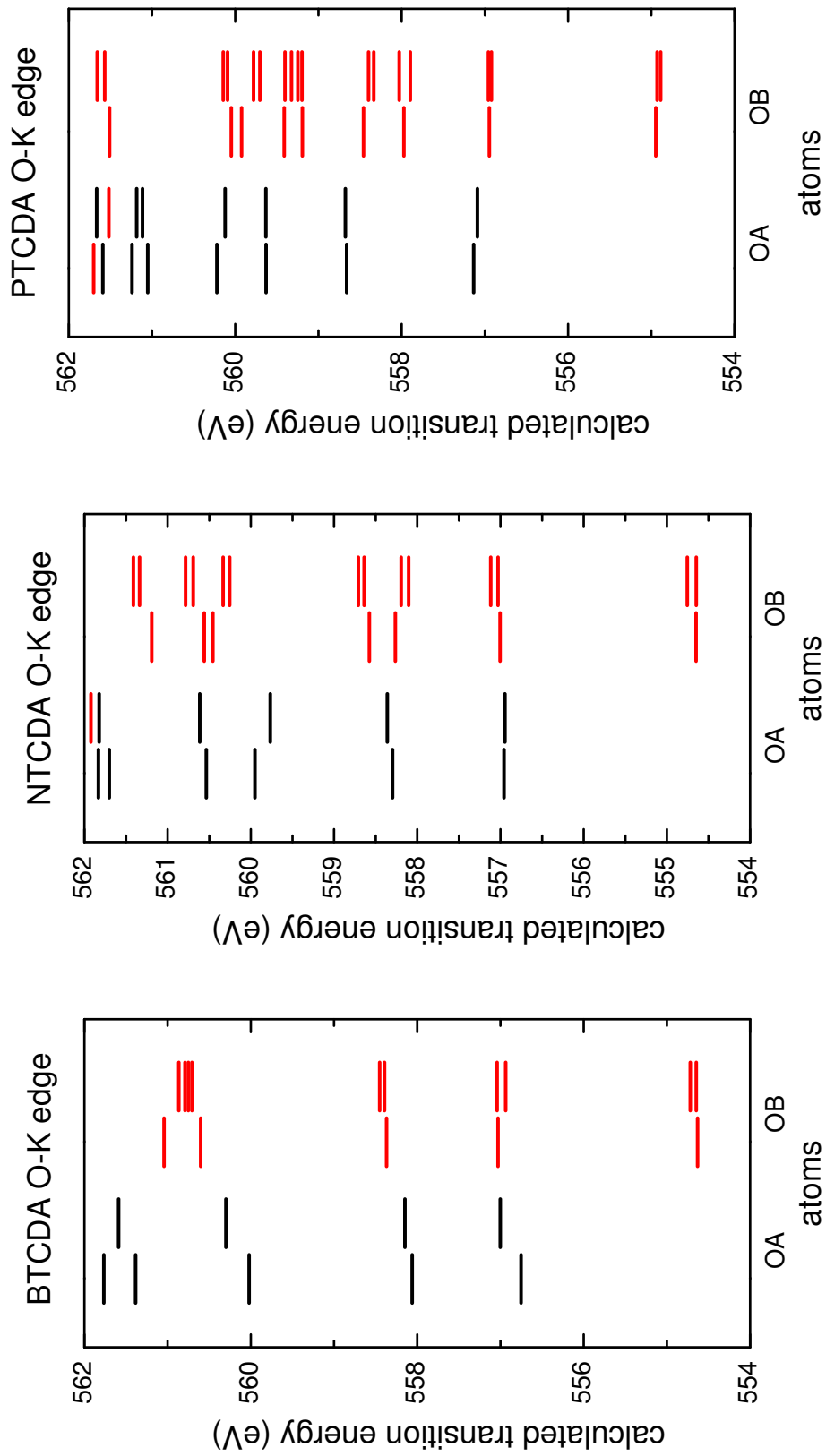
Figure D.3: Z+1 calculations for Dianhydrides in gas and crystal phase. These calculations are based on non–physical C–H bonding distances!
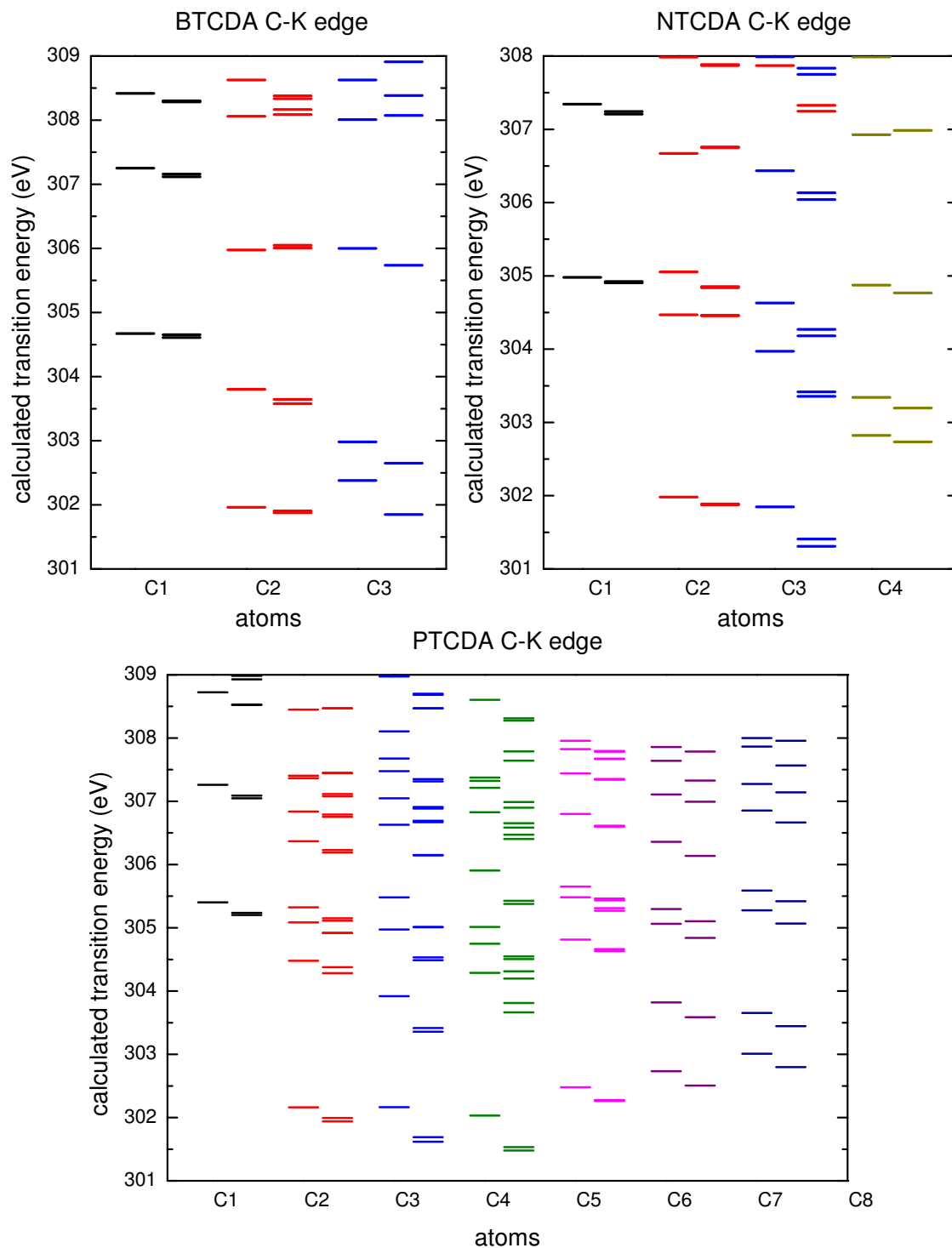
Figure D.4: Z+1 calculations for Dianhydrides in gas and crystal phase. These calculations are based on non–physical C–H bonding distances!

Bibliography

[1] N. Karl. *Charge carrier transport in organic semiconductors.* Synth. Met. **133-134** (2003), 649.

[2] V. Coropceanu, J. Cornil, D. da Silva Filho, Y. Olivier, R. Silbey, and J. Bredas. *Charge Transport in Organic Semiconductors.* Chem. Rev. (Washington, DC, U. S.) **107(4)** (2007), 926.

[3] K. Hannewald and P. Bobbert. *Ab initio theory of charge-carrier conduction in ultrapure organic crystals.* Appl. Phys. Lett. **85** (2004), 1535.

[4] A. Troisi and G. Orlandi. *Charge–Transport Regime of Crystalline Organic Semiconductors: Diffusion Limited by Thermal Off-Diagonal Electronic Disorder.* Phys. Rev. Lett. **96(8)** (2006), 086601.

[5] J. Stöhr. *NEXAFS Spectroscopy.* Springer Series in Surface Science 25. Springer-Verlag Berlin Heidelberg, Berlin Heidelberg, 1992.

[6] D. Turner, C. Baker, A. Baker, and C. Brundle. *Molecular Photoelectron Spectroskopy.* John Wiley & Sons Ltd., London, 1970.

[7] OLED–DISPLAY.NET. 15.09.2009.

[8] M. B. Casu, Y. Zou, S. Kera, D. Batchelor, T. Schmidt, and E. Umbach. *Investigation of polarization effects in organic thin films by surface core-level shifts.* Phys. Rev. B: Condens. Matter Mater. Phys. **76(19)** (2007), 193311.

[9] H. Yamane, S. Kera, K. K. Okudaira, D. Yoshimura, K. Seki, and N. Ueno. *Intermolecular energy-band dispersion in PTCDA multilayers.* Phys. Rev. B: Condens. Matter Mater. Phys. **68(3)** (2003), 033102.

[10] N. Koch, A. Vollmer, I. Salzmann, B. Nickel, H. Weiss, and J. P. Rabe. *Evidence for Temperature-Dependent Electron Band Dispersion in Pentacene.* Phys. Rev. Lett. **96(15)** (2006), 156803.

[11] M. Schneider, E. Umbach, and M. Sokolowski. *Growth-dependent optical properties of 3,4,9,10-perylenetetracarboxylicacid-dianhydride (PTCDA) films on Ag(111).* Chem. Phys. **325(1)** (2006), 185.

[12] M. Leonhardt, O. Mager, and H. Port. *Two-component optical spectra in thin PTCDA films due to the coexistence of α- and β–phase.* Chem. Phys. Lett. **313(1-2)** (1999), 24.

[13] Z. Chen, V. Stepanenko, V. Dehm, P. Prins, L. Siebbeles, J. Seibt, P. Marquetand, V. Engel, and F. Würthner. *Photoluminescence and Conductivity of Self-Assembled $\pi - \pi$ Stacks of Perylene Bisimide Dyes.* Chem.–Eur. J. **13(2)** (2007), 436.

[14] S. G. Urquhart and R. Gillies. *Matrix effects in the carbon 1s near edge x-ray absorption fine structure spectra of condensed alkanes.* J. Chem. Phys. **124(23)** (2006), 234704.

[15] R. Blyth, R. Delaunay, M. Zitnik, J. Krempasky, R. Krempaska, J. Slezak, K. Prince, R. Richter, M. Vondracek, and R. Camilloni. *The high resolution Gas Phase Photoemission Beamline, ELETTRA.* J. Electron Spectrosc. Relat. Phenom. **101-103** (1999), 959.

[16] F. Holch. *NEXAFS – Spektroskopie an organischen Molekülen in der Gasphase.* Diploma Thesis, Universität Würzburg, 2004.

[17] E. Silinsh and V. Čápek. *Organic Molecular Crystals.* American Institute of Physics, New York, 1994.

[18] C. Dimitrakopoulos and P. Malenfant. *Organic Thin Film Transistors for Large Area Electronics.* Adv. Mater. (Weinheim, Ger.) **14(2)** (2002), 99.

[19] A. B. Djurisic, T. Fritz, and K. Leo. *Modeling the optical constants of organic thin films: application to 3,4,9,10-perylenetetracarboxylic dianhydride (PTCDA).* Opt. Commun. **183(1-4)** (2000), 123 .

[20] U. Gómez, M. Leonhardt, H. Port, and H. C. Wolf. *Optical properties of amorphous ultrathin films of perylene derivatives.* Chem. Phys. Lett. **268(1-2)** (1997), 1 .

[21] E. Engel, K. Schmidt, D. Beljonne, J.-L. Brédas, J. Assa, H. Fröb, K. Leo, and M. Hoffmann. *Transient absorption spectroscopy and quantum-chemical studies of matrix-isolated perylene derivatives.* Phys. Rev. B: Condens. Matter Mater. Phys. **73(24)** 245216.

[22] R. Scholz and M. Schreiber. *Linear optical properties of perylene-based chromophores.* Chem. Phys. **325(1)** (2006), 9 . Electronic Processes in Organic Solids.

[23] R. Scholz, A. Kobitski, T. Kampen, M. Schreiber, D. Zahn, G. Jungnickel, M. Elstner, M. Sternberg, and T. Frauenheim. *Resonant Raman spectroscopy of 3,4,9,10-perylene-tetracarboxylic-dianhydride epitaxial films.* Phys. Rev. B: Condens. Matter Mater. Phys. **61(20)** (2000), 13659.

[24] V. Wagner, T. Muck, J. Geurts, M. Schneider, and E. Umbach. *Raman analysis of first monolayers of PTCDA on Ag(111).* Appl. Surf. Sci. **212-213** (2003), 520 . 11th International Conference on Solid Films and Surfaces.

[25] G. R. Fleming and P. G. Wolynes. *Chemical Dynamics in Solution.* Phys. Today **43(5)** (1990), 36.

[26] J. Sauther, J. Wüsten, S. Lach, and C. Ziegler. *Gas phase and bulk ultraviolet photoemission spectroscopy of 3,4,9,10-perylene-tetracarboxylic dianhydride, 1,4,5,8-naphthalene-tetracarboxylic dianhydride, and 1,8-naphthalene-dicarboxylic anhydride.* J. Chem. Phys. **131(3)** 034711.

[27] W. Wurth, J. Stöhr, P. Feulner, X. Pan, K. R. Bauchspiess, Y. Baba, E. Hudel, G. Rocker, and D. Menzel. *Bonding, structure, and magnetism of physisorbed and chemisorbed O_2 on Pt(111).* Phys. Rev. Lett. **65(19)** (1990), 2426.

[28] C. Puglia, A. Nilsson, B. Hernnäs, O. Karis, P. Bennich, and N. Mårtensson. *Physisorbed, chemisorbed and dissociated O_2 on Pt(111) studied by different core level spectroscopy methods.* Surf. Sci. **342(1-3)** (1995), 119 .

[29] L. Kilian. *Adsorption, Struktur und Morphologie hochgeordneter organischer Adsorbatschichten.* PhD Thesis, Universität Würzburg, 2002.

[30] M. Chiodi, L. Gavioli, M. Beccari, V. D. Castro, A. Cossaro, L. Floreano, A. Morgante, A. Kanjilal, C. Mariani, and M. G. Betti. *Interaction strength and molecular orientation of a single layer of pentacene in organic-metal interface and organic-organic heterostructure.* Phys. Rev. B: Condens. Matter Mater. Phys. **77(11)** 115321.

[31] M. Alagia, C. Baldacchini, M. G. Betti, F. Bussolotti, V. Carravetta, U. Ekström, C. Mariani, and S. Stranges. *Core-shell photoabsorption and photoelectron spectra of gas-phase pentacene: Experiment and theory.* J. Chem. Phys. **122(12)** 124305.

[32] S. Krummacher, M. Biermann, M. Neeb, A. Liebsch, and W. Eberhardt. *Close similarity of the electronic structure and electron correlation in gas-phase and solid C_{60}.* Phys. Rev. B: Condens. Matter Mater. Phys. **48(11)** (1993), 8424.

[33] H. Bethe. *Termaufspaltung in Kristallen.* Ann. Phys. **395(2)** (1929), 133.

[34] M. Inokuti and B. Bederson. *Bethe's contributions to atomic and molecular physics.* Phys. Scr. **73(2)** (2006), C98.

[35] H. A. Jahn and E. Teller. *Stability of Polyatomic Molecules in Degenerate Electronic States. I. Orbital Degeneracy.* Proc. R. Soc. A **161** (1937), 220.

[36] O. Fuchs. *Soft x–ray spectroscopy of organic molecules and liquids.* PhD Thesis, Universität Würzburg, 2009.

[37] M. Born and R. Oppenheimer. *Zur Quantentheorie der Molekeln.* Ann. Phys. **389(20)** (1927), 457.

[38] R. F. Fink, S. L. Sorensen, A. N. de Brito, A. Ausmees, and S. Svensson. *The resonant Auger electron spectrum of C $1s^{-1}$ π^* excited ethene: A combined theoretical and experimental investigation.* J. Chem. Phys. **112(15)** (2000), 6666.

[39] R. Brun and F. Rademakers. *ROOT – An Object Oriented Data Analysis Framework.* Nucl. Instrum. Methods Phys. Res., Sect. A **389** (1997), 81. Proceedings AIHENP'96 Workshop, Lausanne, Sep. 1996.

[40] L. S. Cederbaum and W. Domcke. *On the vibrational structure in photoelectron spectra by the method of Green's functions.* J. Chem. Phys. **60(7)** (1974), 2878.

[41] A. Thompson. *X-RAY DATA BOOKLET.* Lawrence Berkeley National Laberatory, Berkeley, second edition, 2001.

[42] B. Wästberg, S. Lunell, C. Enkvist, P. A. Brühwiler, A. J. Maxwell, and N. Mårtensson. *1s x-ray-absorption spectroscopy of C_{60}: The effects of screening and core-hole relaxation.* Phys. Rev. B: Condens. Matter Mater. Phys. **50(17)** (1994), 13031.

[43] M. J. Frisch, G. W. Trucks, H. B. Schlegel, G. E. Scuseria, M. A. Robb, J. R. Cheeseman, J. A. Montgomery, Jr., T. Vreven, K. N. Kudin, J. C. Burant, et al. *Gaussian 03, Revision C.02* Gaussian, Inc., Wallingford, CT, 2004.

[44] N. Kosugi and H. Kuroda. *Efficient methods for solving the openshell SCF problem and for obtaining an initial guess. The "One-Hamiltonian" and the "Partial SCF" methods.* Chem. Phys. Lett. **74** (1980), 490.

[45] N. Kosugi and H. Kuroda. *Equivalent-core basis functions to study core-ionized and excited states.* Chem. Phys. Lett. **94(4)** (1983), 377 .

[46] N. Kosugi. *Strategies to vectorize conventional SCF-CI algorithms.* Theor. Chim. Act. **72** (1987), 149.

[47] M. Cohen and P. S. Kelly. *Hartree-–Fock wave functions for excited states: III. Dipole transitions in three-electron systems.* Can. J. Phys. **45** (1967), 1661.

[48] R. Fink. *Theoretical autoionization spectra of 1s –> π^* excited N_2 and N_2O.* J. Electron Spectrosc. Relat. Phenom. **76** (1995), 295 . Proceedings of the Sixth International Conference on Electron Spectroscopy.

[49] W. Liu and R. F. Fink. (in preparation) .

[50] P. Atkins and R. Friedman. *Molecular Quantum Mechanics.* Oxford University Press, fourth edition, 2005.

[51] J. L. Brédas, J. P. Calbert, D. A. da Silva Filho, and J. Cornil. *Organic semiconductors: A theoretical characterization of the basic parameters governing charge transport.* Proc. Natl. Acad. Sci. U. S. A. **99** (2002), 5804.

[52] D. Faltermeier, B. Gompf, M. Dressel, A. K. Tripathi, and J. Pflaum. *Optical properties of pentacene thin films and single crystals.* Phys. Rev. B: Condens. Matter Mater. Phys. **74(12)** 125416.

[53] M. I. Alonso, M. Garriga, N. Karl, J. O. Ossó, and F. Schreiber. *Anisotropic optical properties of single crystalline PTCDA studied by spectroscopic ellipsometry.* Org. Electron. **3(1)** (2002), 23 .

[54] M. Kasha, H. R. Rawls, and M. Asharf el-Bayoumi. *The exciton model in molecular Spectroscopy.* Pure Appl. Chem. **11** (1965), 371.

[55] A. S. Davydov. *Theory of Molecular Excitons.* Plenum Press New York–London, 1971.

[56] Thermocoax GmbH. *Heating elements.* Stapelfeld, Germany.

[57] Lebow Company. *Thin foil.* Goleta, NJ, USA.

[58] B. Henke, E. Gullikson, and J. Davis. *X-Ray Interactions: Photoabsorption, Transmission, and Reflection at $E = 50 - 30000eV$, $Z = 1 - 92$.* Atomic Data And Nuclear Data Tables **54(2)** (1993), 181.

[59] A. Schöll, Y. Zou, T. Schmidt, R. Fink, and E. Umbach. *Energy calibration and intensity normalization in high–resolution NEXAFS spectroscopy.* J. Electron Spectrosc. Relat. Phenom. **129(1)** (2003), 1.

[60] J. F. O'Hanlon. *A User's guide to Vacuum Technology.* Wiley-Interscience, second edition, 1989.

[61] E. Pohlmann, R. Huttl, and H. Knecht. *Self-maintained reed chopper for beam modulation in UHV.* J. Phys. E: Sci. Instrum. **20(4)** (1987), 455.

[62] Electro–Optical Products Corporation. *Optical Choppers.* Fresh Meadows, NY, USA.

[63] R. Flesch, A. A. Pavlychev, J. J. Neville, J. Blumberg, M. Kuhlmann, W. Tappe, F. Senf, O. Schwarzkopf, A. P. Hitchcock, and E. Rühl. *Dynamic Stabilization in $1\sigma_u \to 1\pi_g$ Excited Nitrogen Clusters.* Phys. Rev. Lett. **86(17)** (2001), 3767.

[64] J. Bruley, M.-W. Tseng, and D. B. Williams. *Spectrum-Line Profile Analysis of a Magnesium Aluminate Spinel Sapphire Interface.* Phys. Rev. B: Condens. Matter Mater. Phys. **6** (1995), 1.

[65] A. P. Hitchcock and C. E. Brion. *K-shell excitation spectra of CO,* N_2 *and* O_2. J. Electron Spectrosc. Relat. Phenom. **18(1)** (1980), 1.

[66] T. Sham, B. Yang, J. Kirz, and J. Tse. *K-edge near-edge x-ray-absorption fine structure of oxygen- and carbon-containing molecules in the gas phase.* Phys. Stat. Sol. A **40(2)** (1989), 652.

[67] M. Tronc, G. C. King, and F. H. Read. *Carbon K-shell excitation in small molecules by high-resolution electron impact.* J. Phys. B: At., Mol. Opt. Phys. **12(1)** (1979), 137.

[68] A. P. Hitchcock, D. C. Newbury, I. Ishii, J. Stöhr, J. A. Horsley, R. D. Redwing, A. L. Johnson, and F. Sette. *Carbon K-shell excitation of gaseous and condensed cyclic hydrocarbons:* C_3H_6, C_4H_8, C_5H_8, C_5H_{10}, C_6H_{10}, C_6H_{12}, *and* C_8H_8. J. Chem. Phys. **85(9)** (1986), 4849.

[69] I. Fujii, N. HIRAYAMA, J. OHTANI, and K. KODAMA. *Crystal Structure of Tris(8-quinolinolato)aluminum(III)- Ethyl Acetate(1/0.5).* Phys. Rev. B: Condens. Matter Mater. Phys. **12** (1996), 153.

[70] C. W. Tang and S. A. VanSlyke. *Organic electroluminescent diodes.* Phys. Rev. B: Condens. Matter Mater. Phys. **51(12)** (1987), 913.

[71] M. M. Levichkova, J. J. Assa, H. Fröb, and K. Leo. *Blue luminescent isolated Alq₃ molecules in a solid-state matrix.* Appl. Phys. Lett. **88(20)** 201912.

[72] J. D. Anderson, E. M. McDonald, P. A. Lee, M. L. Anderson, E. L. Ritchie, H. K. Hall, T. Hopkins, E. A. Mash, J. Wang, A. Padias, et al. *Electrochemistry and Electrogenerated Chemiluminescence Processes of the Components of Aluminum Quinolate/Triarylamine, and Related Organic Light-Emitting Diodes.* J. Am. Chem. Soc. **120(37)** (1998), 9646.

[73] S. Krause. *Determination of the transport levels in thin films of organic semiconductors.* PhD thesis, Universität Würzburg, 2009.

[74] S. Krause, M. B. Casu, A. Scholl, and E. Umbach. *Determination of transport levels of organic semiconductors by UPS and IPS.* New J. Phys. **10(8)** (2008), 085001 (16pp).

[75] M. Brinkmann, G. Gadret, M. Muccini, C. Taliani, N. Masciocchi, and A. Sironi. *Correlation between Molecular Packing and Optical Properties in Different Crystalline Polymorphs and Amorphous Thin Films of mer-Tris(8-hydroxyquinoline)aluminum(III).* J. Am. Chem. Soc. **122(21)** (2000), 5147.

[76] A. Curioni, W. Andreoni, R. Treusch, F. J. Himpsel, E. Haskal, P. Seidler, C. Heske, S. Kakar, T. van Buuren, and L. J. Terminello. *Atom-resolved electronic spectra for Alq_3 from theory and experiment.* Appl. Phys. Lett. **72(13)** (1998), 1575.

[77] T. Yokoyama, H. Ishii, N. Matsuie, K. Kanai, E. Ito, A. Fujimori, T. Araki, Y. Ouchi, and K. Seki. *Neat Alq3 thin film and metal/Alq3 interfaces studied by NEXAFS spectroscopy.* Synth. Met. **152(1-3)** (2005), 277 . Proceedings of the International Conference on Science and Technology of Synthetic Metals.

[78] V. V. N. R. Kishore, A. Aziz, K. L. Narasimhan, N. Periasamy, P. S. Meenakshi, and S. Wategaonkar. *On the assignment of the absorption bands in the optical spectrum of Alq3.* Synth. Met. **126(2-3)** (2002), 199 .

[79] N. Dori, M. Menon, L. Kilian, M. Sokolowski, L. Kronik, and E. Umbach. *Valence electronic structure of gas-phase 3,4,9,10-perylene tetracarboxylic acid dianhydride: Experiment and theory.* Phys. Rev. B: Condens. Matter Mater. Phys. **73(19)** 195208.

[80] S. Aravamudhan, U. Haeberlen, H. Irngartinger, and C. Krieger. *Pyromellitic acid dianhydride: crystal structure and anisotropic proton magnetic shielding.* Mol. Phys. **38** (1979), 241.

[81] F. H. Herbstein, R. E. Marsh, and S. Samson. *X-ray diffraction study of the crystal structure of the molecular compound pyrene pyromellitic dianhydride at 19 K.* Acta Crystallogr., Sect. B: Struct. Sci. **50** (1994), 174.

[82] J. C. A. Boeyens. *A free–electron study of π–molecular compounds.* J Phys. Chem. **71(9)** (1967), 2969.

[83] A. Bondi. *van der Waals Volumes and Radii.* J Phys. Chem. **68(3)** (1964), 441.

[84] J. Schirmer, A. B. Trofimov, K. J. Randall, J. Feldhaus, A. M. Bradshaw, Y. Ma, C. T. Chen, and F. Sette. *K-shell excitation of the water, ammonia, and methane molecules using high-resolution photoabsorption spectroscopy.* Phys. Rev. B: Condens. Matter Mater. Phys. **47(2)** (1993), 1136.

[85] O. Rahkonen and M. Krause. *Total And Partial Atomic–Level Widths.* Atomic Data And Nuclear Data Tables **14** (1974), 139.

[86] M. Krause. *Atomic Radiative and Radiationless Yields for K and L Shells.* J. Phys. Chem. Ref. Data **8(2)** (1979), 307.

[87] Y. Hase, K. Kawai, and O. Sala. *The infrared and Raman spectra of pyromellitic dianhydride.* J. Mol. Struct. **26(2)** (1975), 297.

[88] B. Frederick, M. Ashton, N. Richardson, and T. Jones. *Orientation and bonding of benzoic acid, phthalic anhydride and pyromellitic dianhydride on Cu(110).* Surf. Sci. **292(1-2)** (1993), 33 .

[89] A. C. Blackburn, L. J.Fitzgerald, and R. E.Gerkin. *1,4,5,8-Naphthalenetetracarboxylic Acid Cyclic 1,8-Anhydride Bis(dimethyl sulfoxide) Solvate and 1,4,5,8-Naphthalenetetracarboxylic 1,8:4,5-Dianhydride.* Acta Crystallogr., Sect. C: Cryst. Struct. Commun. **53(12)** (1997), 1991.

[90] C. F. Macrae, I. J. Bruno, J. A. Chisholm, P. R. Edgington, P. McCabe, E. Pidcock, L. Rodriguez-Monge, R. Taylor, J. van de Streek, and P. A. Wood. *Mercury CSD 2.0 – new features for the visualization and investigation of crystal structures.* J. Appl. Crystallogr. **41(2)** (2008), 466.

[91] L. Born and G. Heywang. *Crystal structure of 1,4,5,8-naphthalene-tetracarboxylic-dianhydride (NTDA).* Z. Kristallogr. **190** (1990), 147.

[92] A. Schöll, Y. Zou, L. Kilian, D. Hübner, D. Gador, C. Jung, S. Urquhart, T. Schmidt, R. Fink, and E. Umbach. *Electron-Vibron Coupling in High-Resolution X–Ray Absorption Spectra of Organic Materials: NTCDA on Ag(111).* Phys. Rev. Lett. **93(14)** (2004), 146406.

[93] A. Schöll, Y. Zou, D. Hübner, S. G. Urquhart, T. Schmidt, R. Fink, and E. Umbach. *A comparison of fine structures in high–resolution x–ray–absorption spectra of various condensed organic molecules.* J. Chem. Phys. **123(4)** 044509.

[94] D. Hübner and V. Shklover. (in preparation) .

[95] K. Prince, M. Vondracek, J. Karvonen, M. Coreno, R. Camilloni, L. Avaldi, and M. de Simone. *A critical comparison of selected 1s and 2p core hole widths.* J. Electron Spectrosc. Relat. Phenom. **101-103** (1999), 141.

[96] K. Prince, R. Richter, M. de Simone, M. Alagia, and M. Coreno. *Near Edge X-ray Absorption Spectra of Some Small Polyatomic Molecules*. J. Phys. Chem. A **107** (2003), 1955.

[97] R. Püttner, C. Kolczewski, M. Martins, A. S. Schlachter, G. Snell, M. Sant'Anna, J. Viefhaus, K. Hermann, and G. Kaindl. *The C 1s NEXAFS spectrum of benzene below threshold: Rydberg or valence character of the unoccupied σ–type orbitals*. Chem. Phys. Lett. **393(4-6)** (2004), 361 .

[98] A. Hempelmann, M. N. Piancastelli, F. Heiser, O. Gessner, A. Rüdel, and U. Becker. *Resonant photofragmentation of methanol at the carbon and oxygen K-edge by high-resolution ion-yield spectroscopy*. J. Phys. B: At., Mol. Opt. Phys. **32** (1999), 2677.

[99] N. Kosugi. *Molecular symmetries and vibrations in high-resolution inner-shell spectroscopy*. J. Electron Spectrosc. Relat. Phenom. **79** (1996), 351 . Proceedings of the 11th International Conference on Vacuum Ultraviolet Radiation Physics.

[100] K. C. Prince, L. Avaldi, M. Coreno, R. Camilloni, and M. de Simone. *Vibrational structure of core to Rydberg state excitations of carbon dioxide and dinitrogen oxide*. J. Phys. B: At., Mol. Opt. Phys. **32** (1999), 2551.

[101] O. Björneholm, A. Nilsson, E. O. F. Zdansky, A. Sandell, B. Hernnäs, H. Tillborg, J. N. Andersen, and N. Mårtensson. *2π-resonance broadening in x-ray-absorption spectroscopy of adsorbed CO*. Phys. Rev. B: Condens. Matter Mater. Phys. **46(16)** (1992), 10353.

[102] D. R. Zahn, G. N. Gavrila, and M. Gorgoi. *The transport gap of organic semiconductors studied using the combination of direct and inverse photoemission*. Chem. Phys. **325(1)** (2006), 99 . Electronic Processes in Organic Solids.

[103] K. Glöckler, C. Seidel, A. Soukopp, M. Sokolowski, E. Umbach, M. Böhringer, R. Berndt, and W. D. Schneider. *Highly ordered structures and submolecular scanning tunnelling microscopy contrast of PTCDA and DM-PBDCI monolayers on Ag(111) and Ag(110)*. Surf. Sci. **405(1)** (1998), 1 .

[104] Y. Zou, L. Kilian, A. Schöll, T. Schmidt, R. Fink, and E. Umbach. *Chemical bonding of PTCDA on Ag surfaces and the formation of interface states*. Surf. Sci. **600(6)** (2006), 1240 .

[105] A. Hauschild, K. Karki, B. C. C. Cowie, M. Rohlfing, F. S. Tautz, and M. Sokolowski. *Molecular Distortions and Chemical Bonding of a Large π-Conjugated Molecule on a Metal Surface*. Phys. Rev. Lett. **94(3)** (2005), 036106.

[106] F. Tautz. *Structure and bonding of large aromatic molecules on noble metal surfaces: The example of PTCDA*. Prog. Surf. Sci. **82(9-12)** (2007), 479 .

[107] K. Tojo and J. Mizuguchi. *Refinement of the crystal structure of β-3,4:9,10-perylenetetracarboxylic dianhydride, $C_{24}H_8O_6$, at 223 K*. Z. Kristallogr. **217** (2002), 255.

[108] T. Ogawa, K. Kuwamoto, S. Isoda, T. Kobayashi, and N. Karl. *3,4:9,10-Perylenetetracarboxylic dianhydride (PTCDA) by electron crystallography*. Acta Crystallogr., Sect. B: Struct. Sci. **55(1)** (1999), 123.

[109] K. Tojo and J. Mizuguchi. *Refinement of the crystal structure of α-3,4:9,10-perylenetetracarboxylic dianhydride, C24H8O6, at 223 K*. Z. Kristallogr. **217** (2002), 253.

[110] E. Umbach, M. Sokolowski, and R. Fink. *Substrate-interaction, long-range order, and epitaxy of large organic adsorbates*. Applied Physics A **63** (1996), 565.

[111] F. S. Tautz, S. Sloboshanin, J. A. Schaefer, R. Scholz, V. Shklover, M. Sokolowski, and E. Umbach. *Vibrational properties of ultrathin PTCDA films on Ag(110)*. Phys. Rev. B: Condens. Matter Mater. Phys. **61** (2000), 16933.

[112] A. Y. Kobitski, R. Scholz, and D. R. T. Zahn. *Theoretical studies of the vibrational properties of the 3,4,9,10,-perylene tetracarboxylic dianhydride (PTCDA) molecule*. J. Mol. Struct. **625(1-3)** (2003), 39 .

[113] M. Häming. personal communication, 2009.

[114] P. Coppens. *The use of a polarized hydrogen atom in X-ray structure refinement*. Acta Crystallogr., Sect. B: Struct. Sci. **28(5)** (1972), 1638.

[115] M. I. Kay, Y. Okaya, and D. E. Cox. *A refinement of the structure of the room-temperature phase of phenanthrene, $C_{14}H_{10}$, from X-ray and neutron diffraction data*. Acta Crystallogr., Sect. B: Struct. Sci. **27** (1971), 26.

[116] F. H. Allen, O. Kennard, D. G. Watson, L. Brammer, A. G. Orpen, and R. Taylor. *Tables of bond lengths determined by X-ray and neutron diffraction. Part 1. Bond lengths in organic compounds*. J. Chem. Soc. Perk. 2 **2** (1987), 1.

[117] R. Fink, D. Hübner, A. Schöll, E. Umbach, K. Prince, R. Richter, M. Coreno, and M. Alagia. *Electron–Vibron Coupling in Large Organic Molecules*. Research Highlights ELETTRA 51.

[118] S. Singh, M. Jayswal, and R. Singh. *Vibrational Spectrum Of Acenaph-thenequinone.* Phys. Rev. B: Condens. Matter Mater. Phys. **36** (1967), 624.

[119] D. Verma, R. Dash, K. S. Katti, D. L. Schulz, and A. N. Caruso. *Role of coordinated metal ions on the orientation of phthalocyanine based coatings.* Spectrochim. Acta, Part A **70(5)** (2008), 1180 .

[120] E. Fuente, J. A. Menendez, M. A. Diez, D. Suarez, and M. A. Montes-Moran. *Infrared Spectroscopy of Carbon Materials: A Quantum Chemical Study of Model Compounds.* J. Phys. Chem. B **107(26)** (2003), 6350.

[121] S. Kera. personal communication, 2005.

[122] G. Nemethy, M. S. Pottle, and H. A. Scheraga. *Energy parameters in polypeptides. 9. Updating of geometrical parameters, nonbonded interactions, and hydrogen bond interactions for the naturally occurring amino acids.* J. Chem. Phys. **87(11)** (1983), 1883.

[123] Advanced Chemistry Development, Inc. *ACD/ChemSketch Freeware, version 10.00.* Toronto, ON, Canada, 2006.

[124] OriginLab Corporation. *Origin 6.0.* Northampton, MA, USA, 1999.

[125] M. Kohm and J. U. Morawski. *KOMA–Script.* Lehmanns Media, Berlin, third edition, 2008.

List of Figures

List of Tables

Danksagung

Zum Schluss möchte ich all denen, die zum Gelingen dieser Arbeit beigetragen haben ganz herzlich danken:

- Meinen langjährigen Mitstreitern der ersten Stunde FloMaier, Stefann und Christian für die unzähligen Diskussionen über Dies und manchmal auch Das, die Kaffeepausen usw.

- Meinen Leidensgenossinnen beim Fertig–Zusammen–Schreiben Franziska und Moni für die *stets kurzen* Kaffeepausen um 04:00Uhr morgens

- Meinem Büro Kollegen Marc Häming für die vielen physikalischen und nicht–physikalischen (*Buuuttterbemmmmeeee...*) Diskussionen

- Der gesamten restlichen EPII (bzw. jetzt EPVII), vor allem jenen, die das angenehm freundliche und hilfsbereite Arbeitsklima wesentlich geprägt haben; Schaut zu, dass ihr euch das erhaltet!

- Allen Beteiligten am Projekt *Mikrothermal Extraktor für granulare organische Materie zur Erzeugung hochthermaler fluider Dispersionen aromatischer Verbindungen.* (Wir sollten doch noch ein Projekt beantragen...)

- Den ganzen Guten Geistern der Universität, die jeden Tag dafür sorgen, dass es was zu Essen gibt, Rechner und Netzwerke gut funktionieren, der Campus hübsch ausschaut...

- Der LaTeX und sonstigen Open Source Community für die vielen tollen Pakete und Programme die das PhD Leben so viel leichter machen

- Allen anderen die ich an dieser Stelle ungerechter Weise vergessen habe

Mein ganz besonderer Dank gilt natürlich meiner Familie. Meiner Frau Caroline danke ich für ihr Verständnis für meine Zusammenschreib–Nachtschichten und die Versorgung mit Motivations–Kuchen, Waffeln... und dafür, dass Sie die Zeit als *PhD–Widow* auf sich genommen hat. Meinem Bruder Felix danke ich für den tollen Bildschirm ohne den ich wohl beim Augenarzt und Orthopäden gelandet wäre. Ganz besonders bedanke ich mich bei meinen Eltern und Großeltern, deren voller Unterstützung ich mir stets sicher sein konnte und kann, ganz gleich was auch immer ich vor habe.